Near-Infrared Emitting Quantum Dots for Cellular and Vascular Fluorescent Labeling in *In Vivo* Multiplexed Imaging Studies

by

Juwell Wendy Wu

S.B. Materials Science & Engineering
S.B. Mathematics
Massachusetts Institute of Technology, 2001

Submitted to the Harvard-MIT Division of Health Sciences and Technology in Partial Fulfillment of the Requirements for the Degree of

DOCTOR OF PHILOSOPHY

at the

MASSACHUSETTS INSTITUTE OF TECHNOLOGY

SEPTEMBER 2011

Signature of Author: _____
Harvard-MIT Division of Health Sciences and Technology
August 23rd, 2011

Certified by: _____
Charles P. Lin, Ph.D.
Associate Professor, Harvard Medical School
Wellman Center for Photomedicine and Center for Systems Biology, MGH
Thesis Co-Supervisor

Certified by: _____
Moungi G. Bawendi, Ph.D.
Lester Wolfe Professor in Chemistry, MIT
Thesis Co-Supervisor

Accepted by: _____
Ram Sasisekharan, Ph.D.
Director, Harvard-MIT Division of Health Sciences and Technology
Edward Hood Taplin Professor of Health Sciences & Technology and Biological Engineering

Near-Infrared Emitting Quantum Dots for Cellular and Vascular Fluorescent Labeling in *In Vivo* Multiplexed Imaging Studies

by

Juwell Wendy Wu

Submitted to The Harvard-MIT Division of Health Sciences and Technology on August 23rd, 2011 in Partial Fulfillment of the Requirements for the Degree of Doctor of Philosophy

ABSTRACT

In vivo multimodal, multiplexed microscopy allows real-time observation of hematopoietic cells, their stem and progenitor cells and metastatic cancer cells in their native bone marrow (BM) environment. Multiplexing has made possible detailed studies of the BM's microarchitecture, which helps define the niche of these cells; it has nonetheless been limited by the paucity of suitable probes fluorescent in the near-infrared spectrum that is favored by tissue optics. This project attempts to address this problem by developing cellular and vascular fluorescent imaging probes comprised of semiconductor nanocrystals, or quantum dots (QDs), with tunable fluorescence between 650-800nm and exhibiting photostability, robust quantum yield and narrow fluorescence profiles that are critical for such applications.

The synthesis of alloyed $CdTe_xSe_{1-x}$ QDs will be detailed in the thesis. Reproducibility and workability in subsequent steps are emphasized in the methods. Special attention is also paid to the difference between working with alloyed versus single semiconductor QDs, especially the need to achieve physical and spectral uniformity when composition and its gradient are also variable.

The steps for creating biological probes from these QD fluorophores are also described. They include overcoating, water solubilization and functionalization for cellular uptake and vascular retention. Finally, the thesis returns to its motivation and reports novel methods, developed using NIR QD vascular imaging probes, for visualizing *in vivo* 3-D imaging data of the murine BM and characterizing the tissue's architecture. Measuring the Euclidean distance between BM osteoblasts and blood vessels is presented to exemplify a potential platform for describing the geographic relationships between cells, molecules and structural components in any tissue.

Thesis Co-supervisor: Moungi G. Bawendi, Ph.D.
Title: Lester Wolfe Professor in Chemistry, MIT

Thesis Co-supervisor: Charles P. Lin, Ph.D.
Title: Associate Professor, Harvard Medical School

ACKNOWLEDGMENT

First of all, I'd like to express my heart-felt gratitude to Charles and Moungi, my co-advisors, for their invaluable time and patience, for letting me join in the fun and excitement that is their research, for sharing their knowledge and wisdom in science and beyond.

I'd like to thank Dr. Tayyaba Hasan for being in my thesis committee, for her advices.

I can't be here—literally in some cases—without my family and friends. The latter, of course, include every member of both the Lin Lab and the Bawendi Lab. Thank you for all the help, the discussions big and small, the laughs, the late night cookies.

Thank you.

Table of Contents

List of Figures

1 Near Infrared Fluorescent Probes for In vivo Imaging

1.1 Motivation: *In vivo* Multiplexed Imaging as a Tool for Understanding Biological Processes— Studies of the Murine Calvarial Bone Marrow

Biological processes are the sum of intricate interactions between extra- and intra-cellular components. These interactions can be local or remote and they proceed in a wide range of timescales. Remarkable advances in imaging technologies have greatly expanded our medical knowledge. *In vivo* imaging, in particular, has offered the opportunity to observe biological events in real time and in their native environment, circumventing the shortcomings of using *in vitro* models that often fall short of fully capturing the structural and biochemical complexity of live tissues. It also precludes interpretations of *ex vivo* data that is often marred by artifacts resulting from post-mortem biopsies and histological preparations. As a technique that can track an event over time, *in vivo* imaging offers a more telling picture on the function of each relevant entity than "snapshots" from immunochemistry are able to.

In vivo imaging has evolved into a technically advanced field that includes a wide range of modalities, some of which—such as X-ray computer tomography (CT), magnetic resonance imaging (MRI) and positron emission tomography (PET)—have become standard tools for clinical diagnosis. Meanwhile, fluorescence microscopy has found ubiquitous applications in laboratory research. In particular, by extracting information from animal models with well-characterized genetic makeup designed to mimic human physiology and pathology, *in vivo* fluorescence microscopy has closed significant gaps between knowledge gained from *in vitro* and clinical studies. In particular, the use of small animals (such as rodents) for imaging, combined with the highly-resolved optical sectioning power of confocal and multi-photon microscopy [188,202], allows for time series and 3-D reconstructions of biological events that

cumulate to a comprehensive view of these events that are impossible to collect from human subjects.

Multiplexing is indispensible to the utility of *in vivo* fluorescence imaging. A series of optical channels simultaneously visualize multiple biological components, each labeled with imaging probes of a specific range of fluorescence wavelengths. By permitting observation of not only the individual components but also co-localization of their representative fluorescent signals, which suggests of interactions, the data from *in vivo* multiplexed imaging has helped to identify the roles played by each component and from that, the mechanisms that drive and maintain the biological processes they take part in, whether they are physiological or pathological. With this knowledge, novel strategies in clinical management can be devised.

The bone marrow (BM) is a biologically active and functionally complex tissue, the residence of hematopoietic cells and a common metastatic site for solid and liquid tumors. Biology of the BM is clinically relevant to immunology, cancer biology and transplantation medicine, and while it is beyond the scope of this thesis to examine it in detail, *in vivo* multiplexed imaging of the BM has offered the context and motivation of this project—namely, to further expand the multiplexing capability of the *in vivo* imaging systems developed in Lin Lab [61,107,108164,171] (Figure 1.1) by adding near-infrared (NIR) fluorescent imaging probes to our current set in use, which mostly emits in the visible spectrum.

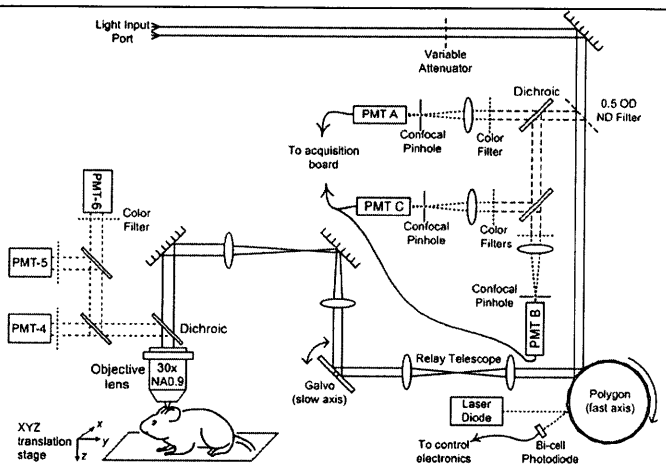

Figure 1.1: *In vivo* multimodal, multiplexed imaging system developed in the Lin Lab. The light input includes a titanium:sapphire laser (700-1100nm excitation) for two-photon microscopy and second harmonic generation, and three diode lasers (492, 532, 633nm) for confocal imaging. Three detection channels can be acquired at video rate (30 frames/second) simultaneously (out of the six available; 3 for confocal (A-C) and 3 for two-photon (4-6)). The anesthetized animal subject is placed on a 37°C, motorized precision stage for imaging.

Cell trafficking in the BM—whether the cells are leukocytes, malignant cells, or hematopoietic stem & progenitor cells (HSPCs)—is highly dynamic, from the cells' physical behavior (ex. the "rolling and sticking" of leukocytes on the endothelium [99]), to the local microenvironment's expressions of molecules to guide the cells' migration in and out of the BM, to the fate of the cells and its corresponding clinical outcome (ex. organ-specific metastasis). The BM is a traditionally difficult tissue to study *ex vivo*, as its interface with the hard bone, which not only acts as structural support but also modulates its function, is prone to damage and creation of artifacts during tissue sectioning. The relative translucence of murine calvarium (i.e. mouse skullcap) has provided unique opportunities for *in vivo* observation of the BM with its surrounding cortical bone left intact [116], thus minimizing perturbation of the local environment before and during imaging. Description of the murine calvarial BM and representative *in vivo* images collected from the area are illustrated in Figure 1.2. Structurally, the calvarial BM is located in multiple cavities inside the bone, most of which lie sagittally to the midline of the skull (Figure 1.2 a). The bone surface lining each cavity, the endosteum, is covered with bone cells (osteoblasts and osteoclasts)

that constantly remodel the hard tissue and secrete cytokines and other soluble factors that modulate the behavior of hematopoietic cells; arteries burrow through hard bone of the skull into the BM and arborize into an intricate network of capillaries and sinusoids that supply nutrients to the soft tissue in each cavity and drain into a central sinus that runs parallel to the skull's midline (Figure 1.2 b, c). Hematopoietic cells pack the soft tissue of the BM (Figure 1.2 d), which is also the engraftment site of secondary lesions when bone metastasis occurs [130,164,171].

The BM plays a critical role in regulating the balance between quiescence, renewal and differentiation of HSPCs for maintenance and repair [169]. The complex microarchitecture of the BM, in spatially defining the locations of its residing cell types (endothelial cells, osteoblasts etc.), partially describes the HSPC niche [166]. As HSPC proliferation reconstitutes the blood and immune cells in patients who have undergone BM irradiation and transplantation, identifying the niche for HSPCs is of clinical significance; it also helps to pinpoint the multipotent subpopulation within the HSPCs that is truly capable of regenerating hematopoietic cells of all lineages. *In vivo* multiplexed imaging in two-photon or confocal mode has not only visualized single HSPC activity (Figure 1.2 e), but also permitted quantitative morphometry of the local microenvironment—measurement of the density and location of nearby cells such as osteoblasts and endothelial cells, for example, and expressions of biologically relevant molecules such as signaling proteins and chemokines that altogether form the residence of and offer functional cues to the HSPCs (Figure 1.2 f).

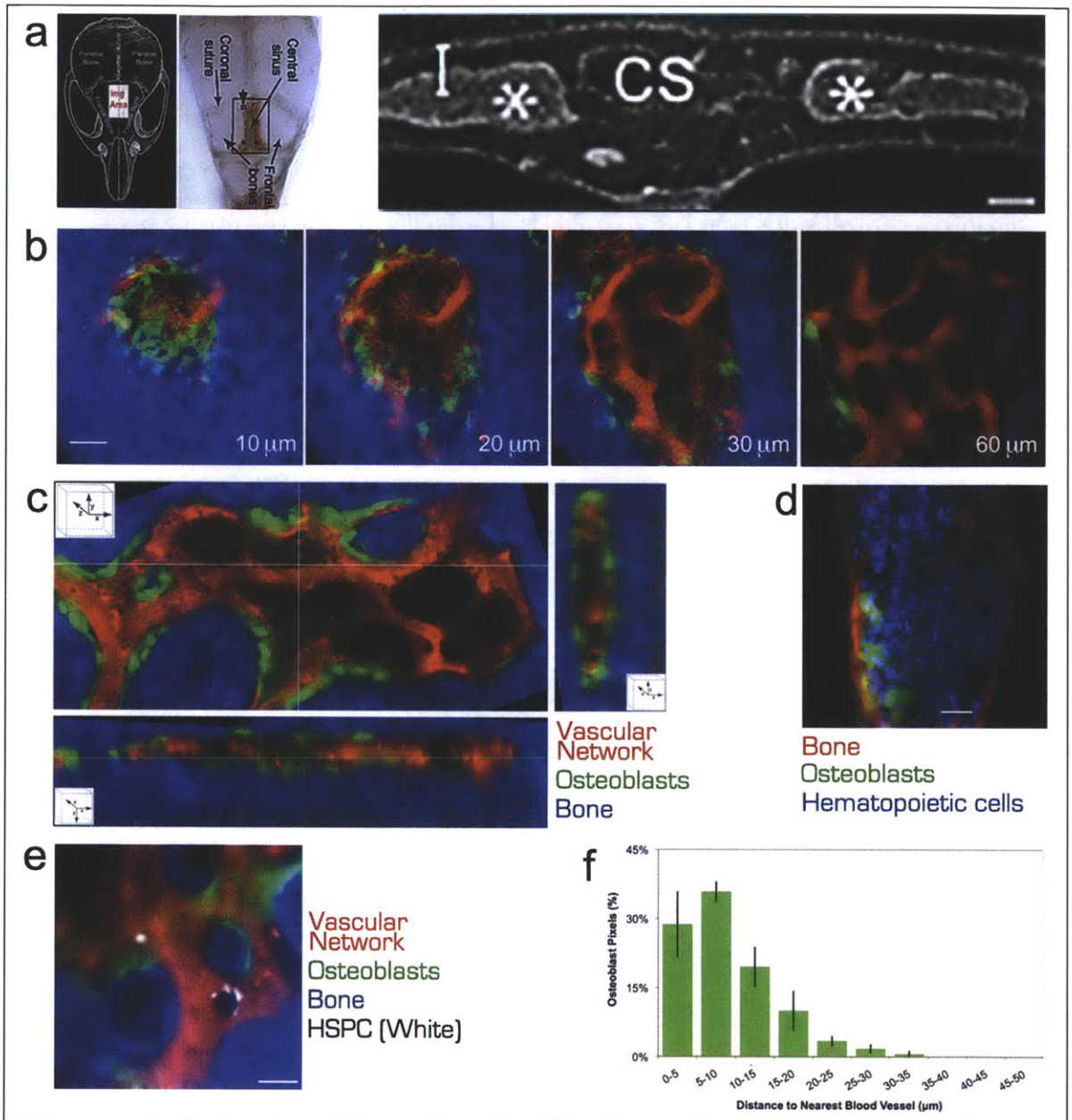

Figure 1.2: *In vivo* imaging of the murine calvarial BM [107,108]. a) The murine calvarial BM. Left: the boxed area in each image represents the region of interest; in the white light image, the bone marrow, with its reddish tint, can be seen distributed along the central sinus (CS). This "aerial" perspective corresponds to the X-Y imaging plane; the Z-axis quantifies the imaging depth from the skull surface. Right: an X-Z tissue slice that shows the cross section of two bone marrow cavities (labeled with asterisks) flanking the central sinus and embedded inside hard bone; the bracket indicates the imaging depth the *in vivo* imaging system can reach, which is limited by tissue absorption and scattering. b) Representative *in*

vivo 3-D imaging stack of a BM cavity. The number indicates imaging depth from surface (z value). As depth increases, the cavity opens up within the bone (blue, from second harmonic generation of bone collagen). It is lined with bone cells (green, from EGFP-col2.3 osteoblasts) and vascularized with a complex but well-organized network of blood vessels (red, from semiconductor-based vascular probes pre-injected into the mouse). Visual presentation of these image stacks has been made versatile by imaging analysis programs such as ImageJ [1], as seen in c), in which a simple reslicing function offers three cross-sectional views of a BM cavity with the cross hair set as origin. d) The dark regions seen within the BM cavity in b) and c) are in effect packed with hematopoietic cells, made evident in this image by the DNA label Hoechst33342 (blue) that highlights all cell nuclei; the bone is labeled red by the calcium stain Alizarin. A blood vessel, which is not labeled, can be seen traversing the upper left corner of the cavity. e) With its submicron resolution, the *in vivo* imaging system can track single cell activity. In this image (color-coded the same way as b) and d)), the white signal belongs to HSPCs transplanted 1 day before imaging. The cell on the left had remained quiescent after homing to the BM, while the cluster on the right were progenies of a single cell that had homed and proliferated. f) Quantitative analysis of the BM microenvironment and cell activities are possible with the highly resolved optical sectioning ability offered by both the two-photon and confocal imaging mode of the imaging system. This graph describes the geographical relationship between the osteoblasts and the vasculature in the BM, plotting the Euclidian distance between the osteoblasts and the closest blood vessel in their 3D vicinity; the method with which this data is derived from the images will be described in Chapter 4. Proper optics setup and the selection of fluorescent probes go hand in hand in making morphometric analysis like this possible, in that accurate measurements require strong signal-to-noise ratio in the original image stack and a good match of the fluorescence signal from each entity to its assigned imaging channel, such that the boundaries of each are easily observed and defined. This requires the fluorophores that identify cells and vessels to be bright, not only having high absorption coefficients and quantum yields but also avoiding the wavelengths at which the tissue itself absorbs and scatters photons, exclusive to the entity they are set to label, and have a fluorescence profile that is spectrally well-confined within the detection range of their own imaging channel. Scale bar=50μm except in a), which is = 150μm.

Morphometric analysis, as the example shown in Figure 1.2 f, requires that the optics setup of the *in vivo* imaging system and fluorescent probes are not only robust themselves but also optimized for one another. Considerations pertaining to tissue optics and how it affects fluorophore selection will be discussed in sections 1.2 and 1.3. Looking ahead, the imaging probes based on semiconductor nanocrystals, which were used to label the vasculature in Figure 1.2 including the images from which the numerical data for Figure 1.2 f had been derived, have been found to be well suited for *in vivo* multiplexed imaging.

Another application for *in vivo* multiplexed imaging of the BM is the evaluation of new therapies against metastasis to the bone. Predilection for bone metastasis has been observed in both "liquid" malignancies that originate from blood cells (leukemia, multiple myeloma) and solid tumors (ex. lung, prostate, breast cancers) at later stages of the disease. Development of lesions in the bone is a sign of poor prognosis, leading to significant morbidity and mortality [125,163]. These malignant cells are known to share common trafficking pathways with normal lymphocytes and HSPCs to access the bone marrow (ex. SDF-1/CXCR4 axis [181], [180] and references), making them difficult to target with therapies without adversely affecting the "good" cell populations. It has also been known that the BM is a safe haven for certain hematological malignancies against chemotherapy due to the drug resistance conferred to these cells when in contact with the stroma; in multiple myeloma, for example, this has been contributed to both the physical adhesion of the cells (CAM-DR, for cell-adhesion mediated drug resistance) and the stromal release of soluble cytokines such as IL-6 that promote survival (SM-DR, soluble factor mediated drug resistance) [103]. Potential drug candidates therefore include reagents that 1) prevent cancer cells from homing into the BM and 2) cause the already-homed cancer cells to egress and return to the vasculature, where cytotoxins used in current chemotherapy are the most effective.

Before the advent of multiplexed imaging, these drugs and their treatment plans must be tested individually by, for example, injecting into an animal subject a single cancer cell population, pretreated *in vitro* with a specific regimen, then repeating for each drug and regimen to be tested with a different animal and comparing the imaging results. Multiplexed imaging allows simultaneous introduction of multiple pre-treated cell populations into one animal, such that the populations can compete for the same homing and engraftment sites in the BM. Competitive assays as such thus circumvent the need to interpret data from different animals, the intra-species differences among which necessarily lead to ambiguities during analysis. It also ensures that the experimental variables—including the optical setup, the health and cell cycle of the cells investigated, even the circadian rhythm of the host that is known to affect trafficking [117]—are held consistent for each drug treatment option.

1.2 The *In vivo* Challenge: Tissue Optics and the NIR spectral window

Considerations in fluorophores' optical properties, together with the spectral limitations placed by tissue optics that is highly relevant for *in vivo* imaging and shall be discussed next, restrict the number of channels that can be included in an *in vivo* multiplexed imaging system. By extension, they restrict the complexity of the biological processes one can observe and study. This limitation serves as motivation for this thesis project, which is to develop new imaging probes that are optimized specifically for use in *in vivo* multiplexed imaging. The probes will ideally have the following attributes: near-infrared (NIR; >650nm) fluorescence, bright (often expressed as the product of extinction coefficient and quantum yield), narrow and symmetric fluorescence profiles. The goal is to allow for more optical channels to be

set up within the wavelength ranges (or "windows") that are friendly for photon transmission within tissues, which fall within the near infrared (NIR) spectrum.

In an ideal *in vivo* multiplexed fluorescence imaging setup, entities to be observed are each assigned an optical channel suitable for the imaging probe that labels the entity, with spectral characteristics that is specific and exclusive to that entity alone. Often then, each imaging channel has its own excitation source and detector, defined spectrally by an appropriate optical filter or dichroic mirrors. Complexity of these imaging system setups therefore escalates quickly when the number of multiplexing channels increases. Also, the transmission cutoffs of these filters and mirrors are not infinitely sharp and low levels of photon transmission likely remain at some of the wavelengths they are supposed to block. This must be factored in when deciding on the spectral spacing between individual channels, in addition to considering the fluorophores used and the exact shape of their absorption and fluorescence profiles.

Fluorophores in organic imaging probes, which include traditional fluorescent dyes and also fluorescent proteins, often have shoulders in their fluorescence as well as absorption profiles that widen their spectral "footprint" significantly compared to the peak's full-width-half-maximum (FWHM) value, rendering them less confined in their own optical channel. Other cautions regarding fluorophore selection may be subtle. For example, the shape of fluorescence profile may vary significantly from dye to dye even when they are grouped into one commercial series (ex. the Alexa Fluor series (Invitrogen, Carlsbad, CA) [4]). Also, because commercial sources commonly plot the spectral profiles of their fluorescent products at peak absorption wavelength excitation, fluorescence below the peak absorption may be omitted in these plots but occur in reality when the excitation wavelength is hypsochromic of the absorption peak. Excitation and fluorescence profiles of fluorophores have thus been plotted as 2-D matrices in academic literature [42].

Deviations in optical properties have been observed when fluorophores are excited under multi-photon conditions. When performing two-photon microscopy, for example, while a good estimate of fluorophore's two-photon absorption peak is to double the wavelength reported in literature for single-photon excitation, organic dyes with structural symmetries (ex. rhodamines) are known to have broadened absorption profiles that are significantly shifted in wavelengths from this estimate, due to the difference in selection rules between one-photon and two-photon processes [202] and the energetic discrepancy in the vibronic states available for a given electronic transition. The fluorescence profile usually remains the same but the quantum yield may change. Literature reporting the two-photon spectral properties of common fluorophores has been published [23,176,178,193,204].

1.2.1 Tissue Optics: Absorption, Scattering and Autofluorescence

In vivo imaging presents additional challenges compared to *in vitro* imaging in that incoming and exiting photons must penetrate a finite thickness of tissue. Thus Imaging *in vivo* is often photon-limited from signal attenuation due to absorption by major tissue components (blood oxy/deoxyhemoglobin, water, lipids [58]) or scattering, which eliminates the photons and alters their direction of travel respectively. The risk of thermal damage sets an upper limit to the excitation energy. Optical properties also differ from one tissue type to another due to variations in the composition and organization of absorbers and scatterers in each tissue.

Scattering from tissues is generally considered to be intermediate between Mie and Rayleigh scattering, as the size distribution of scatterers, including cells, organelles, pigment bodies etc., is continuous. The scattering coefficient μ_s as well the reduced scattering coefficient μ_s' ($\mu_s' = \mu_s(1-g)$, where g = anisotropy factor) has been assigned to many tissue types, which differs significantly and exhibits its own wavelength

dependence [35,115,168,212]. However, as $\mu_s' \alpha \lambda^{-n}$ and n>0, imaging at longer wavelengths always lessens the effects of scattering [104,213]. Meanwhile, the absorption spectrum for major tissue absorbers must be taken into account (fat: [10,182,185]; water: [68,148]; hemoglobin: [149,162]). 95% of lipids in human fat are composed of oleic, palmitic, linoleic, stearic, palmitoleic acids [182]. While there are published absorption spectra of general live tissues, which combine the effects of major absorbers at their most common relative concentrations (ex. [159]), their accuracies, as expected, depend on the exact composition of the absorbers in the tissue type of interest.

Bone is often excluded from studies of tissue optics as the need to image the hard tissue itself is relatively rare. Imaging of the soft tissue connected the bones (such as bone marrow) often proceeds after demineralization. Bone is a strong scatterer with a significantly different refractive index (~1.56 [203]) compared to water-based tissue components (~1.3; intracellular and interstitial fluids have approximated n=1.37 and 1.35 respectively [205]).

Autofluorescence from endogenous fluorophores adds background to imaging data. Endogenous fluorophores commonly found in tissues include the adenine dinucleotides (NAD, FAD) and their reduced forms (NADH, NADPH, $FADH_2$), collagen and elastin, porphyrin and flavins, tryptophan and lipofuscin [42,188,206,209]. Most of these species fluoresce in the visible violet to green, rendering these hemoglobin-absorption wavelengths even less ideal for *in vivo* imaging. The visible red is not entirely exempt, as seen in the overall tissue autofluorescence spectrum of the skin of a nude mice [209]. Lipofuscin, an age pigment found in lysosomal bodies of phagocytized lipids and membranes, is a collection of fluorophores with wide fluorescent peak extending beyond 600nm [206,208]. NIR autofluorescence is often contributed by chlorophyll in animal diets and hence removable if needed [209]. While the spectral properties of many of these autofluorophores are available in

literature [42], the actual tissue autofluorescence during imaging is also determined by the relative composition of these autofluorophores in the tissue, as well as the physical-chemical conditions of the local microenvironment (ex. pH may lead to spectral shifts and quantum yield changes) and the metabolic states of the cells. Background from autofluorescence is therefore difficult to remove by retrospective compensation / signal un-mixing without aggressive assumptions regarding the tissue and the state of its endogenous fluorophores [193], especially when complex tissue structures are involved.

1.2.2 The NIR Windows for *In Vivo* Imaging

With tissue optics considerations in mind, the optimal wavelengths for *in vivo* imaging have been determined computationally to lie within small ranges, or "windows" (sometimes, "therapeutic windows"), within the near infrared (NIR) spectrum.

The first NIR window, which spans between the absorption peaks of hemoglobin and water, is the most well known and cited; the exact endpoints vary between literature but are usually reported to be ~650nm and ~950nm. The cause of these variations is, again, tissue-dependent absorber composition. A well-vascularized tissue, for example, may require wavelengths >650nm to ease the loss of signal due to hemoglobin absorption. Biological probes suitable for intravital use in this 1st NIR window are commercial available, despite having a smaller selection compared to the visible blue to green; *in vivo* imaging within this window and the improvements in photon penetration depth is therefore well documented (ex: [9,97,172]). Multi-photon microscopy has also contributed to the feasibility of *in vivo* imaging in the 1st NIR window by allowing NIR excitation for fluorescent dyes originally excited by visible blue to green wavelengths.

Other NIR imaging windows, more recently defined, are situated near the two local minima of the water absorption curve before 1900nm, at which water absorption spikes sharply in value. The second window, between 1000-1300nm as described by Smith et al. [173], follows the minor water absorption peak between 950-1000nm. The historical cutoff between this second NIR window and the first may be contributed by the limits in detection range of the traditional silicon-based CCD cameras, which lose sensitivity beyond 900nm. The third NIR window is between 1600-1900nm after the water absorption peak between ~1300-1600nm, as seen in Lim et al [104]. The high volume fraction of water in soft tissues (>65% [86]) explains the lack of water absorption as the best indicator of optimal *in vivo* imaging wavelengths; nonetheless, in tissues exhibiting significant wavelength-dependent scatter, the third NIR window, which has stronger water absorption, may fare better than the second because longer imaging wavelengths reduce scattering-associated loss of photons. High fat content in specific tissue types may also narrow the effective range of these NIR windows; in the ~1600-1900nm water absorption minima, for example, the local maximum of lipid absorption at 1735nm would narrow this window to ~1600-1700nm for imaging high fat content tissues [104].

NIR windows therefore only serve as guidelines for *in vivo* imaging wavelengths; the optimal wavelength(s) within each window is ultimately determined by the exact composition of the tissue type of interest (Figure 1.3). As previously mentioned, wavelength cutoffs of conventional photodetectors are additional considerations in defining imaging windows [172]. InGaAs detectors are suited for imaging further into the NIR. Ideal biological probes should therefore be able to tune to adjust to tissue type as well as address the limitations in optical sensitivities in the imaging systems.

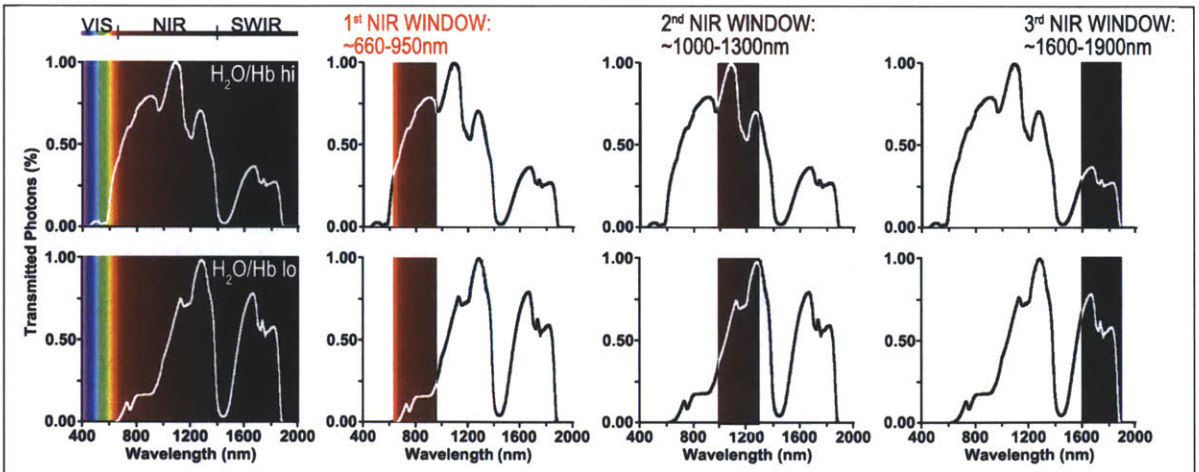

Figure 1.3: Suitability of NIR Imaging windows depends on tissue type and its components. Top row: tissue with high water-to-hemoglobin ratio; bottom row: tissue with low water-to-hemoglobin ratio, both are models reproduced from [104], assuming tissue thickness = 0.25cm and scatter is wavelength-dependent. The plots highlight how tissue types dictate which NIR window is best photons for imaging—the 1st window is only suitable for low blood content tissues, for example, and even within each window the transmission efficiency of photons can vary widely as a function of wavelength, such as the case for high blood content tissues in the 2nd window.

1.3 Selection of Biological Probes for NIR In vivo Fluorescence Imaging

While the second and third NIR imaging windows further extend the choice of wavelengths suitable for *in vivo* multiplexed imaging, biological probes optimized for use within these windows are still under development. Besides the need to incorporate fluorophores with appropriate spectral properties, biological probes for *in vivo* fluorescence imaging must perform satisfactorily in terms of their interactive behavior with the local environment.

Water solubility is the requirement for almost all biological probes, with very rare exceptions such as those designed to directly apply on hydrophobic cell membranes (ex. DiA, Invitrogen Corporation, CA). Aggregation occurs when the probes are insufficiently soluble and the resultant labeling, if any, tends to be poor and non-specific. Furthermore, after systemic injection into animals for *in vivo* labeling, these aggregates are often removed rapidly from the vasculature as part of the host's immune response (via the reticuloendothelial system, to be discussed below) or worse, may cause animal death from emboli occlusion of, for example, pulmonary capillaries. Water solubility is a concentration-dependent parameter; a probe that is soluble at 1uM in the labeling medium may not be soluble at 10uM, and while full solubility of the probe at its applied concentration is usually required for proper labeling, a probe far more soluble than needed may have trouble interacting with the entity they are designed to label.

Parameters that describe the *in vitro* environment in which fluorophore characterization is performed generally fall short of describing all the variables that determine the efficacy of biological labeling. They mostly consist of quantifiable physical-chemical variables: temperature, pH, matrix polarity and proticity (hydrogen bonding ability), viscosity, ionic strength, presence of fluorescence quenchers such as oxygen and molecules with affinity to the probes [158], while the *in vivo* environment is at once much more restrictive—for example, living tissues, including those from tumors that are known to be more acidic, rarely have pH outside 6.0-8.0 [67]—and broad in scale. Resident cell types are tissue-specific and their architecture may provide differential access to different probes (ex. via endothelial fenestrations in specific organs [150]). The cells also carry out dynamic activities that interact with the local microenvironment and can modify it over time.

Furthermore, biological activities that influence the efficacy of labeling may originate from remote tissues. Case in point, the reticuloendothelial system (RES), which

comprises of phagocytic cells at various organs including the spleen, liver and lymph nodes and clears away foreign particles and spent tissue debris from circulation, determines the clearance rate of probes introduced *in vivo* and hence, the effective concentration of probes available for labeling any tissue (not just the RES-related organs) over time. RES action on the probes is dependent on the latter's physical properties, such as size and charge, the details of which has been extensively investigated in nanomedicine and drug delivery [55,160]. Incorporation of poly(ethylene glycol) on probe surfaces has become a standard strategy to help the probes evade RES clearance as well by minimizing their adhesion to other biological molecules [16].

Despite difficulty in reproducing the *in vivo* environment *in vitro*, *in vitro* assays can help predict the probes' intravital behavior. Full solubility of the probes in physiological buffers without compromising their optical properties can be seen as the most primitive test for *in vivo* probe functionality. Incubation with commercial serum or its major components (ex. albumin) has been used to gauge the probes' interaction with blood. The most important requirement for *in vivo* biological probes—the absence of toxicities and physiological changes through direct or indirect probe-tissue interactions (ex. uptake of the probes leading to cell death for former; changing the media properties, such as shifting the pH and gettering / sequestering needed nutrients for latter)—can be tested by running viability and functional assays on cultured cells pre-incubated with the probes; these cells can belong to the same cell type to be labeled or can be macrophages that mimic the cellular component of the RES. *In vitro* confocal imaging can confirm labeling specificity for cellular and molecular probes and provide information on coverage and labeling uniformity. Fluorescence-activated cell sorting (FACS) quantifies the fluorescent intensity and uniformity and viability of large populations of labeled cells. While these tests, even collectively, cannot replace *in vivo* evaluation of the probes,

they eliminate the need for extensive animal testing and minimize mortality and morbidity in the tested animal subjects.

Sections 1.3.1 and 1.3.2 will focus on the development of fluorophores that govern the optical properties of *in vivo* NIR multiplexed imaging probes. Selection of proper methods for water solubilization and functionalization is possible only after knowing the physical and chemical properties of the fluorophore, which, if unmodified, will determine the probes' interactions with the environment.

1.3.1 "Classical" NIR Probes based on Organic Cyanines

Organic dyes with absorption and fluorescence in the visible spectra have long been available as contrasting agents for *in vivo* imaging. Equivalent products in the NIR are far fewer. Certain dye classes, such as oxazones, exhibit drastic changes in their optical properties, including their spectra and quantum yields, in response to their immediate neighboring molecules (solvatochromism). Among the dye classes less susceptible to environmental factors—resonant dyes rather than charge transfer dyes [158]—cyanines have been popular fluorophores among the commercially available bioprobes fluorescent in the NIR.

Heptamethine cyanines fluoresce above 700nm. Commercial products that make use of this cyanine class include indocyanine green (ICG), Cy7 (GE Healthcare, NJ), Alexa750 (Invitrogen, CA) and IR Dye series (LI-COR, NE). Polymethines are defined by their linear chain of multiple conjugated carbon (methine, -CH=) groups, terminated at two ends by an electron donor group and an electron acceptor group. Cyanines are cationic polymethines, their heterocyclic electron donor and acceptor groups containing nitrogen; one of these nitrogen atoms that bracket their methine chain is positively charged to induce electron pulling along the delocalized π–orbitals.

Absorption/fluorescence peaks of polymethines are largely governed by the number of vinylene (-CH=CH-) group in the chain, the addition of each causing a discrete bathochromic wavelength shift [54]. NIR cyanines generally have phenol-incorporated bicyclic or tricyclic rings (ex. indole, benzoindole) to further shift their optical spectra to longer wavelengths.

To achieve the water solubility needed for most biological applications, the bulky, hydrophobic heptamethine cyanines mostly require sulfonation of the donor and acceptor cyclic groups. The negative charges supplied by the sulfonates also prevent aggregation by repelling the dye molecules from one another. Alkyl chains may also be incorporated into the donor and acceptor ring systems, either for lipid labeling or functionalization with a terminal carboxylate group, which can in turn be esterified (ex. form NHS ester) for protein conjugation.

Heptamethine cyanines nonetheless have several drawbacks. The long polymethine chain is structurally unstable and torsional vibrations make it prone to non-radiative energy losses, causing poor quantum yield and photobleaching. Structural flexibility also leads to strong coupling between the molecules' different vibrational levels in the electronic ground-state and excited singlet state, the multiple vibronic transitions contributing to the "shoulder" on the hypsochromic side of the absorption peak and bathochromic side of the fluorescence peak.

Physical- and photostability in heptamethine cyanines has been partially ameliorated by incorporating large cyclic groups to improve structural rigidity, particularly along the methine chain [54]. Nonetheless, quantum yield of NIR cyanines rarely exceeds 30% and their fluorescence often bleaches too quickly for the longer in duration, higher excitation energy conditions required for *in vivo* imaging.

Trans→*cis* conformational changes are also known to occur in heptamethine cyanines and cause substantial shifting of their optical spectrum to shorter wavelengths [46]. Cyanines are also more restricted in their availability of wavelengths due to the discrete chromatic shift from each vinylene's addition, even if smaller spectral "stepping" can be made via modifications of the cyclic structures. Cy3, Cy5 and Cy7 in the CyDye series, for example, have identical structures other than the length of their methine chains but exhibit a 100nm difference in fluorescence peak wavelength from one dye to the next. Extending the repertoire of cyanines further into the NIR region (>900nm) for *in vivo* multiplexed imaging will likely present a significant challenge due to the severe structural instability expected in such fluorophores, especially if the polymethine chain is to be further extended.

And as is true for most organic resonant dyes, asymmetry in cyanine's spectral properties (the "shoulders" in both their absorption and fluorescence profiles) and their small Stokes shift—compared to even other organic fluorophores, such as the charge-transfer dyes coumarin—render channel separation difficult in multiplexing. Heavy sulfonation for water solubility in large organic dyes may also lead to difficulties in bioconjugation due to charge and steric effects [58].

1.3.2 NIR Probes based on Inorganic Semiconductor Nanocrystals (QDs)

The first reports on using semiconductor nanocrystals, or quantum dots (QDs), as a novel, inorganic class of fluorophores for biological probes were published in 1998 [8,27,33], five years after Murray et al. [127] reported the colloidal synthetic scheme that made possible the production of highly crystalline and uniformly sized semiconductor nanocrystals [127]. Semiconductor nanocrystals can be grown to a wide variety of shapes [92,113,140]; those with an aspect ratio of ~1 (near-spherical) are mostly used for biological imaging and will be the focus of this thesis. The

advantages of using QDs over the "classic" organic cyanines for *in vivo* multiplexed imaging include: unlimited choices of peak fluorescence wavelengths, photostability, narrow fluorescence profiles, wide absorption curves / long Stokes shifts that are especially attractive for multiplexed imaging setups, and large two-photon action cross-sections.

Colloidal syntheses of QDs are performed in organic solvents, with the growing nanocrystals capped by ligands that are commonly also surfactants—molecules with polar head groups to bond to the surface and non-polar, usually linear hydrocarbon tail to suspend the crystals in the organic solvent. The nanocrystals, in their as-made form, cannot survive as individual fluorophores in biological environments without modification of this organic "cap" to confer, at minimum, water solubility. Functional handles for probing biological units must be incorporated into the water-solubilized organic cap as well.

Inorganic nanocrystals found in biological probes are mostly composite structures of at least two semiconductor materials: the ***emitter*** in which radiative recombination occurs and the ***overcoat*** that passivates the emitter and protects it from environmental assault. For clarity's purpose, the term ***fluorophore***, when applied on QDs in this thesis, will always designate the overall inorganic structure that includes both the emitter and the overcoat, as the latter can significantly modulate the emitter's optical properties. Also, as both emitter and overcoat can be made of more than one semiconductor material, the composition gradient—i.e., fraction of each constituent material as a function of QD radius—is relevant and will be referred to as follows:

- homogeneously alloyed, in which the composition is uniform throughout
- gradient alloyed, in which the composition changes incrementally as a function of radial distance.

- *Core-shell*, in which an ultra-steep gradient composition gradient effectively separates the different materials into sublayers. When a core-shell gradient is found in the emitter and the core and shell semiconductor each supplies one type of charge carrier, the result is a Type II QD (see section 2.2).

Figure 1.4 illustrates the schematic of a QD biological probe:

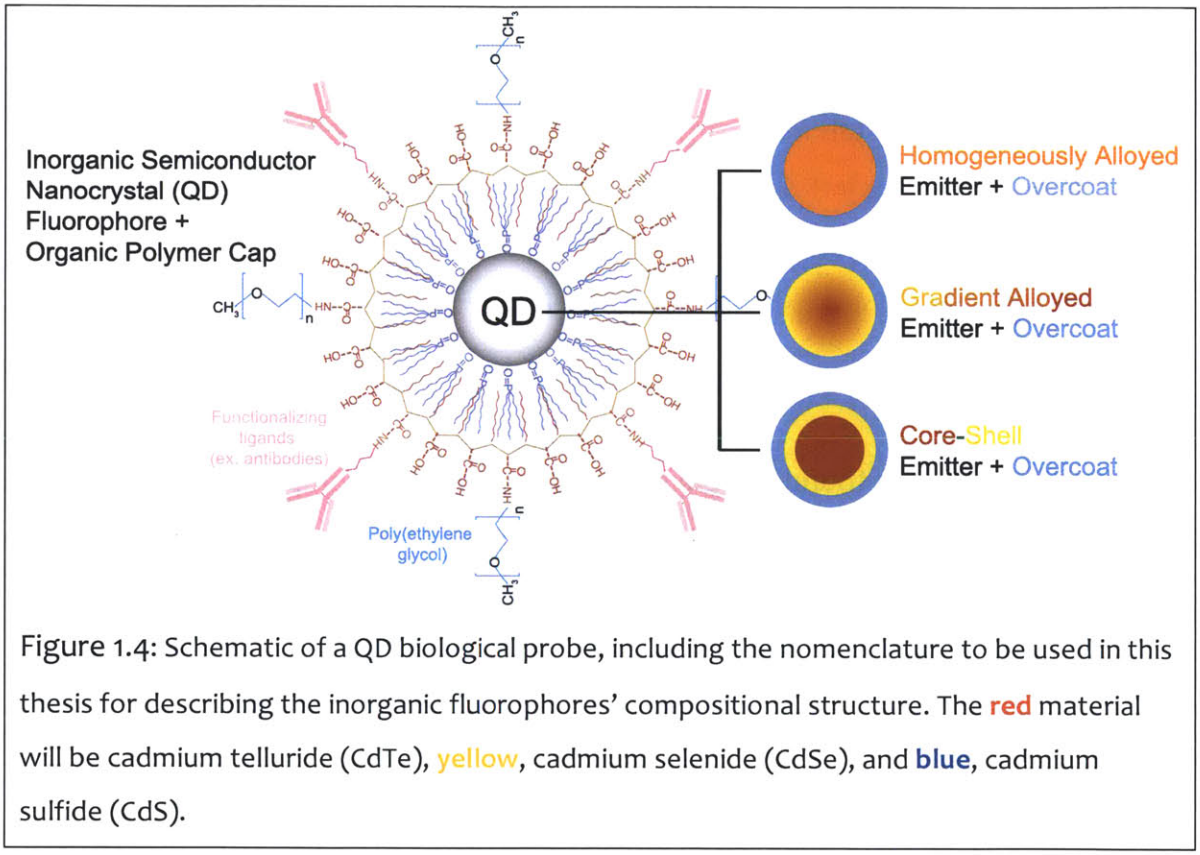

Figure 1.4: Schematic of a QD biological probe, including the nomenclature to be used in this thesis for describing the inorganic fluorophores' compositional structure. The **red** material will be cadmium telluride (CdTe), yellow, cadmium selenide (CdSe), and **blue**, cadmium sulfide (CdS).

Overcoating has become standard for QDs designed for use in biological applications. While it is often performed as a separate step from synthesis, both its chemistry and physical outcome can be seen as an extension of growth, in which monomers of a semiconductor—one with a larger bandgap and a lattice constant well-matched to the emitter—is epitaxially deposited onto the surface of a nanocrystal, the emitter itself. Overcoating serves two major purposes: i) passivation, in which it completes

the dangling bonds from the emitter at the emitter/overcoat interface and thus removes their mid-bandgap energy states that serve as non-radiative recombination centers [7], ii) protection, in which it shields the emitter from oxidizing agents (O_2, water, etc.). Overcoat therefore confers the stability required for nanocrystals to immerse in the aqueous biological environment and maintains their quantum efficiencies for *in vivo* fluorescence detection. Notation for overcoating in this thesis will be *A@B*, in which *A* and *B* denotes the overcoating and emitter material, respectively.

Upcoming chapters of this thesis will focus on the development of a NIR QD fluorophore for use in *in vivo* imaging probes, using alloyed $CdTe_xSe_{1-x}$ as the emitter material. Chapter 2 will begin with an overview of the structural and optical characteristics of QDs, followed by potential fluorescence tuning parameters that are specific to alloyed $CdTe_xSe_{1-x}$ QDs and the special considerations to be made when synthesizing and optimizing the properties of such alloyed emitter nanocrystals. New synthetic schemes for these $CdTe_xSe_{1-x}$ QDs will then be presented in Chapter 3, with emphasis on uniformity control and parameters that may affect reproducibility.

2 $CdTe_xSe_{1-x}$ Alloyed QDs for *In vivo* NIR Fluorescence Imaging

2.1 Introduction: Structural & Optical Properties of QDs

At ~10^2-10^3 atoms per nanocrystal, QDs generally have diameters in the scale of 1E1 to 1E2 nm. The ultra small physical dimensions, comparable or smaller than the Bohr radii of excitons generated during excitation, quantum-confine the electron-hole pairs. The quantum mechanical model of QDs conforms to the simple "particle in a sphere" configuration with strong confinement in all directions, provided that the surface is perfectly passivated and relieved of strain [6,7,28,87,131,133]. QDs have thus been known as "artificial atoms", or mesoscopic materials that exhibit properties intermediate between the bulk and molecular forms [7,41,52].

Quantum confinement leads to discretized density of excitonic states in QDs, with energy values dependent on both the composition-determined bulk semiconductor bandgap and the nanocrystals' diameter. The bandgap of a QD of radius r, $E_{g,r}$, is proportional to r^{-2} [131], thus increasing from the bulk bandgap value as the nanocrystal size decreases [7,41]. The shape of the nanocrystals, which changes the extent of quantum confinement in each crystal axis, and their compositional gradients (for alloyed QDs) further diversify the spectral outcome of QDs [137].

QDs are known to have narrow and symmetric fluorescence peaks [131]. This is due to the low Franck-Condon vibrational coupling factors associated with excitons in QDs, the rigid sp^3-hybridized orbitals of its semiconductor crystalline structure permitting little lattice distortion [131]. Hence, the electronic dipole selection rule suppresses the number of conduction-to-valence band transitions involving vibrational sidebands, eliminating the red "shoulder" often seen in organic dyes' spectral profile. Structural stability also confers photostability in the QDs by suppressing non-radiative internal conversions.

The width of a QD sample's fluorescence peak nonetheless deviates from the line width expected from its discretized energy states. As QD's fluorescence is size-dependent, size distribution in a population of QDs—which in a well-controlled synthesis can be limited to ~5% [127]—translates to a distribution in peak fluorescence wavelengths. However, even if each QD is identical, broadening of the emission peak from its theoretical linear profile still occurs due to spectral diffusion, in which trapped charges on or near the surface of the nanocrystals, created by energy input that can be very mild (such as room light), respond to the local environment and create a time-evolving electric field that polarize nearby excitons to form dipoles, leading to a small spectral Stark shift in each QD over time [51,52]. As an ionization phenomenon, spectral diffusion is also related to the "blinking" observed in single QDs [112,132] that compromise the quantum yield of a population [129].

The wide absorption band of QDs makes them highly attractive for multiplexed imaging. QDs' large Stokes shift is the outcome of the densification of excitonic states at energies removed from the band edge and the rapid fluctuation of their energy values as a result of short lifetimes, an outcome of the Heisenberg Uncertainty Principle ($\Delta p \Delta x < h$; or alternatively $\Delta E \Delta t < h$) [6]. Extinction coefficient of QDs is therefore larger at shorter wavelengths, as the absorption band extends away from its first absorption peak towards the UV. This allows QD probes of different fluorescence wavelengths to be excited simultaneously by a single laser source during multiplexed imaging, which greatly simplifies the needed optical setup.

Two-photon action cross section of QDs (two-photon absorption cross section σ_{2p} multiplied by the fluorescence quantum yield) is significantly higher than that of organic dyes, at the order of 1E3 to 1E5 GM (1GM=1E-50 cm^4s) compared to organic dyes' 1-1E2 GM [97,202]. As previously mentioned, multi-photon imaging allows the use of NIR excitation wavelengths for visible wavelength fluorophores, thereby

reducing signal attenuation in the excitation path; it also allows for higher resolution and less photo damage. QDs tend to have higher one-photon absorption coefficient than organic dyes as well, with typical values between 1E5-1E6/(M.cm) (QD size dependent) [98] compared to 1E4-1E5/(M.cm) for dyes (at dye absorption maximum wavelength) [64,158].

2.2 *In vivo* Imaging with QDs: Semiconductor Choices Beyond the Visible Spectra

Since Murray et al. [127] reported the colloidal synthetic scheme for highly crystalline and uniform CdE (E=S, Se, Te) nanocrystals, the protocol has been adopted for a wide variety of metal precursors, ligands and solvent systems [127,128]. Overcoating has also employed similar schemes with success [71,184]. Research has postulated the molecular mechanisms by which precursors of different element (ex. trioctylphosphine-chalcogenides (TOP-E), cadmium-phosphonate complexes) interact and become semiconductor monomers (ex. CdTe, CdSe) that either form nucleates or deposit onto the growing crystal structure. These mechanisms are often elucidated by first developing a working protocol for synthesis and then tracking the identity and concentrations of precursors and molecules that form during the reaction ([135]; [9] for InP; [179] for PbSe). Based on these studies, guidelines and strategies on controlling the process and its outcome have been established.

The first QDs created from colloidal synthesis are based on compound semiconductors made from divalent transition metals (zinc Zn, cadmium Cd, mercury Hg) and the Group VI chalcogens (sulfur S, selenium Se, tellurium Te). Referred to as II-VI semiconductors, fluorescence from these QDs, such as CdSe and CdS, usually falls within the visible wavelengths. Only with appropriate mixture of materials and

stringent control of size and architecture can II-VI QDs reach the first NIR window (~650-950nm) suitable for *in vivo* imaging.

II-VI semiconductors are therefore not the most spectrally suitable QD materials for achieving NIR fluorescence. III-V and IV-VI semiconductor families form nanocrystals that fluoresce mostly, if not completely, *within* the NIR, and without the need to mix two or more materials. Recent reviews [111,158,161] tabulated the wavelengths achieved by these QDs; the III-V family (ex. $InAs_yP_{1-y}$, $In_xGa_{1-x}P$, $In_xGa_{1-x}As$) can emit from the visible red (620nm, InP) to 1400nm (InAs), while the IV-VI semiconductors, PbS and PbSe, can fluoresce up to 1800nm and 3500nm [70,143] and even longer wavelengths are possible given their large Bohr radii (18 and 46nm respectively, compared to 5.4nm for CdSe and 7.5nm for CdTe [26]) that allow for strong confinement effects—thus each can comfortably span every NIR window suitable for *in vivo* imaging. Of note, PbTe's bandgap is greater than PbSe's ($E_{g,\ PbTe}$=0.19eV, $E_{g,\ PbSe}$=0.17eV) [94]. *In vivo* imaging with III-V QDs has been reported [9,63,85,201] and their bio-distribution determined as well [36]. *In vivo* imaging using PbS and PbSe QDs are yet to be reported.

Nonetheless, the III-V and in particular, the IV-VI family QDs have yet to catch up with the II-VI family in regards to the knowledge base and tools available for controlling synthesis and functionalizing the products for *in vivo* use. The rest of this thesis will therefore be devoted to II-VI semiconductor NIR QDs.

For *in vivo* imaging applications, CdSe, often considered the "classic" QD material, covers most of the visible spectrum with its size-determined emission from ~470-670nm [120]. Fluorescence from CdS and the Zn-chalcogenides are limited to the blue end of the visible spectrum and therefore has limited use for tissue imaging. Commercial biological probes based on CdS or CdSe emitter QDs with ZnS overcoat have exemplified the strengths of QDs—symmetric and narrow (<40nm full width

half maximum (FWHM)) fluorescence profiles, minimal photobleaching, broad Stokes' shift and large absorption cross-section.

Although CdTe QDs are capable of peak emission up to 750nm and quantum yields up to 70%, Te atoms on the surface of the nanocrystals are strongly susceptible to oxidation and act as hole traps that compromise the photoluminescence [74]. Unlike the oxidation of CdSe (as well as ZnSe and ZnTe), which is shared between the cation and the anion and is relatively self-limiting via a CdO-enriched surface, oxidation of CdTe is specific to tellurium ions, forming TeO_2 that continuously sublimes with un-oxidized cadmium [50]. The resulting degradation of the CdTe QDs' physical structure and optical properties, exacerbated by light, and the large diameters required to reach NIR wavelengths all present issues in post-synthesis processing (in particular, water solubilization), reliability and shelf-life.

NIR-emitting biological probes based on II-VI semiconductor QDs are nonetheless commercially available, the most prominent example being the QTracker series from Invitrogen (Carlsbad, CA; spectral data available on company website). Fluorescence spanning the 1st NIR window (650-950nm) from II-VI QDs was first achieved by CdTe core-CdSe shell QDs, which emitted up to 1000nm [83]; the study suggested that the spectral properties of these QDs depend not only on the size and overall composition of the nanocrystals, but also the degree of mixing between the constituent semiconductor materials, which can vary from complete (homogeneous alloy) to none (core-shell). The latter, which gave rise to what is known as a type II electronic band structure within the emitter, was key to its reaching the longer NIR wavelengths.

In the electron band diagram of type II CdTe-CdSe QDs (Figure 2.1), the conduction and valence bands (E_c and E_v) are staggered and the band offset is positioned such that the hole and the electron are quantum-confined to the core and the shell

respectively. Charge recombination must occur across the material interface during radiative decay.

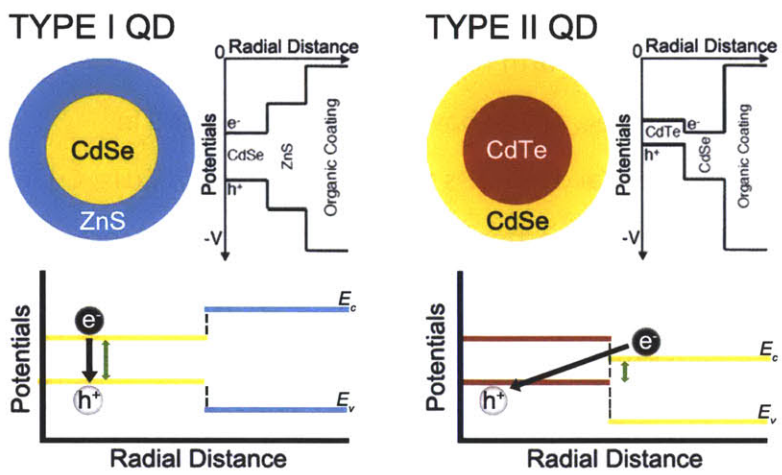

Figure 2.1: Type I vs. Type II electronic structure. In type I QDs, such as those with CdSe as emitter and ZnS as overcoat, both the conduction and valence band edge has lower energy in the inner (emitter) material. Thus both electrons and holes are generated and they recombine in this one material without having to cross a material interface. In type II QDs, such as those with CdTe core and CdSe shell, the staggered conduction and valence bands energetically favors electron and hole generation in separate materials. Recombination occurs across the core-shell interface, thus emission requires the participation of two materials. It can nonetheless generate photons with lower energy (shown in green) than the bandgap of the core or the shell. Band diagrams are reproduced from [84].

The effective bandgap in these type II QDs, modulated by two semiconductors, extends the longest peak fluorescent wavelength attainable by CdTe-core/CdSe-shell QDs into the NIR [83]. The FWHM of the fluorescence peak is nonetheless broad (74nm@ 705nm peak fluorescence for Qtracker 705 (Invitrogen, Carlsbad, CA), compared to 33nm for Qtracker 655 that is composed of CdSe-ZnS QDs). Quantum yield is also compromised due to long radiative lifetimes resultant of spatial separation of charge carriers, which promotes non-radiative decay with interfacial crystalline defects serving as non-radiative recombination centers [83]. Interfacial defects also trap charge carriers at mid-bandgap energy states prior to radiative recombination, giving rise to a "red tail" in the emission profile that is not unlike the

"shoulder" in organic dye spectra, with the same effect of rendering the fluorescence spectra more difficult to confine within a single optical channel during multiplexed imaging.

Syntheses of CdTe+CdSe QDs with more uniform compositional mixing—the homogeneous and gradient alloy $CdTe_xSe_{1-x}$ QDs—have also been reported in literature. Closely related to the gradient alloyed QDs are the quasi type-II CdTe-CdSe QDs; in quasi-type II QDs, one of the charge carriers remains confined in the core or shell material while the other carrier delocalizes [74]. While homogenous alloys are ideal Type I structures, gradient alloys may be more practical to synthesize due to differential kinetics between the precursors, in this case, of the chalcogen Te and Se that are to be alloyed. Regardless of the degree of alloying, $CdTe_xSe_{1-x}$ QDs have not been commercialized, although they too, are capable of achieving wavelengths in the NIR [13]. They will be the focus of the rest of this chapter as well as Chapter 3 of this thesis.

On a final note, the II-VI mercuric chalcogenides (HgE, E=S, Se, Te) have longer absorption and emission wavelengths compared to the cadmium equivalents and their fluorescence extends well into the NIR range; HgS QDs can emit up to 800nm and HgTe QDs, 1800nm [161]. Application of these QDs in the biological context is not considered, however, due to the extreme toxicity and environmental concerns regarding the use and disposal of mercury.

2.3 $CdTe_xSe_{1-x}$ Binary Alloy QDs

Over the past decade, several groups have prepared and characterized $CdTe_xSe_{1-x}$ alloyed QDs as NIR emitters [13,14,73,77,144]. While $CdTe_xSe_{1-x}$ QDs do not have the

staggered bandgap that is responsible for Type II CdTe core-CdSe shell QDs' NIR fluorescence, optical bowing in bulk $CdTe_xSe_{1-x}$ (more details in section 2.3.2) suggested the potential of $CdTe_xSe_{1-x}$ QDs to surpass CdTe QDs in their longest emissible wavelength. Meanwhile, by alloying / physical mixing of the constituents CdTe and CdSe and eliminating the material interface to be crossed for radiative recombination, $CdTe_xSe_{1-x}$ alloyed QDs are expected to share the attributes of type I QDs such as CdSe—robust quantum yields and narrow and symmetric fluorescence profiles. These qualities, together with their NIR fluorescence and photostability, would make $CdTe_xSe_{1-x}$ QDs the ideal fluorophore candidate for *in vivo* imaging.

Unlike QDs composed of one semiconductor material such as CdSe or CdTe, therefore, $CdTe_xSe_{1-x}$ has three major parameters controlling its fluorescence rather than one (assuming shape is constant and isotropic): size, composition, composition gradient. This is akin to having a 3-D parameter space to search for a robust synthetic scheme for $CdTe_xSe_{1-x}$ QDs compared to a 1-D line for single-semiconductor QDs. Achieving uniformity in the products' physical and optical properties also presents a much greater challenge—not only because of the diversity of outcomes, but also because of the multitude of additional factors that must be considered when working with the $CdTe_xSe_{1-x}$ alloy system. Some of these factors stem from the bulk properties of the alloy, others, the nanoscale dimensions of QDs and still others, the practical concerns and limitations in the colloidal chemistry used for QD synthesis. These factors will be detailed in the remainder of this chapter.

2.3.1 Structural overview of $CdTe_xSe_{1-x}$ QDs: Lattice Structure and Surface Reconstructions.

QDs made of $CdTe_xSe_{1-x}$ are expected to crystalize in the hexagonal close-packed wurtzite structure assumed by bulk and nanocrystalline CdSe or the cubic zinc blende structure of bulk CdTe [144]. Wurtzite and zinc blende structures are identical in their

tetrahedral bonding to local neighbors but differ in their plane stacking sequence along the (1 1 1) direction (wurtzite: ABABAB…; zinc blende: ABCABC…). Thus, compared to the isotropic zinc blende, wurtzite loses structural symmetry in its *c*-axis, which coincides with the direction of most aggressive growth in wurtzite QDs. This anisotropy in growth direction, which stems from difference in surface energy among the crystal facets, allows for syntheses of QDs with various shapes; by modulating the selection and availability of monomers and ligands, nanocrystals from spheres (aspect ratio ~ 1; minimal shape anisotropy) to elongated rods to branched structures have been produced [113].

Controlling the surface of the QDs, which enumerates a significant fraction of the total number of atoms per nanocrystal (30% in a 5nm diameter CdSe QD, for example), is vital to developing a proper synthetic scheme. Surface reconstruction reduces the number of dangling bonds, minimize electronic energy and electrostatic energy via the rearrangement of charged, inorganic surface atoms [114]. Only with the presence of organic ligands, however, can full passivation be attained; ligand binding is nonetheless modulated by surface reconstructions that first determine the facets to which they bind. Relatively availability of each ligand during synthesis and its controlled removal during flocculation also control the outcome of ligand binding; decreasing the acid input during synthesis, for example, has been shown to switch the prominent ligands on CdSe QDs from strong acids to phosphine oxides and selenides [90]. Densely-capped ligands with strong electron donating abilities are well suited to transfer their electrons to passivate the surface states [134]. While ligands modulate the shape of nanocrystals via the facet-dependent variations in surface energy upon ligand adsorption / binding, the shape of the ligands themselves has been linked to their ability to passivate; cone-shaped ligands (such as trioctylphosphine, or TOP) have been reported to encourage the growth of small QDs with small radii of curvature, while linear / rod shaped ones (alkyl amines and acids) favor larger QDs [134].

Various reports have investigated the relationship between the QDs' crystal lattice, their surface reconstructions and the strength and coverage of their surface ligands' binding. QD shape anisotropy is a well-known consequence. Via first-principles modeling, atoms on the surface of CdSe QDs have been shown to have different propensity to passivation via self-healing (rearrangements of surface atoms [151]) and ligand binding leads to growth rates and surface strain and energies that are all facet specific [114,156]. The details can be summarized as follows. On the non-polar, Cd+Se containing $(10\bar{1}0, 11\bar{2}0)$ planes, the Cd atoms, with their $sp^3 \rightarrow sp^2$ change in hybridization, donate electrons to the Se dangling bonds and mechanically relax the surfaces, the energy of which is further lowered by good coverage of strong Cd-complexing ligands including phosphonic and carboxylic acids. Hence, these facets are the most inactive in QD growth [156]. On the other hand, the polar planes along the *c*-axis, which carry alternating layers of Cd and Se atoms, are strained and not so easily passivated. The (0001) plane, which is preferentially terminated by Cd, is partially stabilized with a vacancy and an incomplete coverage of ligands (~75%). Meanwhile, the high surface energy of the Se-preferred $(000\bar{1})$ plane, which cannot be passivated by any ligands, is largely responsible for anisotropic growth. The influence of ligand binding on the mechanical strain within the entire QD lattice has also been studied; for example, Meulenberg et al. [119] reported compressive strain exerted by hexadecylamine (HDA) on the lattice of CdSe QDs and tensile strain by trioctylphosphine oxide (TOPO), the extent of both decreasing as the nanocrystals' size increases.

Surface reconstructions can also cause non-stoichiometry. Despite the predicted Cd vacancy for (0001) plane relaxation, elemental analysis of actual cadmium chalcogenide QDs from various synthetic schemes has reported Cd-enriched products (ex. [41,114,123,196]) with positively charged surfaces. Related to surface charging is that ligand binding occurs as L- or X-type. L-type ligands do not donate their charges

and include trioctylphosphine oxide (TOPO) and amines that were first described as QD ligands by Kuno et al. [93], while X-type ligands are dative and are, in most cases, deprotonated phosphonic and carboxylic acids that complex strongly with ionic cadmium atoms on the surface. Abundance of X-type ligands compared to the L-type may encourage non-stoichiometry by their stabilizing effect [123].

Both the lattice structure and organic / inorganic surface reconstructions may participate in the fluorescence tuning of $CdTe_xSe_{1-x}$ QDs, as will discussed in the next section. While it is beyond the scope of this project to provide experimental evidence on how and to what extent each of these factors, often atomic in scale, contributes to spectral modulation, understanding these factors is helpful for predicting how the spectral characteristics of $CdTe_xSe_{1-x}$ QDs may shift when changes are applied to their synthetic schemes.

2.3.2 Fluorescence Tuning in $CdTe_xSe_{1-x}$ QDs: Optical Bowing, Strain-induced Spectral Shifting & Surface Effects

Optical bowing tunes bulk $CdTe_xSe_{1-x}$ fluorescence in a nonlinear manner. Vegard's law, which predicts the bandgap E_g for an alloy of composition A_xB_{1-x} as a linear function of composition x

$$E_{g,A_xB_{1-x}} = E_{g,A}x + E_{g,B}(1-x) \qquad (Eq.1)$$

is modified with $b(x)$, the bowing function to give a second order relationship:

$$E_{g,A_xB_{1-x}} = E_{g,A}x + E_{g,B}(1-x) + b(x)x(1-x) \qquad (Eq.2)$$

$b(x)$ is smaller than 0 eV for $CdTe_xSe_{1-x}$, $ZnTe_xSe_{1-x}$, $Cd_yZn_{1-y}Se$ and $Cd_yZn_{1-y}Te$ binary alloy systems, thus they fluoresce at longer wavelengths at certain alloy compositions compared to what is predicted by Vegard's law [69,146]. Proposed physical mechanism behind optical bowing is the local ordering of the alloy's atomic constituents, which differ in atomic radii, electronegativity and lattice constants, to allow for structural relaxation of the lattice [22,146].

Bailey and Nie [13,15] were the first to hypothesize that the NIR wavelengths observed in alloyed $CdTe_xSe_{1-x}$ QDs is caused by the optical bowing effect. In the series of homogeneous and gradient alloy QDs they produced, the longest wavelength achieved was 825nm for a 6.5nm diameter, $CdTe_{0.66}Se_{0.34}$ QD, compared to ~740nm for the same sized CdTe [13].

Estimates of the expected fluorescence wavelength of $CdTe_xSe_{1-x}$ QDs of diameter D can be made if $b(x)$ is assigned the near composition-independent optical bowing factor of bulk $CdTe_xSe_{1-x}$, -0.94eV [69,146], and assuming the 1st absorption peak energy, E_{abs1}, shares the bowing characteristics of its corresponding fluorescence energy. From *Eq.2*, E_{abs1} of $CdTe_xSe_{1-x}$ QDs of diameter D can then be formulated as, in eV:

$$E_{abs1,CdTe_xSe_{1-x}}(D) = E_{abs1,CdTe}(D)x + E_{abs1,CdSe}(D)(1-x) - 0.94\,x(1-x) \qquad (Eq.3)$$

This assumes that the alloy is fully homogeneous. Estimates of $E_{abs1,\,CdTe}$ and $E_{abs1,CdSe}$ can be made from published fitting curves that describe CdTe and CdSe QD diameters as a function of their 1st absorption peak wavelength λ, determined from experimental data ([195] for CdTe; [126,127] for CdSe):

$$D_{CdTe} = 9.8127 \times 10^{-7}\lambda_{CdTe}^{3} - 1.7147 \times 10^{-3}\lambda_{CdTe}^{2} + 1.0064\lambda_{CdTe} - 194.84 \qquad (Eq.4)$$

$$D_{CdSe} = 3.149\times 10^{-9}\lambda_{CdSe}^{5} - 8.482\times 10^{-6}\lambda_{CdSe}^{4} + 9.119\times 10^{-3}\lambda_{CdSe}^{3} - 4.891\lambda_{CdSe}^{2} + 1.0387\times 10^{3}\lambda_{CdSe} - 1.3975\times 10^{5} \quad (Eq.5)$$

Figure 2.2 shows the resultant plot of the predicted 1st absorption peak wavelength for $CdTe_xSe_{1-x}$ QDs as a function of nanocrystal diameter *D* based on the above calculations:

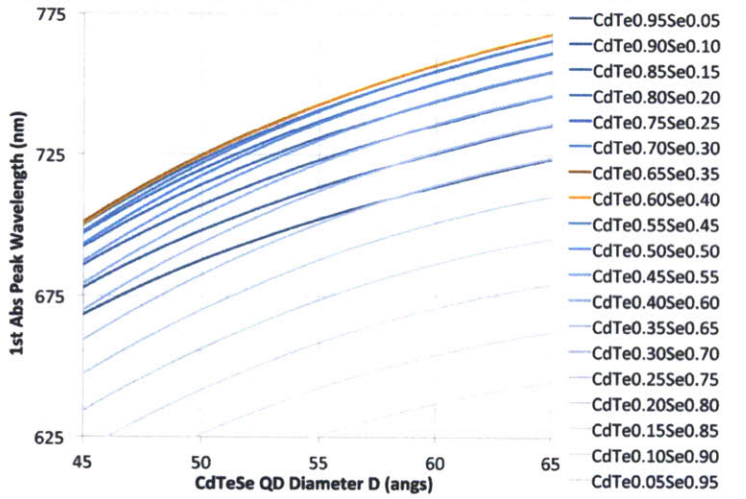

Figure 2.2: Estimated 1st absorption peak wavelength of $CdTe_xSe_{1-x}$ QDs as a function of QD diameter *D* and at different compositions *x*, assuming that optical bowing behaves identically in QDs as in bulk. The longest wavelength is attained when x=0.60-0.65 (shown in orange).

While optical bowing has been cited as the cause of non-Vegard's rule compliant fluorescent wavelengths in QDs composed of $CdTe_xSe_{1-x}$ as well as other alloyed systems, attempts to model optical bowing in nanocrystals has nonetheless given contradictory results. For example, Zhu et al. determined that the bowing function *b(x,D)* increases rapidly from -0.83eV to 0 as *D* shrinks to <10nm for zinc blende $CdTe_{1-x}Se_x$, suggesting that the effects of optical bowing diminish in nanocrystals [200]. However, Mourada and Czycholl applied an alternate model on $Cd_yZn_{1-y}Se$ and reported that optical bowing actually becomes more pronounced as *D* decreases to <5nm [124].

It should hence be noted that optical bowing, as a bulk phenomenon, assumes the alloy under observation is completely homogeneous with no surface or interface effects, which is unlikely to hold true for nanocrystals. Whether the alloy is compositionally homogeneous within each QD depends on the synthetic scheme; also, the large surface–to-volume ratio of each QD, as well as the fact that QDs almost always have at least one material interface (emitter / overcoat), means that any local lattice ordering that gives rise to optical bowing within the nanocrystals must be influenced by the mechanical strain at the surface and interface(s), a consideration that is less than vital in the modeling of the bulk.

Related to optical bowing, then, is the more recent report that mechanical strain by means of core-shell lattice mismatch can yield QDs with fluorescence tunability far exceeding the extent permissible by optical bowing in the bulk material [173]. In determining the distribution of mechanical strain inside a QD, shell deposition on a core (or overcoat on an emitter) can be regarded as epitaxial growth of a film on a substrate; while in 2D systems, the substrate is often significantly thicker than the film and thus considered infinite in size and fully relaxed mechanically (strain $\varepsilon_{substrate} \rightarrow 0$) [60], the core in QDs, with similar dimensions as the shell, is expected to be a compliant substrate that can distort its lattice to accommodate the shell. The strain due to lattice mismatch is hence shared between the core and the shell and the extent each undergoes is determined by the elastic modulus of the respective materials [109].

The stiffness of Cd and Zn chalcogenides is inversely related with its unit cell volume [78], which, in turn, is inversely related with its bandgap energy. The shell material, which has a larger E_g, is therefore expected to be stiffer than the core. If the compliant substrate hypothesis holds true for nanocrystals, then the core would sustain more of the elastic strain from lattice mismatch and experience a spectral shift. While compressive strain in the core lattice alone would lead to shorter

fluorescent wavelengths, elevation of the core's conduction band position (which accounts for most of the change in E_g value in II-VI semiconductors [102]) and the lowering of E_c in the stretched shell's may become sufficient to yield a type II electronic structure.

Although the reasoning above mainly concerns core-shell structures, fluorescence modulation by mechanical strain is expected to extend to gradient alloyed $CdTe_xSe_{1-x}$ QDs, which are Te-rich at the center and Se-rich towards the surface. Such gradient-alloyed QDs can be seen as intermediates between homogeneously alloyed QDs and core-shell QDs; as their compositional gradient steepens, gradient-alloyed $CdTe_xSe_{1-x}$ QDs should converge to type II CdTe core-CdSe shell QDs in structure and optical properties. Thus like core-shell QDs, gradient-alloyed QDs should also experience mechanical strain, if only to a lesser extent, within its lattice structure and exhibit the accompanying spectral shifts, the amplitudes of which are determined by the compositional gradient within each nanocrystal.

Consequently, prediction of the spectral properties of $CdTe_xSe_{1-x}$ QDs is far from straightforward. Although mechanical strain and / or optical bowing are expected to play a role in modulating the fluorescence of $CdTe_xSe_{1-x}$ QDs, their effects are difficult to gauge and dependent on synthesis conditions.

Surfaces and interfaces may also augment the set of variables in $CdTe_xSe_{1-x}$ fluorescence tuning given their contributions to the mechanical stain of QDs. If both optical bowing and strain-based bandgap modulations originate from lattice distortions, then "outside" layers of material with different lattice constants epitaxially grown on the $CdTe_xSe_{1-x}$ emitter—for example, a $Cd_yZn_{1-y}S$ overcoat—can further alter the lattice strain within the emitter, rendering the latter's optical properties even less predictable. Meanwhile, the configuration of surface atoms and their passivating ligands influences the mechanical strain and the surface

stoichiometry of the QDs, as previously discussed. While Puzder et al. [151] claimed these factors had negligible influence on the bandgap of CdSe QDs, in a modeling study [24], Cd-rich and Te-rich CdTe nanoclusters that are dominated by surface atoms have been predicted to have different HOMO-LUMO gap size due to differences in mechanical relaxation. Experimentally, band gap modulation by surfaces and interfaces has yet to be reliably determined, in part due to the sensitivity of both the surface atoms and the ligands to post-synthesis processing steps required for structural and elemental analysis; flocculation ("crash out"), for example, which cleans up the QDs, may strip off surface cadmium-ligand complexes.

2.4 Process Control in the Colloidal Synthesis of $CdTe_xSe_{1-x}$ QDs

Reproducibility of the synthesis of $CdTe_xSe_{1-x}$ QDs is therefore critical for understanding the behavior of this alloyed system in nanocrystal form and optimizing its structural and optical properties. Even minor differences in size and composition may translate to a substantial shift in composition gradient and fluorescence wavelengths.

$CdTe_xSe_{1-x}$ QDs also lack "gold standard" absorption profiles, which have served as fast metrics of nanocrystal size and quality for single material QDs. This is due to the need to specify the composition gradient in addition to size and composition in creating such standard, and the only truly reliable means to determine the composition gradient is by carrier lifetime measurements. Major publications on $CdTe_xSe_{1-x}$ QDs have reported vastly different absorption spectra from well-defined [13,144] to barely resolved features [77]. Given that high quality single material QDs are characterized by sharp, well-defined absorption features that shift in a known relationship to nanocrystal size ([126,127] for CdSe; [195] for CdTe) and type II QDs

have diminished absorption band edge and often smoothed features [83], gradient-alloyed QDs, even those that are highly crystalline and uniform, are expected to have less defined absorption peaks—but the extent of loss in definition is likely influenced by both the composition gradient, which is inherent to the nanocrystals, and morphological non-uniformity or poor crystallinity, which are reversible by improved synthetic schemes.

The practical consequence of having no simple models that describe the effects of factors other than size on $CdTe_xSe_{1-x}$ QDs' bandgap tuning is that *in situ* selection of fluorescence wavelengths during synthesis is difficult to perform. During the growth of single-material CdSe or CdTe QDs, for example, the size and fluorescence peak wavelength increase incrementally, allowing the endpoint of determined in real time by monitoring the band edge or fluorescence peak location in time intervals. Synthesis of alloyed QDs may not enjoy such convenience in wavelength tuning. Non-linear shift in fluorescence peak over the course of growth has been observed during the synthesis of $CdTe_xSe_{1-x}$ QDs for this project. In quasi type II CdTe-CdSe QDs, which may be viewed from a compositional perspective as gradient alloyed nanocrystals, sub-monolayer thickening of the CdSe shell has been reported to push the spectral characteristics significantly into longer wavelengths, presumably due to carrier delocalization [38] but can also be contributed by Te-to-Se chalcogenide exchange at the surface and/or lattice ordering within the emitter. The high temperature phase during synthesis may also relax intraparticle strain via annealing, inducing further atomic rearrangements in the lattice. In addition, composition gradients in alloyed QDs are generally unpredictable from their synthetic schemes. Non-unity reaction yields can cause the composition of the QDs to deviate from the composition of starting precursors and depending on ligand choice and the balance it maintains between kinetic- and sterically driven growth, what is left behind can be exclusively the slower precursors (Se in this case) or a mixture that is closer in composition to the precursor input.

$CdTe_xSe_{1-x}$ synthesis protocols therefore demand specificity that is beyond what is needed for describing the synthesis of single semiconductor QDs. Critical parameters, such as temperature, concentration and purity of starting chemicals, the timing and rate of precursor introduction, are already routinely reported in detail for single material QD syntheses. Still, it is known that successful reproduction of any published synthesis protocol is more an exception than a rule even in the hands of experienced QD chemists. Variations in outcome have shown themselves to be more pronounced in alloyed QD systems. While the causes of these variations may be traced to obscure differences in reaction conditions, such as temperature ramping and cooling rates (dependent on the setting of the temperature control) or pressure of the inert gas and its quality (ex. concentrations of oxygen and water); it has been established that impurities found in starting chemicals can exert a significant effect on the morphology of the synthesized QDs (further discussion in section 2.4.2.1). The high temperature conditions of synthesis also encourage side reactions and formation of byproducts.

Another potential source of ligands and monomers—and a very difficult to control one—are the QDs themselves in the growth solution. The growing, changing QDs are sinks of monomers and ligands that dynamically reverse their role to act as sources when precursor concentrations run low, thus acting a crystalline "buffer" that maintains an equilibrium between free and bound monomers. Maintaining a single population of QDs at all times during synthesis—i.e., suppressing any nucleate formation after an initial "burst" of nucleation events—eliminates the complexity in process control due to the presence of multiple precursor sinks and sources. It also aids in ensuring reproducibility of the alloyed QDs which, unlike single material QDs, cannot "uptake" late nucleates (in size focusing, to be described in more detail in section 2.4.1.2) without the risk of modifying its optical properties.

In the upcoming section, the means to maintain a single QD population over the course of a single-semiconductor QD synthesis will first be introduced. How these mechanisms and their theories apply to alloyed QD synthesis—and in particular, how they can be compromised by the variations in composition among the alloyed QDs—will be discussed next. This is followed by a closer look at the role of chemical impurities.

2.4.1 Maintaining a Single Population of QDs

2.4.1.1 *Achieving Uniformity in Single Semiconductor QD Systems @ Nucleation*

Evolution of organometallic monomer concentrations in the colloidal synthesis of QDs follows closely the nucleation and growth model described by La Mer and his colleagues, based on their studies of self-nucleation in hydrosols and aerosols [95,96] (Figure 2.3). Monodispersity of the nucleated phase is achieved when nucleation occurs as a "burst", i.e., within an infinitesimal amount of time.

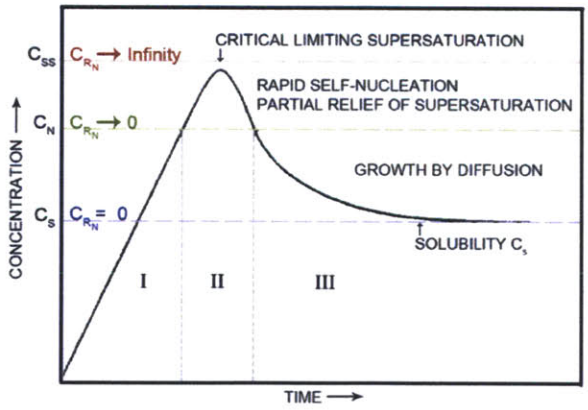

Figure 2.3: La Mer's nucleation and growth model, reproduced from [96]. C_S is the saturation concentration of precursors, C_N, the critical concentration of nucleation. R_N is the rate of nucleation. Stage II is the nucleation phase and Stage III is the growth phase. Monodispersity of nucleates is achieved when the precursor concentration approximates C_{ss}, the limiting state of supersaturation at which the rate of nucleation, R_N, approaches infinity and creates all nucleates within a single, infinitesimal "burst" of time; ideally then, Stage I is also bypassed such that the monomer concentration never passes through the range at which slow nucleation occurs. C_{ss}, dependent upon the reaction

conditions, should be sufficiently dilute such that once a single burst of nucleation events has occurred, it falls under C_N but above C_s; the supersaturation then drives the growth of the nucleates but allows no further nucleation.

In QD synthesis, monodispersity of nucleates is further ensured by the initial high temperature, fast injection of organic metallic precursors, which not only allows for the spike of concentration to near C_{ss} and bypassing Stage I as defined in Figure 2.3, but also lowers the temperature (which shifts the whole curve upward) and expands the volume of the growth solution (hence, suppresses the precursor concentration by more than the amount exhausted by nucleation). Uniformity of nucleate growth is encouraged subsequently by supplementing precursors to sustain their concentration at supersaturation and allow for size focusing, the latter to be discussed next. Other changes in the growth solution that can encourage uniformity are more subtle and difficult to quantify; for example, release of by-products that changes the viscosity or interact with the nanocrystals (ex. TOPO's oxidation into phosphinic and phosphonic acids under sustained heat [192]).

2.4.1.2 *Achieving Uniformity @ Growth in Single Semiconductor QD Systems: Size Focusing & Oswald Ripening*

As the key mechanism for maintaining monodispersity during the growth of single-semiconductor QDs, size focusing refers to the narrowing of QD size distribution that occurs when the size of individual growing QDs universally exceeds a critical radius, determined by the concurrent free monomer concentration in the reaction vessel. High monomer concentrations encourage size focusing by suppressing the value of the critical radius, hence size uniformity is achieved either by ceasing the reaction when precursors are not yet exhausted or via continuous introduction of free precursors [137]. As a dynamic process, size focusing not only preserves the narrow

size distribution of a monodisperse population of nucleates but actively drives the current population to the narrowest size distribution—thus it has the potential to "repair" a starting nucleate population with less than ideal uniformity.

Surface energy of the nanocrystals has been determined to be the driving force behind QD size focusing [155]. The Gibbs-Thompson (or Kelvin) effect delineates the relationship between solubility of a particle and its surface energy, which is due to the increase in chemical potential when local curvature increases:

$$S_r = S_b \times e^{\frac{2\sigma V_m}{rRT}} \qquad (Eq.6)$$

Where S_r, S_b are, respectively, the solubility of a particle of radius r and its corresponding bulk material; σ, the specific surface free energy; V_m, the particle's molar volume. R and T are the gas constant and temperature [138].

The reverse process to size focusing is Ostwald ripening, which describes the *widening* of particle size distribution due to the exhaustion of free precursors in solution. Small crystals, which are kinetically favored to nucleate, are lost at the expense of larger ones that are thermodynamically favored to grow. Oswald ripening has been modeled based on diffusion-limited growth, which assumes the interface between the particles and their matrix acts as an efficient source/sink for monomers. Specifically, the LSW theory describes the growth rate of a particle of radius r using Fick's first law as a starting point, then takes into account the Kelvin effect as well as the resistance from the adsorbed layer on the particle surfaces [45,79,207] to give rise to a equation of the following form [138]:

$$\frac{dr}{dt} = K\left(\frac{1}{r} + \frac{1}{\delta}\right)\left(\frac{1}{r^*} - \frac{1}{r}\right) \qquad (Eq.7)$$

δ is the thickness of the adsorbed layer; K is a constant proportional to the diffusional coefficient; r^* is the critical radius at which solubility of the particles is equal to the free monomer concentration in solution and increases in value when the free monomer concentration decreases. One important assumption of the LWS competitive growth theory specifies that the particles (i.e., the QDs) and bulk phase (the growth solution) must have identical compositions [207]. According to *Eq.7*, as growth proceeds and monomers are depleted, the rise in r^* (and consequent drop in $1/r^*$) leads to the smaller particles having a negative growth rate and dissolving while larger ones continue to grow in their expense. This competitive growth phenomenon thus widens the size distribution of the overall population.

Size focusing occurs, on the other hand, whenever enough monomers are present such that all particles are in the positive growth regime ($1/r^* - 1/r > 0$). Metal-ligand precursors supplied late during growth initiate focusing as well as those introduced at or before nucleation [138]. Size focusing by late injection of precursors also allows independent control of precursor concentration for nucleation and for growth. However, even if the precursor concentration is kept below the critical concentration for nucleation (C_N), it has been known that nucleation can still occur in the form of magic-sized nanoclusters (MSNCs), which are ultra small, ultra stable nanocrystals; their properties and effects on synthesis will be detailed in section 2.4.1.4.

Last but not least, the size focusing point, at which the QD population is at or near its narrowest size distribution, has been observed to coincide with maximum quantum yield of the nanocrystals. The same study hypothesized this phenomenon to be due to the near monomer-QD equilibrium achieved at the size focusing point, which leads to less atomic exchanges between the QDs and the solvent and allows for optimal QD surface reconstruction, improving both quantum yield and photostability [153].

2.4.1.3 *Achieving Uniformity Post-Synthesis in Single Semiconductor QD Systems: Flocculation*

Flocculation (or crash-outs) extracts the QDs from their growth solution—the solution and suspension of unused precursors, ligands, surfactants and byproducts of reactions at the end of synthesis and overcoat. Two countering forces determine if flocculation occurs: Van der Waals forces, from induced dipole / induced dipole attraction that draw neighboring nanocrystals together, and steric repulsion, in which the ligands extending from the QD surface entropically and enthalpically repel the particles from one another and suppress aggregation [126]. A solvent that suspends QDs single nanocrystals shields the interparticle charge interactions; subsequent addition of a miscible non-solvent reduces the repulsion force and causes the QDs to form a flake, or "floc". The turbid media is then centrifuged and the supernatant decanted to collect the pellet of nanocrystals, which can be re-suspended in the solvent for another round of cleanup or proceed to the next processing step such as overcoating or water solubilization [128]. Solvents and non-solvents of choice for QD flocculation are therefore dependent on the organic cap of the QDs. The hydrocarbon tails of most QD surface ligands result in the choice of non-polar, hydrophobic liquid hydrocarbons (ex. hexanes, toluene) as solvents and the alcohols and ketones (ex. methanol, isopropanol, acetones), which are of intermediate polarity, as non-solvents. Strongly polar solvents, as well as over zealous addition of medium polarity non-solvent and repetition of the flocculation procedure, are known to strip away the organic cap and causes irreversible aggregation and loss of fluorescence.

One notable application of flocculation for single-semiconductor QDs is size-selective precipitation. Larger QDs tend to aggregate first upon addition of non-solvents due to their higher polarizability [51], which in turn creates stronger inter-particle Van der Waals attraction. Partial flocculation of the QDs therefore yields a pellet that is

enriched in larger-sized QDs. A QD population can hence be divided into a series of subpopulations, each of a progressively smaller mean diameter, by adding the non-solvent in increments, centrifuging and decanting the supernatant that is free of the largest subpopulation.

2.4.1.4 *Nucleate Heterogeneity & Magic-Sized Nanoclusters (MSNCs): Special Considerations for Alloyed QD Synthesis*

Early nucleates of alloyed QDs are expected to exhibit compositional heterogeneity as long as the competing precursors that give rise to each constituent semiconductor (ex. TOP-Se versus TOP-Te in $CdTe_xSe_{1-x}$ synthesis) are present and are both sufficiently reactive to participate in nucleation. Even if the precursors are identical in reactivity and diffusive properties, statistics alone is sufficient to generate a compositional distribution. Small nucleates, in particular, can have a significant compositional spread, wider if the competing precursor incorporation rates are close to equivalent—this can be modeled using binomial distribution with the relative incorporation rates converted to the probability *p*. These nucleates with different compositions then serve as templates for growth, their lattice constants in all cases resisting compositional changes to minimize epitaxial strain that expends energy. Growth rates also differ, thus nucleate heterogeneity translates to a wide range of composition as well as size over time. Meanwhile, differences in reactivity and steric effects among competing precursors cause selective precursor exhaustion, which leads to evolution of the composition of nucleates forming at one infinitesimal time point to the next.

Nucleation has been known to occur over the course of growth even under optimized synthesis conditions, in the form of ultra small nanocrystals (1-2nm) with discrete and defined numbers of atoms known as the magic-sized nanoclusters (MSNCs). The formation of MSNCs has been ascribed to their exceptional structural

stability and hence, low chemical potential compared to the free monomers in solution [140]. Each "species" of MSNCs—of one size or number of atoms—corresponds to a closed-shell atomic configuration and does not evolve gradually in size or optical profile during growth as QDs do; rather, a MSNC population "jumps" from one species to the next until it outgrows the largest cage configuration, at which point it behaves like regular QDs. Size uniformity within each species of MSNCs also translates to sharp, well-defined features in the absorption spectrum.

MSNCs based on CdTe, CdSe and CdS and their optical absorption band edges corresponding to each family of close-shell atomic configuration have been reported [49,91,196]. A family of homogeneously alloyed $CdTe_{0.5}Se_{0.5}$ MSNCs with doublet absorption peaks at 520 and 524nm has also been described [191]. Their caged atomic configurations have also been elucidated: CdSe MSNCs, for example, lack the reactive $(000\,\overline{1})$ Se-terminated and (0001) Cd-terminated surface planes; instead, it is "caged" within facets identical to the less reactive nonpolar $(11\,\overline{2}\,0)$ planes that are preferentially stabilized by ligands on CdSe QDs [157].

Although MSNCs are essentially defined by their singular, thermodynamically stable cage structure, they are known to exhibit spectral variations according to synthetic conditions. This is believed to be caused by the strong effects on lattice strain imposed by different surface ligands, given that the surface takes up the majority of atoms in these ultra small nanocrystals. Thus while absorption band-edges have fixed values for a given species of MSNCs synthesized with a given synthetic scheme, MSNCs of the same material and size but synthesized in different solvent-ligand systems vary in their spectral properties [49]. Furthermore, MSNCs capped with different ligands also merge into the continuous growth phase of "regular" QDs at different wavelengths, as shown in the Table 1:

Table 1: Variations in absorption band edge among reported CdTe and CdSe MSNCs.		
Material	Solvent-Ligand System	Wavelength, absorption band-edge (nm)
CdTe	Nonanoic acid, Decylamine, TOP	445, 488, 506 [196]
	Hexylphosphonic Acid, Hexadecylamine, TOPO	425, 470, 505, 557, 606 [43]
CdSe	Nonanoic acid, Dodecylamine, TOP	330, 360, 384, 406, 431, 447 [91]
	Diisophosphinic acid, Hexadecylamine, TBP	441, 446, 490 [49]

That MSNCs can retain their ultra-stable configurations at large diameters / long wavelengths further cloud the distinction between MSNCs and QDs. Thus rather than treating MSNCs as an inorganic impurity that is highly distinguishable and easily removable, MSNCs must be treated as dynamic (and potentially QD-similar) populations that interact and compete for resources by being in the same precursor pool as the major QD population.

MSNCs generally pose few problems to the synthesis of single semiconductor QDs. Although they may lead to significantly faster precursor exhaustion, which is remediable by precursor injections mid-growth, MSNCs and the QDs that mature from them should remain the smallest-sized in the growth solution and therefore, the fastest to re-dissolve when Ostwald ripening occurs. This prevents them from "catching up" or taking over the major population of QDs by growing in its expense. Size selective flocculations can also remove them. The major QD population also does not suffer from compositional perturbations when they incorporate the re-dissolved precursors from the MSNCs.

On the other hand, MSNCs, when present in significant quantities, can prove detrimental to controlling the synthesis of alloyed QDs. Size focusing is no longer a reliable "crutch" for repairing non-uniformity for two reasons. First, alloyed QD

syntheses do not meet an important assumption of the LWS competitive growth theory that specifies that the particles and solvent (i.e. the growth solution) must have identical compositions [207]. Size-dependent solubility (S_r, *Eq.6*) also assumes identical specific surface energies (σ), but alloyed QDs are likely to exhibit a small degree of surface compositional heterogeneity. Thus the relationship described between QD size and growth rate *dr/dt (Eq.7)*, which drives the size focusing process in single-semiconductor QD synthesis, may no longer apply. Secondly, MSNCs' dissolution during Ostwald ripening, which often instigates the need to size focus, can change the effective composition of the growth solution from which the major QD population continues to draw its precursors. This is because MSNCs may be compositionally distinct from the major QD population if they nucleate after the initial nucleation stage, after significant material-selective precursor exhaustion has occurred. The composition gradient within the major QD population is then perturbed, potentially giving rise to more compositional non-uniformity as the precursors preferentially deposit onto whichever QD subpopulation that has the most active surface in the reaction vessel.

Even if the MSNCs do not affect the properties of the major QD population, removal of MSNCs by flocculation presents more challenges in alloyed compared to single-semiconductor systems, as will be discussed in the next subsection. While the inability to remove MSNCs effectively can potentially be resolved by increasing the resolution of selective flocculations (protocol detailed in section 3.5.3.2), the approach is time consuming and lowers reaction yields.

For simplicity's purpose, the term "MSNCs" in the subsequent sections in this thesis will refer to both MSNCs and the extraneous QD populations they grow into after leaving the caged configuration phase.

2.4.1.5 *Composition Effect on Selective Flocculation: Special Considerations in Alloyed QD Synthesis*

Size-selective precipitation is part of the original CdSe QD preparation scheme that yields the <5% size variation that is widely quoted in literature—pre-floccuation size distribution has been noted to be ~10% [128]. However, size is unlikely the only parameter that controls the flocculation rate in alloyed QDs. Flocculation, as previously described, occurs due to a shift of balance towards the Van der Waals attractive forces between the QDs from the steric repulsion offered by their surface ligands. Van der Waals forces are dependent on polarizability, a molecular property that is in turn related to the macroscopic bulk dielectric constant of the material via the Clausius-Mosotti relationship; the calculation is tensor-based, dependent on the crystal structure, its electric field and also quantum size effects [20]. Thus while the exact mathematical relationship may not be equivalent, the dielectric constant can serve as a useful predictor to how polarizability may change according to composition. Studies on bulk $CdTe_xSe_{1-x}$ alloys have revealed that the dielectric constant as a function of composition x features a similar "bowing" as the alloy bandgap E_g, with its maxima at the same location as E_g's minima, at Te composition x~0.6 [69].

Studies on the flocculation of "soft particles"— hard particles with terminally-anchored polymer chains—provide insights on the parameters affecting steric repulsion [186]. QDs can be modeled as soft particles with ligands as terminal polymers on the hard semiconductor crystals. Parameters involved in the modeling include particle size, thickness of the adsorbed polymer, degree of interpenetration between the solvent and the polymer layer, coverage, molecular weight, folding of the polymer on the particle. A theta solvent is "ideal" in that the polymer coils naturally in their random walk dimensions; most solvent causes the polymer to expand or collapse upon itself on the particle surface. MSNCs lack the reactive crystal

facets that are also less protected by ligands, thus their ligand conditions also differentiate them from the major population. Compositional heterogeneities can affect the surface polymer cap in that surface tellurium ions are much more prone to lose their TOP ligand than the selenium ions, which decreases polymer density or alternatively, leads to the enrichment of surface Cd and its ligands for stabilization. The size and shape distributions may also change; complications in flocculation that arise from shape differences alone are evidenced by the intricate steps required to separate a batch of *single-semiconductor* QDs of various shapes [113].

If combining every aforementioned considerations regarding uniformity at nucleation, growth and flocculation, gradient-alloyed $CdTe_xSe_{1-x}$ QDs should have a better chance in achieving uniformity than homogeneously alloyed QDs, as both their nucleates and surface termination should approach single semiconductor in composition (CdTe and CdSe respectively): the former encourages the growth of a more uniform major population, the latter, flocculations that may show less dependence in composition heterogeneities via a more uniform polymer cap. Overall, the considerations as described above further justify the need for tight process control and proper planning of the synthetic scheme for alloyed QDs. In addition to seeking more aggressive methods to minimize nucleate heterogeneity, Ostwald ripening should be suppressed at all times and any replenishment of precursors must be well paced to suppress nucleation.

2.4.2 Impurities in Colloidal QD Synthesis

In this thesis, the term *impurities* will refer to both the extraneous chemical species introduced "from the bottle" as well as byproducts formed in reactions during synthesis, including those pertaining to QD nucleation and growth and side reactions. They have been known to affect the outcome of colloidal QD synthesis by producing

strongly coordinating ligands (ex. TOPO's oxidation into phosphonic and phosphinic acids), unanticipated precursors (ex. H_2S and H_2Se) and other molecules that may not interact with the nanocrystals directly but modulate the physical properties of their growth solution, resulting in changes in precursor solubilities and the extent of steric hindrance as the precursors approach the QD surface (ex. coordination polymers based on phosphonic acids and amines). The following subsections will describe the examples in further details.

2.4.2.1 *Impurities as Adventitious Molecular Species in Starting Chemicals*

Impurities in starting chemicals can modulate the properties of the QDs much more than their weight percent suggests, especially when the impurities have lower molecular weights (thus more moles of chemicals for a given weight) compared to the pure chemical and/or exhibit stronger affinity to the coordinating metal, and/or when the starting chemical in which they are found is needed at high concentrations for syntheses.

Impurities found in trioctylphosphine (TOP) and its oxide (TOPO) have been among the most widely attributed cause of non-reproducibility in QD synthesis [189], possibly due to their strong thus apparent effects on the kinetics and the size and shape of II-VI nanocrystals synthesized. The consequences of impurities are best appreciated in the context of the form and function of the pure chemical. TOP's main function is to act as the coordinating ligand as well as a liquid carrier for the chalcogens (mainly Se and Te). It is also a weak reducing agent (compared to dialkylphosphines) for the divalent transition metal, easing its separation from its ligand such that it can react with the chalcogen to form a semiconductor monomer [179]. Tributylphosphine (TBP), also a common chalcogen ligand for QD synthesis, is structurally and functionally analogous to TOP. The oxide of TOP, trioctylphosphine oxide (TOPO), often constitutes a significant volume of the growth solvent while

acting as a relatively weak but stabilizing X-type coordinating ligand [93]. TOPO has therefore been termed a "coordinating solvent", in contrast to the "non-coordinating solvent" (but not necessary inert; see below) 1-octadecene (ODE), the use of which for QD synthesis has also become common place [75,101]. TOPO is polar and is among the least reactive of phosphorus compounds, with a bond energy of ~128kcal/mol for $R_3P=O$ [154]. The oxygen atom may be exchanged into another chalcogen, commonly sulfur (R3P=S ~90s kcal/mol). TOPO also increases the lability of the chalcogens.

Common impurities in commercial grade TOP and TOPO (≥90%) have been well investigated [190]. Acid impurities in TOP and TOPO such as octylphosphonic acid, di- and mono-octylphosphinic acid, much like the free acids intentionally introduced into synthesis, substantially slow the kinetics of QD nucleation and growth and change the size, shape and nucleate concentration of the nanocrystal products [62,90,189]. The apparent impact they elicit on synthesis and its non-reproducibility has prompted the switch to using higher purity TOP and TOPO and adding phosphonic acids in known amounts to mimic the effects of these impurities. Because TOPO and TOP are usually introduced in large qualities—often up 10-fold in molar concentration—compared to the amount of acids intentionally introduced, they can increase the effective concentration of acidic ligands in the synthesis by a significant fraction via the impurities they carry. For example, a 90 *weight %* purity TOPO can carry up to 20 *molar %* of acidic impurities, if one considers the molecular weight of octylphosphonic acid (OPA)'s molecular weight (194 g/mol) is ~50% of TOPO's (387 g/mol); thus a synthetic scheme using 5:1 TOPO: OPA and with acids constituting half of TOPO's impurities would therefore still end up with a 25% increase in the total amount of acid ligands actually introduced into the reaction vessel.

Secondary phosphine impurities in TOP, specifically, dioctylphosphine, have been known to enhance the reactivity of TOP-Se precursor solutions upon coordinating

with chalcogen atoms [53]. As dioctylphosphine is not commercially available, its effect has been mimicked by the addition of other secondary phosphines into synthesis. Introduction of even a small amount of diphenylphosphine has been shown to significantly increase the conversion yields of phosphine-chalcogens [179].

2.4.2.2 *Impurities as Byproducts of Side Reactions*

The high temperatures required for QD synthesis as well as the presence of many precursors and ligands, including impurities, create an environment conductive to unintentional chemical reactions. These side reactions can generate byproducts that modulate the growth of the nanocrystals—a very simple case is the reported oxidation of TOPO under sustained heat, forming phosphinic and phosphonic acids [192], or the condensation of two octylphosphonic acids (OPAs) into P,P'-(di-n-octyl) dihydrogen pyrophosphonic acid (PPA) that binds even more strongly to QDs compared to OPA itself [90,105]. More complex cases exist and the extent of their influence on synthesis and post-synthesis processing is not fully understood. Two examples will be described in this section: 1) the formation of hydrogen chalcogenides, which are highly reactive precursors (more so than phosphine-chalcogens), and 2) the formation of phosphonic acid coordinated polymers, which act as ligands and have been known to affect the post-synthesis processing of QDs.

2.4.2.2.1 Formation of Hydrogen Chalcogenides

The role hydrogen chalcogens (H_2E; E=S, Se) play in "phosphine-free" QD synthesis as gaseous chalcogen precursors formed *in situ* has been explored in literature [76,194]. Sulfur, and to a lesser extent, selenium, have been known to react with alkanes, alkenes, carboxylic acids and primary amines to form hydrogen sulfide (H_2S) and hydrogen selenide (H_2Se) at the temperature range (>200°C) pertinent to QD

synthesis. These interactions are therefore potential sources of inconsistencies in QD syntheses, in particular when large volumes of alkenes such as 1-octadecene (ODE) are used as non-coordinating solvent. Impurities in alkenes, which are generally other hydrocarbons including alkanes, branched isomers or alkenes of different lengths, are likely to exhibit different reactivity against the chalcogens; sulfur has been shown to yield different amounts of H_2S when heated in different but similarly structured hydrocarbons as the solvent [194]. Primary amines, which are added in significant quantities in many QD syntheses, may facilitate the formation of H_2S and H_2Se to the extent that their purities may matter in synthetic schemes that are more sensitive to batch-to-batch variations, such as those for alloyed QDs.

In alkanes, sulfurization first removes the secondary hydrogen, followed by pyrolysis to form alkenes at concentrations proportional to the hydrocarbon chain length [29]. The overall reaction rate is faster for longer hydrocarbon chains that eject electrons more efficiently; however, the size and shape of the hydrocarbons have also been reported to make little difference beyond pentane [40].

Sulfur's interactions with alkenes (olefins) have been studied in depth, as olefinic hydrocarbon networks, cross-linked by disulfide bridges, are effective lubricants [57]. Notably, tertiary phosphines (such as TOP) are known catalysts for the initial sulfurization of olefin's double bond, allowing the process to occur at >160°C [81]. The formation of H_2S is related to the formation of close-ringed, octatomic sulfur (S_8) that forms at high temperatures. Se also forms Se_8 [142]. Radical terminals of fragmented S_8 rings attack the double bonds of alkenes (as opposed to electrophilic addition reactions by sulfur) to form polysulfide products R_{sat}-S_x-R_{sat}, R_{sat}-S_x=R, and R=S_x=R, where R' is the saturated version of olefinic R, and S_x is a linear polysulfide chain. In linear mono-olefins (such as ODE), moderate temperatures (>100°C) is sufficient to initiate the process. Polysulfides further decompose via S-S bond breakage into H_2S and thiols [56] when the temperature is maintained >140C.

Polyselenides have been proposed to be the selenium source for phosphine-free CdSe QD synthesis [76].

Sulfurization also occurs in the presence of functional groups. Sulfurization of oleic acid and their esters have been reported, yielding networked molecules with their functional groups intact [57]. Primary amines open S_8 rings to form polysulfide ion chains in their presence, the ease of which depends on the basicity of the nitrogen atom; secondary amines thus only has limited faculty and tertiary amines, none. Overtime and even at room temperature, amine-sulfur solutions also break down into thioamide and H_2S [44].

2.4.2.2.2 Acids & Coordination Polymers

Acids are the strongest coordinating ligands for the divalent transition metal ions (cadmium, zinc) in QD synthesis. Phosphonic and carboxylic acids are the two major families of acids employed; metal-carboxylate complexes are more reactive than metal-phosphonate complexes as the less acidic carboxylic acids are weaker chelators [140,157].

The mechanism by which metal-carboxylates and metal-phosphonate act as precursors ("precursor conversion") in QD synthesis has been elucidated [135]. The two types of complexes are described as differing in binding strength; they share identical coordination chemistry with the acid ligands, forming the same bi-dentate linkage to the metal ions. Recent papers have, however, alluded to the presence of a "coordination polymer" when phosphonic acids but not carboxylic acids, free or bound, are introduced for synthesis [105,135]. This polymer is close to insoluble in the growth solvent [135] and flocculation is inefficient in its removal, causing difficulties in modifying the organic cap of the QDs afterwards for water solubilization [177].

The structure of metal-carboxylates and metal-phosphonates therefore invites further examination. Literature has detailed the coordination chemistry of transition metals (emphasizing on zinc and cadmium) with carboxylates and phosphonates, most of which based on studies of the complexes using IR spectroscopy and calorimetry. As metal phosphonates are used for the synthesis of (CdS@)$CdTe_xSe_{1-x}$ QDs, the discussion below focuses on these metal salts. Information of the metal carboxylates can be found in Appendix 5.2 for comparison.

Monoalkylphosphonates of divalent metals, in particular zinc and cadmium, form puckered polymer sheets of the metal-phosphonate network that can be stacked via interlamellar Van der Waals interactions into crystals, sheets, or lamellae, structures that have been dubbed inorganic Langmuir-Blodgett films [30,141]. Zinc-phosphonate complexes can have down to four coordination sites while cadmium is typically six-coordinated [59,141]. In *n*-coordinated phosphonates, the metal ion is held by *n-1* phosphonate oxygen atoms in plane to create the ionic network; most of the oxygen atoms are shared with neighboring metal ions (bridging bi-dentate linkage) but for one that coordinates to that metal ion alone [141]. Both the organic alkyl chain from the phosphonic acid and the remaining coordination site, which extends away from the plane, control the sheet-to-sheet distance. The latter site is hydrated in the presence of water [66,187] but can otherwise bind to other molecules; of particular interest to QD chemistry is that amines have been known to bind to the site and act as "pillars" between the metal phosphonate polymer sheets [30,141].

Requirements on the amines forming intercalation compound with cadmium-phosphonate are 1) they are primary alkyl amines, with their α-carbon free of branched structures, and 2) the phosphonate's hydrocarbon side group is not too bulky—ex. linear with no aryl groups [31]. Steric considerations extend to the metal

ion: the amines must be in vapor phase for intercalation into zinc phosphonates but can remain in solution for cadmium phosphonates [31].

On a related note, phosphinic acids, as a key impurity of (TOPO) (ex. as dioctylphosphinic acid [189,190]) that modulate QD nucleation and growth, has been shown to assume a polymer chain configuration [187] when coordinated with divalent metals.

Reaction conditions for many synthetic schemes of cadmium-chalcogenide QDs favor the formation of ultra-bulky, amine-pillared phosphonate coordination polymers—the absence of water, the use of (primary) alkylamines, the amines being close to their boiling point at nucleation temperatures and vaporizing in significant amounts. While the amines are weakly bound and subject to loss over time and at the re-introduction of water, they can add substantial bulk to the coordination polymer and contribute to its insolubility in the QD growth solution, as well as making their removal during crashout difficult with its long alkyl chain.

3 Synthesis & Processing of (CdS@)$CdTe_xSe_{1-x}$ Alloyed QDs: The Protocols

3.1 Introduction

This chapter will present the synthetic and processing schemes of (CdS@)$CdTe_xSe_{1-x}$ QDs. Outcome of these protocols will be detailed, and justifications and potential pitfalls for the steps taken will also be described. Selection of the coordinating/TOPO-based chemistry for QD synthesis stems from the strong knowledge base developed for this chemistry in the Bawendi Lab.

Prior to introducing the protocols, data from early biological experiments using $CdTe_xSe_{1-x}$ QDs synthesized from as-purchased, lower purity chemicals is hereby presented as the starting point of the work described in this chapter. The problems associated with these data illustrate the need for well-controlled, reproducible schemes for taking these alloyed nanocrystals beyond "proof-of-concept" to truly application-ready. Details of the equipment used for QD characterizations and imaging can be found in Appendix 5.1.

Figure 3.1 shows cell-labeling experiments using the first generation of water-soluble $CdTe_xSe_{1-x}$ QDs developed for this project. Confocal microscopy revealed endocytotic uptake of the probes, pre-treated with the cell delivery peptide PEP-1 (Chariot ™ Protein Delivery Reagent, ActiveMotif, Carlsbad, CA), by the multiple myeloma cell line MM.1s. These nanocrystals had no overcoat as the attempt to overcoat yielded morphologically poor QDs, with highly diverse shapes and sizes. Water solubilization, attained via 40%octylamine-polyacrylic acid encapsulation [210], created sufficient probes for cell labeling experiments but the chemical yield was extremely low (1-2%), the majority being lost as aggregates. These probes also proved to be non-reproducible, particularly at the water solubilization stage that had near-zero yields;

loss of nanocrystal uniformity at overcoating also persisted regardless of protocol changes.

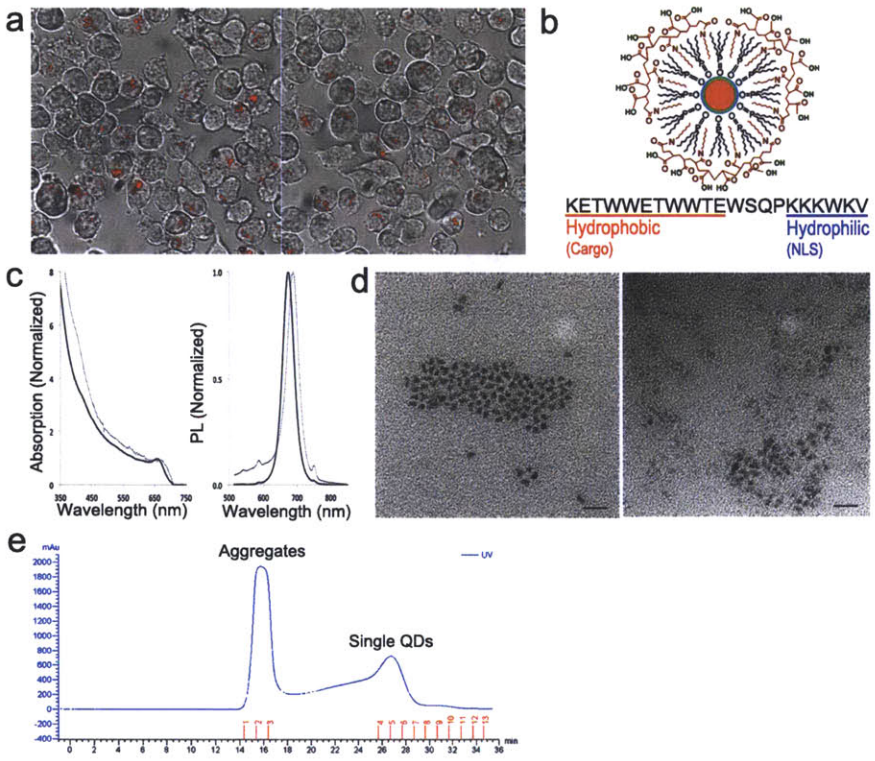

Figure 3.1: Live cell labeling and imaging experiments using the earliest generation $CdTe_xSe_{1-x}$ QD probes, encapsulated with 40% octylamine-poly(acrylic acid) and the cell penetrating peptide PEP-1. MM.1s were cultured in 10%FBS RPMI and labeled as adherent cells, washed with phosphate-buffered saline and imaged immediately. Pre-treatment of probes with the cell delivery peptide PEP-1 and its incubation with cells proceeded according to manufacturer's instructions for low molecular weight protein delivery in 6mm well, using ~1ug of the water solubilized QD probes as the starting material. Quantum yield of the probes was at 35%. a) Confocal images of the labeled cells at 100x, each of the 2 frames capturing an area of 0.25mm*0.25mm. Fluorescence was attained via 488nm argon laser excitation and detected through a 590nm long pass filter. Red signal indicates the presence of endocytosed QDs inside the cells. b) Schematic of a QD with the amphiphilic 40% octylamine-poly(acrylic acid) polymer coat and the peptide sequence of PEP-1. Ideally, once PEP-1 enters a cell, the hydrophilic Nuclear Localization Sequence (NLS) breaks off and targets the nucleus while the hydrophobic region, associated with the cargo (the QDs in this case) via hydrophobic interaction, remains in the cytosol. c) Absorption and photoluminescence (PL) of the QD cellular probes (**solid purple**). A fraction of the same sample underwent an unsuccessful CdS overcoat, the spectral profiles of which are shown in dotted lines. Of note, the fluorescence

signal was significantly elevated at wavelengths shorter than the peak while the peak itself shifted little in position; this was later determined to be caused by MSNCs "hidden" in the emitter population being selectively overcoated. d) 68kx TEM images of the $CdTe_xSe_{1-x}$ QDs before (left) and after (right) overcoating. The "before" sample appeared somewhat uniform, despite showing signs of early pod growth. MSNCs in the sample were not evident in this image. Meanwhile, the "after" sample fared extremely poorly in shape and size uniformity, with a significant fraction of the nanocrystals being smaller than the starting emitter population as they had likely originated from MSNCs formed during synthesis. Scale bar=20nm. e) Size separation by gel filtration chromatography (GFC) of the water-solubilized $CdTe_xSe_{1-x}$ QDs. UV absorption was used to detect QDs exiting the column. Aggregates that left the column early in fraction 1-3 presented only a small fraction of the total loss of QDs via aggregation, most of which had been removed during pre-GFC centrifugal filtering; fraction 4-6, which contained single QDs, was collected for cell labeling.

Figure 3.2 shows *in vivo* vascular imaging data with $CdTe_xSe_{1-x}$ QDs intravenously introduced into a mouse. These vascular QD probes also lacked an overcoat and suffered high loss to aggregation during water solubilization with 40%octylamine-poly(acrylic acid). Coupling of poly(ethylene glycol) for evading *in vivo* RES clearance was unsuccessful as well, partly due to low chemical yield (<2%) in the water solubilization step. The absence of PEG on these probes resulted in their *in vivo* uptake by macrophages residing in the bone marrow, which was observable using *in vivo* confocal microscopy.

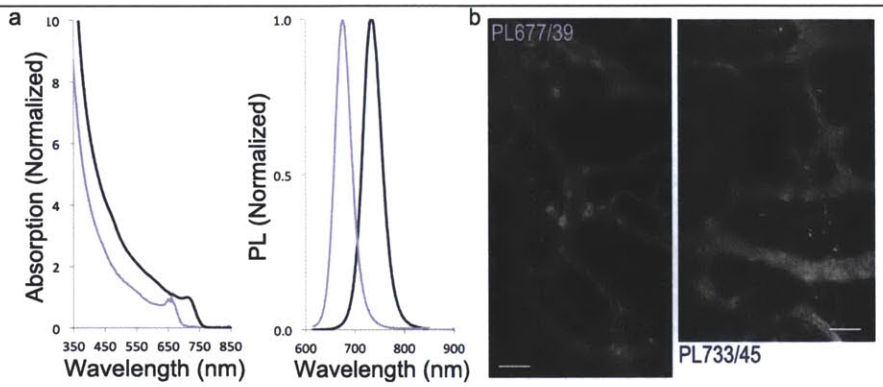

Figure 3.2: *In vivo* vascular imaging experiments using the earliest generation of $CdTe_xSe_{1-x}$ QD probes, encapsulated by 40% octylamine-poly(acrylic acid). a) Spectral profiles of the samples; QY of PL677/39 is 12%, decreased from 35% prior to water solubilization. b) *In vivo* confocal imaging of the murine calvarial bone marrow vasculature, after injecting ~80pmol of the probes into the tail vein of a BALB/c mouse. This amount was known to be sufficient for vascular visualization when commercial non-targeting Qtracker 655 (Invitrogen, Carlsbad, CA) was used (see Figure 1.2). 633nm HeNe laser excited the QDs, the signal of which was detected with a 650-760nm band pass filter. Uptake of the probes by macrophages, which fluoresced as bright spots in the bone marrow space between vessels, was especially evident in the PL677/39 sample that had undergone a failed attempt to couple methoxy-terminated PEG5000 onto the probes. Scale bar=50um.

These problems prompted the overhaul of the early synthesis and processing protocols. Very high purity chemicals were introduced to improve reproducibility, which was needed to determine the root causes of these failures. Difficulties in overcoating and water solubilization would eventually be found to be interconnected, and more importantly, originate from issues hidden within the previous step of probe preparation—namely, the synthesis of $CdTe_xSe_{1-x}$ emitter QDs. MSNCs that manifested during emitter synthesis as well as other uniformity issues would require tight process control of all steps of nanocrystal preparation (including flocculation) as well as the use of only highly pure chemicals to eliminate. While the current generation of (CdS@)$CdTe_xSe_{1-x}$ QDs still need further optimization of its overcoating scheme to achieve consistent stability in water, it has been cleared of all

problems associated with non-monodispersity. The resulting nanocrystal morphology, uniformity, reproducibility and workability during post processing including water solubilization collectively show promise for their becoming truly application-ready.

3.2 Purifications of Starting Chemicals for QD Synthesis

Purification of starting chemicals precedes the making the precursors and synthesis. Starting chemicals used for this project, while all 97% or above in purity, still contain inconsistent impurity compositions that render syntheses irreproducible when the source of the chemicals is switched to a different production lot and/or a different manufacturer. In developing the purification protocols, efficiency and ease of purification is also taken into consideration; industrial methods reported in literature are often geared towards very low purity starting chemicals and are too tedious for laboratory use.

Appendix 5.3 is dedicated to the purification protocols of TOPO, OPA, HDA, Squalane and Squalene, and TOP. Discussions on how these protocols are developed and precautions in their implementation are also included in that section. The choice of tools is also described—in particular, the temperature controller and its settings must be similar to what is specified to reproduce all protocols to be described, including those for purification, for precursor solution preparation and last but certainly not least, for synthesis.

3.3 Metal-Ligand Complex Formation

3.3.1 Making TOP-Chalcogenides

TOP-chalcogenides are prepared by simply mixing chalcogen pellets (Te powder 99.999% Puratronic (Alfa Aesar, Ward Hill, MA); Se shot 99.999% Puratronic (Alfa Aesar, Ward Hill, MA); sulfur 99.998% trace metal basis (Sigma Aldrich, St Louis, MO)) and TOP (purchased and purified as described in Appendix 5.3.5) and stirring in an air-free environment until the pellets are dissolved. While using low heat (up to 60°C on a heat plate) can speed up the solubilization process especially for making TOP-Te, all TOP-E solutions made for this project are created under room temperature conditions. This, again, is to ensure reproducibility.

As the ligand for Group VI metals, the tertiary phosphine TOP controls the degree and relative rates of incorporation for tellurium and selenium (and sulfur, for overcoat). Selenium and tellurium have also been suggested to be more labile and reactive in their phosphine form than as a metal itself [47,154]. Bond energies of different tertiary phosphine-chalcogenides have been published [32], with bond strength between the phosphorus and the chalcogen atom decreasing as one goes down Group VI, i.e. $E(P\text{-}S)>E(P\text{-}Se)>E(P\text{-}Te)$. However, TOP- and TBP- sulfide and selenide solutions are in effect composed only partially of the metal-ligand complex, with the chalcogen atoms present also in their free form. This is evidenced by the gel-like consistency of saturated TOP and TBP solution of sulfur and selenium (2.2M and 4.0M, respectively), in contrast to the highly crystalline form of purified phosphine chalcogenides [154]. Saturated TOP-Te solutions cannot be prepared, with the exception of tri(*tert*-butyl) phosphine-Te); most trialkylphoshine-tellurides have reactive rates < 50% [165].

The possible difference in reactivity between free and complexed chalcogen atoms and the unknown effects of energy input in modulating the relative ratio of the two

forms prompt the need to specify room temperature preparation for the TOP-E precursors. At room temperature, TOP-Se and TOP-S of concentrations up to saturation (2.24M) can be prepared with prolonged stirring, while the maximum concentration attainable for TOP-Te is ~1.0M. TOP-Te is stored not only in air-free conditions as the other phosphine-chalcogenides but also in the dark.

3.3.2 Making saturated sulfur solution in 1-octadecene (ODE-S)

ODE-S was introduced as a sulfur precursor for SILAR overcoating [100] at a low concentration of 0.04M. For this project, the ODE-S solution is made saturated, starting with 1.0M sulfur; the concentration after filtering is however estimated to be <0.1M. The protocol for making this solution is made specific as the coordination chemistry between ODE and sulfur remains poorly understood, and the formation of polysulfides is expected to be dependent on at least the temperature.

95% 1-octadecene from Fluka and sulfur 99.998% trace metal basis are purchased from Sigma Aldrich (St Louis, MO). As the major impurity in ODE (b.p.=314°C @ 760mmHg) is reportedly hexadecene (b.p.=284.8°C @ 760mmHg) [2], a degassing step has been included. It is advisable to degas the ODE prior to sulfur addition in the future.

1. Weigh out 2.565g sulfur and 80mL ODE and transfer to flask.

2. Degas the flask content at room temperature until base pressure is reached. Then, slowly ramp the degassing temperature towards 120°C—sulfur should melt at 115°C—and hold for ~10minutes until base pressure is reached. The sulfur is likely all dissolved and the solution should be yellow in color.

3. Cool the flask under vacuum to ~70°C, at which all sulfur should precipitate and the ODE is once again colorless.

4. Switch to N_2, set the Variac to 70% power and ramp the temperature to 180°C, which should take 10 minutes to reach with the proper temperature controller setting. Hold the solution at 180°C for another 10 minutes. The solution should turn yellow, then darken into orange.

5. Cool to 60°C and transfer into a N_2-filled flask, which is then transferred into the glove box.

6. Allow the solution to settle, during which sulfur precipitates from the solution. Filter with a medium glass frit inside the glove box; the solution should remain clear but orange-hued for at least six months afterwards.

3.3.3 Making cadmium-octylphosphonate salt precursors in trioctylphosphine (Cd-OPA in TOP)

In literature, metal-acid salt complexes that act as Group II precursors have been prepared both during synthesis and as a separate step prior to synthesis. In the latter case, a stock solution is prepared for use as both nucleation and mid-synthesis precursor supply (for size focusing). Among the commonly reported metal-acid salt complexes, the methods of making stocking solutions of cadmium and zinc oleate in 1-octadecene are the most well known [139,140]. These stock solutions are easy to use; sedimentation of the complexes from the solvent is reversible by reheating the stock to regain solubility.

Separating the formation of metal-acid salt complexes from the synthesis of QDs allows optimization of its reaction parameters without the need to consider how it will affect the nucleation and growth of QDs. It also allows user-specified complex concentrations based on the needs of synthesis—for example, mid-growth addition of complexes prepared at higher concentrations leads to less increase in growth solution volume and consequently, less decrease in monomer and ligand concentrations in the reaction vessel. Furthermore, using stock precursor solutions enhances reproducibility among batches of QDs by uniformizing the precursor source while shortening the time and steps required to perform multiple syntheses.

The starting source of cadmium for making cadmium-acid salt complexes is usually a salt itself because free metal cadmium is highly toxic. Complex formation essentially involves an exchange of the Lewis base into acid ligands to be used for QD synthesis, hence the stability of the original salt would determine the rate and ease at which the new complexes form. Critical parameters in metal-acid salt complex formation include concentrations of starting chemicals, temperature as well as the rate of temperature change over time. The temperature ramping profile determines both the speed of pyrolysis of the original metal precursors and the concomitant complexing between the freed metal ions and the acid ligands. Precipitation of metal particulates occurs if the pyrolysis proceeds at a rate too fast for the acids to associate in time; in the case of cadmium salt making, the telling sign is the reaction solution turning intense yellow (similar to egg yolk), then brown and eventually, grey, indicative of large pieces of pure metal suspended in solution. Aside from too aggressive a temperature ramp rate, other factors enabling pure metal precipitation include weak ligands and ligand-to-metal ratios less than or close to the minimum stoichiometrically required for the complexes to use up all metal ions (2:1 for acid: metal for cadmium and zinc salts).

Even without concerns of their toxicity, free metal precipitates are expected to be more reactive compared to the metal-ligand complexes when introduced into QD synthesis and their concentrations should remain consistent from one preparation of stock solution to the next. In the case of making cadmium-phosphonate (Cd-OPA) in TOP, experiences cumulated over this project have suggested that even minor increase in temperatures and/or temperature ramping rate during salt formation is sufficient to increase the free: bound cadmium ratios of the prepared stock. It is indicated visually by a stronger yellow hue as well as lower viscosity, likely due to the relatively low concentration of cadmium phosphonate polymers (as described in section 2.4.2.2.2). These observations, once again, confirm the importance of preparing stock precursor solutions in a rigorous and consistent manner.

CdO has been chosen as the cadmium source for this purpose. While its exceptional stability cumulates to the need for more aggressive pyrolysis conditions (higher temperatures, longer reaction times and often, higher acid: metal ratios) compared to less stable sources (such as cadmium acetylacetonate, cadmium acetate and cadmium hydroxide), it also contributes to its availability at high purity (>99.99% trace metal basis), its low cost and good shelf life. Cadmium acetylacetonate ($Cd(acac)_2$) was previously used as cadmium source but suffered from batch to batch variations even at 98% purity level, likely due to its hydration levels not registering as trace metals that is the purity metric of most cadmium sources; a brownish-pink tint of varying intensity is often observed and is believed to be cadmium oxide. An alternative clean source that is easier to pyrolyze is cadmium hydroxide ($Cd(OH)_2$), also available at 99.99% purity (trace metal basis) but is much more costly.

As previously mentioned in sections 2.4.2.1 and 2.4.2.2, the choice of octylphosphonic acid originates from the consideration that it is already present as TOPO's known impurity as well as its high temperature oxidative product. Involvement of fewer

chemical species should render nucleation and growth of the QDs easier to control and reproduce.

One of the challenges in "coordinating chemistry" based QD synthesis is the lack of relatively inert liquid carriers for mid-synthesis precursor addition, unlike its "non-coordinating chemistry" based counterpart for which the alkene solvent (1-octadecene, ODE) is already a good carrier. TOP has been the choice carrier for most injections in "coordinating chemistry" based synthesis, whether at nucleation or during growth; however, as TOP is also the major ligand for Group VI, the volume of TOP injected also influences the kinetics of the chalcogens. Furthermore, when injection volumes become significant, impurities and especially acids in the TOP, if not removed, are added in significant amounts compared to the acids intentionally added, similar to the case described for TOPO (section 2.4.2.1)—and commercial TOP's maximum purity level is only 97% compared to TOPO's 99%.

In using TOP as the carrier for Cd-OPA precursors, therefore, one important goal is to minimize the volume of TOP needed, which also maximizes the concentration of the Cd-OPA complexes. A balance must nonetheless be achieved, for it is even more essential that the amount of phosphonic acids added is minimal, i.e. just sufficient for CdO pyrolysis—a goal that, in contrast, benefits from using *larger* volumes of TOP, a reducing agent for the CdO. Another consideration in developing the complex making protocol is the ease with which the stock solution can be handled; as the volume of TOP decreases, the stock solution turns increasingly viscous and unlike Cd-oleate in ODE solutions, temperatures of >110°C— impractical for synthesis use—are needed to mobilize these Cd-OPA complexes.

The following protocol has taken into account all of the mentioned considerations. It works as described only when purified TOP is used.

3.3.3.1 Making 0.5M Cd-OPA (1:1.25) in TOP: The Protocol

Cadmium oxide (CdO, >99.99% trace metal basis) is available from Sigma Aldrich (St Louis, MO) and used as purchased. Octylphosphonic acid (OPA, 98% acid basis) is available from PCI Synthesis (Newburyport, MA) and recrystallized once as described in Appendix 5.3.2. TOP (97%) is available from Strem Chemicals (Newburyport, MA) and purified as described in Appendix 5.3.5.

1. Strong, burst-like refluxes are expected to occur due to the relative viscous content in the reaction vessel during and after the formation of Cd-OPA complexes. For this reason, use a large round-bottom flask (250mL; 14/20 joint) and long distilling column (30cm, 14/20 joint) for the amount of chemicals to be described and they should be thoroughly cleaned. The temperature probe should have minimal contact with the acidic solution.

2. Weigh out 3.211g CdO (25.00mmol) and 6.069g OPA (31.25mmol) and transfer to flask. Then introduce 50mL of TOP, fresh from its glove box storage, and immediately pull vacuum on flask content.

3. Degas the flask content at room temperature until base pressure is reached. Then, over the course of ~10min, slowly ramp the degassing temperature towards 100°C—at this temperature range, the OPA should remain largely solid and the CdO, in its brown, powdered form. Wait until the temperature is stable at ~100°C, then begin ramping towards 125°C. The OPA should begin melting at ~110°C and bubbling that is indicative of CdO pyrolysis should commence at the same time. Degas for an additional 15minutes at 125°C. The reason for the brief hold at ~100°C is to avoid temperature overshooting, which is prone to occur when solids melt and cause excessive bubbling and refluxes, the latter often leading to a film of dried CdO / OPA / Cd-OPA stuck

on the glass walls of the flask, compromising the accuracy of the stock solution's concentration.

4. Backfill the flask with N_2. The next step is to ramp the temperature to 280°C for CdO pyrolysis and Cd-OPA complex formation. Once again, the ramp should be performed in steps to better control the temperature:

    a. Set temperature T to 215°C. Bubbling should steadily increase as the temperature rises. By ~180°C, white smoke (from released water vapor) is likely visible in the flask—a needle (30G) may be inserted to relieve this pressure, which also accelerates the rate of temperature increase.
    b. Allow the temperature to stabilize before continuing to ramp the set point of T towards 280°C, going in smaller increments as T approaches its target value.
    c. The 280°C hold should last for ~15minutes total. During that period, tap the reaction flask *very lightly* (do NOT shake) to bring CdO off the walls of the flask—the small bursts of reflux (from water vapor) from the tapping will help to bring the material down. Wait for the white smoke from these bursts to subside. Repeat if needed until all CdO is collected and reacted and the flask content is pure white from the Cd-OPA complexes. (If the flask is separated from its heating pad during the tapping, it is helpful to set the Variac temporarily to 0 to avoid excessive heating).

5. Begin cool down (to 4°C) by removing the heating pad from the flask. By 180°C, remove the 30G needle that has been used to relieve water pressure, if inserted. By ~100°C, a water bath can be used to speed up the cool-down, followed by an ice bath once the temperature falls below ~40°C. It is essential

that the flask content is cooled to well below room temperature before moving on to the next step—the low temperature is needed for the Cd-OPA complexes / polymers to precipitate and decrease the solution viscosity sufficiently for the vacuum pull, which, due to the residual water content of the solution, can otherwise lead to a very messy splashing of the flask content.

6. Degassing: while on vacuum, ramp the flask temperature slowly back to 100°C, waiting for bubbles to subside at every step (the majority of outgassing should occur between 20-45°C). At 100°C, degas for ~15minutes and the flask content should reach base vacuum pressure.

7. Cool the flask content back to 4°C with water and ice baths, as described in step 5. This time, the precipitation of Cd-OPA and lower viscosity of the solution is helpful for a clean and complete transfer into a N_2-backfilled flask, which can then be introduced into the glove box for storage. At this point, the stock solution should carry a light yellow tint and has a gel-like consistency. Unlike Cd-oleate in ODE solutions, Cd-OPA complexes do not settle efficiently in TOP at room temperature and a few vigorous shakes should be sufficient to homogenize the solution before use.

3.4 Overview of Synthesis, Overcoat & Flocculations of $CdTe_xSe_{1-x}$ QDs: Strategies, Challenges, and Occasionally, Solutions

This section will discuss the specific issues surrounding the ongoing optimization for each of the three major preparing steps for $CdTe_xSe_{1-x}$ QDs: synthesis, overcoat and

flocculation. Its intent is to highlight the lessons learned from past observations and justify the design of the protocols to be described next.

3.4.1 Refrain: On The Importance of Purified Chemicals and QD Population Uniformity

The synthesis protocol for $CdTe_xSe_{1-x}$ QDs have undergone several overhauls over the course of this project, most of which are associated with the switch from using as-purchased to purified starting chemicals of the same purity level. Because of the time, effort and cost involved for purification, purification of the chemicals was initially performed on a need-to basis and only TOPO and TOP were purified based on reports in literature. Over time, however, it becomes clear that every starting chemical contains impurities that modulate synthesis, with some being subtler in their effects. For example, hexadecylamine (98%)'s impurities have been found to encourage MSNC formation. Thus while purifications may seem tedious, they have proven to be worthy of the time and effort.

Another important lesson learned is more specific to the development of alloyed QDs: achieving a monodisperse, uniform QD population is a prerequisite for its proper characterization and use. Many QD characterization techniques, such as X-ray diffraction (XRD) for crystal structure or inductively coupled plasma spectroscopy (ICP-AES, ICP-MS etc.) for elemental analysis, are performed with the assumption that the sample population is single and uniform, thus the results are only as meaningful as to what extent this assumption holds (Figure 3.3). "Use" includes using the nanocrystals as crystalline templates for overcoating. The presence of MSNCs, for example, compromises any attempt to determine the appropriate amount of precursors to introduce, by being very difficult to detect, of vastly

different sizes compared to the major population and also by its being a secondary source of semiconductor monomers via Ostwald ripening (section 2.4.1.2).

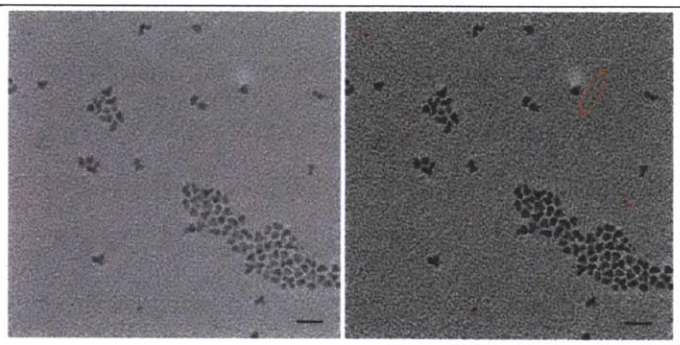

Figure 3.3: Compromised accuracy in the characterization of non-uniform QD samples. TEM shows that the mean diameter of the major QD population in this early sample is ~5.8nm. It also reveals the presence of extraneous populations (MSNCs) that are difficult o discern in the original image (left) but are more visible under enhanced contrast (right; some circled in red). The major QD population also suffers from poor morphology, varying in shape and showing signs of pod growth. XRD analysis of the same sample assumes sample uniformity and identifies the nanocrystals' mean diameter as 3.2nm. The diameter is clearly incorrect and likely influenced by the MSNCs seen in TEM. Similarly, elemental analysis can provide inaccurate results for non-uniform samples like this one, if the major and extraneous populations differ in composition. Scale bar = 20nm.

As seen in Figure 3.3, TEM is a highly efficient tool for gauging the uniformity and shape of QD products. TEM data has also, over the course of this project, aided in the understanding of how absorption profiles of (CdS@)$CdTe_xSe_{1-x}$ QDs are shaped by composition gradients, by identifying genuine synthesis problems (poor crystallinity, presence of MSNC and other extraneous QD populations etc.) that also modulate the features of the curves. Relevant data and discussion can be found in section 3.6.3.

3.4.2 On the Synthesis of $CdTe_xSe_{1-x}$ QDs: Strategies towards Creating Singular Emitter Populations with Predictable Composition and Fluorescence

A set of "perfect scenarios" has been defined for $CdTe_xSe_{1-x}$ synthesis. First of all, nucleation should produce a single population of nucleates of identical size and composition. This is ideally followed by nanocrystal growth that can overlook the kinetic difference between the chalcogen precursors and incorporate CdTe and CdSe at a rate reflective of the relative precursor concentrations in the growth solution, which encourages alloying over the formation of core-shell compositional structure and suppresses type II optical behavior. By the end of growth, near-exhaustion the tellurium and selenium precursors (i.e. high reaction yield) is desirable as it not only equates high reaction yield but renders the final QD compositions more predictable prior to synthesis, in a "what you add is what you get" manner.

The following strategies have therefore been implemented in the synthesis of $CdTe_xSe_{1-x}$ QDs:

1) Allow head start for Te entry, such that the nucleation "burst" creates all CdTe nucleates. Use two syringes for injection at nucleation, such that TOP-Te, in the first syringe with the Cd-OPA precursors, can be injected immediately before TOP-Se, which is loaded in the second syringe. The goal is to exhaust cadmium precursors to below C_N, the critical concentration for nucleation (section 2.4.1.1), with the formation of CdTe monomers only.

2) Increase the reactivity and reaction yield of chalcogens, particularly the selenium precursors (TOP-Se), for growth, by introducing diphenylphosphine (DPP) during and not before nucleation. As previously discussed (section 2.4.2.1), diphenylphosphine enhances the incorporation rates of chalcogens [53,179].

3) Encourage sterically-driven incorporation of chalcogens via introduction of squalene (98%, as purchased), also during and not before nucleation. Current

hypothesis is that squalene is less effective than TOP in breaking down the polymerized cadmium phosphonate (Cd-OPA) precursors (section 2.4.2.2.2), which will also become the dominant metal-ligand species on $CdTe_xSe_{1-x}$ QD surfaces. Physical diffusion barrier in the form of this coordination polymer should favor the entry of smaller-sized CdSe monomers compared to CdTe, which is energetically / kinetically favored, thus equalizing the incorporation rate between the two monomers. Squalene may also facilitate the formation of hydrogen chalcogenides (ex. H_2Se) (section 2.4.2.2.1). Squalene should also have a much lesser effect on the lability of Te and Se compared to TOP, which, if introduced in large volumes, can over-facilitate surface atom exchanges that widen the physical size and spectral distribution of the major population.

4) Sulfur precursors are added towards the end of growth, in significant excess, to encourage full incorporation of tellurium and selenium precursors into the QDs by shifting the reaction equilibrium between precursors and monomers towards the latter. Incorporation of sulfur into the nanocrystals also commences the overcoating process for the $CdTe_xSe_{1-x}$ emitters.

These goals are interrelated and may, at times, be at odds with one another. Introducing steric hindrance to enhance homogeneity of alloying may be counterproductive to improving reaction yield, for example. There are also potential tradeoffs, or restrictions in the extent of which these strategies can be performed; steps aimed to improve uniformity—such as offering a head start to tellurium—necessarily enhances the type II character in these QDs by ensuring the products are gradient alloys (more discussion in section 3.6.3).

3.4.3 On the Overcoating of $CdTe_xSe_{1-x}$ QDs: Removal of Magic-Sized Nanoclusters (MSNCs) as Pre-requisite, the Emitter/Overcoat Interface and 1-Pot vs. 2-Pot Processes

Achieving full stability in water has been the greatest obstacle in adopting NIR $CdTe_xSe_{1-x}$ QDs for biological applications. Bailey et al. reported entry of their gradient-alloyed QDs into biological buffers, but the nanocrystals formed a separate phase when mixed with water and were reported to precipitate over a period of two to three weeks [15]. Jiang et al. reported 12-14% CdS in composition, which translated to less than 1 monolayer of CdS overcoat (but should be less according to the dimensions of a wurtzite CdS unit cell), on their water-solubilized QDs [77]; a thin overcoat as such was not expected to offer full oxidation protection and stability data in the publication was restricted to 400 seconds in duration. Meanwhile, Pons et al. was able to overcoat their $CdTe_xSe_{1-x}$ QDs with three monolayers of $Cd_yZn_{1-y}S$ and demonstrate product stability over the course of four days [144], but the fluorescence of the emitters was mostly in the visible spectrum and while overcoating delivered the needed spectral "push" into the NIR, it did so with considerable spectral widening as well.

Early failures in overcoating $CdTe_xSe_{1-x}$ QDs for this project were plagued with inconsistencies that concealed the root cause of the problems and prevented proper optimization of the protocols. Overcoating late visible red (~680nm) fluorescent emitters, for example, led to the appearance of QDs spanning the entire visible spectrum, while the original emitters' spectral profile could red-shift, blue-shift or not shift at all. Almost in all cases, the major population lost its fluorescence and aggregated even under mild flocculation conditions, despite being introduced into overcoating at concentrations calculated from absorption cross-section values estimated based on Leatherdale et al [98], which had worked consistently for CdSe QDs, and the precursors and surface ligands were added accordingly and in excess

(see Appendix 5.5 for details of estimating the concentration of $CdTe_xSe_{1-x}$ QDs). TEM images revealed nanocrystals and their aggregates in a wide range of shapes and sizes when the emitter population had appeared uniform prior to overcoating, as previously seen in Figure 3.1 on early cell labeling experiments. Meanwhile, emitters that managed to retain their fluorescence after overcoating revealed only sub-monolayer changes in size (if any) under TEM.

It became evident over time that uncontrolled populations of MSNCs within the $CdTe_xSe_{1-x}$ major population instigated these inconsistencies in overcoating. These MSNCs had managed to remain after several rounds of hexanes / ethanol flocculation, the possible causes as discussed in section 2.4.1.5—in summary, size was no longer the only determinant in the flocculation rate of alloyed QDs. They had, moreover, often remained "invisible" to optical characterization and TEM for several reasons:

1. The telltale signs of MSNC formation in single-material CdTe or CdSe QD synthesis are sharp absorption peaks in the lower visible wavelengths. Compared to visible-fluorescent QD major populations, a NIR-fluorescent $CdTe_xSe_{1-x}$ major population, assuming similar 1st absorption peak absorptivity, is expected to absorb more strongly in the CdTe or CdSe MSNC-relevant range of wavelengths, thus possibly "burying" the MSNC absorption peaks co-existing in its absorption profile. Alloying also encourages the MSNCs from $CdTe_xSe_{1-x}$ synthesis to quickly lose their uniformity once they exit their caged structure configurations, leading to wide and flat signal distributions that are even more difficult to detect. Also, the lack of reference / "gold standard" absorption profiles for $CdTe_xSe_{1-x}$ QDs means there are no effective guidelines to identify extraneous absorption peaks prior to isolation of the major population, even if the MSNCs do present themselves as a "hump" in the profile. Figure 3.12 in section 3.6.2 compares the absorption profile of a sample

of QDs prior to and after MSNC cleanup by a multi-alcohol "high resolution" flocculation, thus identifying the MSNC peak retrospectively.

2. Fluorescence of the MSNCs is often poor compared to the major population before overcoating (also see Figure 3.12).

3. At the contrast setting optimal for imaging the $CdTe_xSe_{1-x}$ major population under TEM, CdSe-rich MSNCs are not only small but also likely in poor contrast due to their lower electron density. Flocculation also affects visualization of MSNCs in that the Cd-OPA polymer networks protecting the surface of the QD samples tend to leave electron dense "smudges" (as observed in sample PL656/29 in Figure 3.4) that further conceal the presence of MSNCs. Also, QDs often distribute on the sample grid in colonies, each composed of nanocrystals with similar physical attributes. Careful and extensive inspections are needed to "find" the MSNC colonies and accurately gauge the sample's uniformity.

MSNCs compete for the supply of precursors and monomers with the major QD emitter population, compromising the latter's ability to grow; furthermore, experiments performed for this project have suggested that MSNCs frequently have an upper hand in this competition for resources. These outcomes echo the discussion in section 2.4.1.4 about how, due to the dependence of surface energy to composition, MSNCs and their evolution via size focusing / Ostwald ripening can be detrimental to alloyed QD preparations. Depending on the MSNCs' concentration and sizes and the amount of precursor input, therefore, the major population could remain un-overcoated (no shift in the absorption peak), grow sluggishly (red-shift) or worse, dissolve to re-equilibrate free vs. bound monomer concentration in the reaction vessel (blue-shift). Very high concentrations of precursors lead to new

nucleation events (often observable as blue fluorescence from CdS nucleates) that introduce further non-uniformity to the major QD population.

Solving the problem of MSNCs required revisiting the protocols of emitter synthesis and flocculation to eliminate their sources, even if the major $CdTe_xSe_{1-x}$ population often appeared robust spectrally prior to overcoating. Modifications to synthesis aimed to improve reaction yield in order to keep the precursor concentration low and suppress MSNC nucleation while not evoking Ostwald ripening. A rigorous, highly-resolved multi-alcohol flocculation recipe (presented in section 3.5.3.2) for ridding the major $CdTe_xSe_{1-x}$ population from MSNCs was developed, although low concentrations of extraneous QDs usually remained. The flocculations were also time-consuming to perform and required "tweaking" based on the condition of synthesis to achieve the needed cleanliness without causing aggregation of the nanocrystals.

The switch from as-purchased to recrystallized 98% hexadecylamine (HDA) finally made overcoating $CdTe_xSe_{1-x}$ QDs a practical as well as a manageable, optimizable process. Afterwards, the use of multiple alcohols for flocculation was no longer necessary, with less MSNCs forming during synthesis and also being sufficiently distinct from the major population in size and shape that they are separable with "standard" 1-alcohol flocculations (protocol in section 3.5.3.1). HDA recrystallization has likely removed octadecylamine (ODA) as impurities. Syntheses using ODA had previously created a more uniform major population of QDs but also large concentrations of MSNCs, presumably due to the bulkier ODA slowing down growth kinetics; the MSNCS were also more difficult to extract, as were the leftover cadmium-phosphonate and amines from synthesis that precipitated as white salt during flocculation and in which MSNC fluorescence was frequently observed. The observed relationship between amine chain length and MSNC retention has led to questions of whether the cadmium-phosphonates on the nanocrystal surface, which

serves important protective purposes especially for tellurium-containing QDs with weak phosphine-tellurium surface bonds, not only polymerize but also coordinate with long chain amines given the anhydrous synthesis environment (section 2.4.2.2.2). It also generates the question whether the very bulky polymer complex that forms can harbor residual cadmium precursors / MSNCs and introduce them into subsequent steps of QD preparation, such as overcoating.

A general strategy for overcoating $CdTe_xSe_{1-x}$ QDs has been defined in this project and much progress has been made on its implementation. Prevalent 2-pot overcoating schemes of recent years—either using highly reactive precursors / very low temperatures (ex. dimethyl cadmium, bis(trimethylsilyl) sulfide / ~130°C [72]) or moderately reactive precursors / moderately high temperature (ex. SILAR; cadmium stearate, bis(trimethylsilyl) sulfide / 240°C [100])—have not performed well for $CdTe_xSe_{1-x}$ emitters, which do not tolerate well the long duration (>=2hrs) needed in both cases. When these schemes were tested, spectral widening was common, with a fluorescence "tail" developing on either side of the peak or both before overcoating began; successful suppression of the widening process, via introducing Cd-OPA precursors early and before the QDs were heated, usually led to insufficient or lack of overcoating.

The small compositional heterogeneity among the $CdTe_xSe_{1-x}$ population may be the cause of the defocusing spectral profiles, related to the alloyed QDs' compromised ability to size focus in that compositional effects on surface energies could encourage unwanted surface atom exchanges among the emitter QDs. $CdTe_xSe_{1-x}$'s relative lack of tolerance to prolonged heating may also share the same root cause / mechanism that underlies the known sensitivity of quasi-type II QDs' fluorescence to sub-monolayer shell thickening [38], such as, as previously discussed, the input heat driving a local re-ordering of atoms that modulates the compositional gradient. To address this possibility, durations of the high temperature phase in synthesis and

overcoating, including the rates of temperature ramping and cooling, have all been regulated to ensure consistency.

The inhibitory role of Cd-OPA precursors / coordination polymers is also worth attention. While the strong cadmium-phosphonate bonds on QD surfaces should render subsequent surface processes more difficult compared to non-phosphonate linkages, that they could bind tight enough as coordination polymers to "block" the surface and make it completely unworkable in subsequent steps had only been described in recent years, particularly during polymer cap exchange or encapsulation for water solubilization of the QDs [105,135,177]. It is possible that the use of higher purity starting chemicals and additional purifications as described in Appendix 5.3 have removed impurities that can potentially limit the size of the phosphonate polymer; phosphinic acid impurities in TOPO, for example, favors a 1D, straight-chain configuration rather than the bulkier 2D polymer sheet of phosphonic acids when coordinated with cadmium (section 2.4.2.2.2). A more in depth discussion on the cadmium phosphonate polymer, and how flocculation can modulate its quantity and size, can be found in the upcoming section 3.4.4.

Given the above considerations, overcoating of $CdTe_xSe_{1-x}$ emitter QDs now begins as a 1-pot approach, in which CdS incorporation follows immediately after emitter synthesis as an extension of growth. The temperature remains close to syntheses' and the time needed to overcoat shortens significantly as a result, due to fast kinetics at high temperature and also the elimination of steps required to degas the starting chemicals and the QD carrier when 2-pot approaches are implemented. 1-pot recipes also need not re-define a starting chemistry for overcoating; given the less certain concentrations of $CdTe_xSe_{1-x}$ emitter QDs (compared to single semiconductor QDs; see Appendix 5.5) and the need for higher temperatures, the chemistry at the end of growth should present the optimal condition for maintaining the equilibrium between precursors, monomers and QDs and stability of the latter. Meanwhile, the

major disadvantage of 1-pot approach is the inability to clean up or characterize the $CdTe_xSe_{1-x}$ emitter QDs prior to overcoating, which makes it more difficult to optimize or troubleshoot the process.

Hence, the recipes in focus in the upcoming protocol section will be for the synthesis of $CdS@CdTe_xSe_{1-x}$ QDs, with "CdS@" designating the incorporation of CdS on the emitters as the overcoating material. Optimal conditions of 1-pot overcoating schemes have, as expected, exhibited strong dependence on the preceding nucleation and growth steps that dictate the concentration and size of QDs. Hence, the optimal timing and quantity of precursor supply is expected to differ according to the target fluorescent wavelengths. Compositional analysis has confirmed the presence of sulfur and the nanocrystals are morphologically robust and highly uniform. However, they have yet to achieve consistent stability in water—while air stability has ranged from acceptable to good, stability in water has been limited and variant among the few tested samples (see section 3.7). This is likely due to an inadequate amount of CdS being incorporated, and/or the difficulty in creating a steep CdSe-to-CdS gradient that ensures complete sulfurization of the nanocrystal surface.

Controlling the $CdTe_xSe_{1-x}$/CdS composition gradient is the main challenge of 1-pot $CdS@CdTe_xSe_{1-x}$ synthesis as the chemical "history" in the growth solution prevents independent optimization of the CdS overcoating process. The emitter/overcoat interface is ideally infinitely sharp to completely free the surface of the faster and less stable emitter material (CdTe and CdSe) at termination; however, incorporation of at least a small amount of sulfur prior to Te and Se precursor depletion is expected due to the steric hindrance from the ligand condition intended for growth—which, the more it equalizes the incorporation rate of Te and Se, the more it is likely to counter the kinetic preference of Se over S. Thus the initial shift from kinetically to sterically controlled incorporation between nucleation and growth is preferably reversed

when overcoating begins. However, if the chemistry is to be limited to the set of chemicals used and purified for nucleation and growth, which has been chosen to ensure reproducibility, this reversal is more difficult to achieve as only the sulfur precursors and Cd-OPA are easily modifiable chemical variables in 1-pot overcoating.

Three types of sulfur precursors have been tested for this project: TOP-S, TBP-S and ODE-S. The relatively stable TOP-S and TBP-S ligand complexes have traditionally been considered ineffective precursors. However, these 1-pot processes use high overcoating temperatures and nucleation is not required (and best avoided); phosphine-chalcogenide precursors can also be made at high concentrations (2.24M/4.0M at saturation for TOP/TBP) that minimize dilution of the growth solution. Disparity between using TOP-chalcogenides and their TBP equivalents most likely lies in their steric differences; published enthalpies of chalcogen atom transfer have indicated that while the phosphorus-chalcogen bond strength is proportional to the alkyl chain length, the difference is small compared to a change in the hydrocarbon structure (linear vs. branched) or the chalcogen atom (S vs. Se vs. Te) [32]. Also noteworthy is TBP's relatively low boiling point, at 240°C (~260°C under elevated flask pressure); this poses an opportunity to "boil off" the ligand but poses a safety risk for high temperature injections.

Meanwhile, ODE-S prepared as described in section 3.3.2 is estimated to be <0.1M. And while ODE-S has created the most air-stable overcoated sample in this study, its chemistry remains obscure, as does the identity of sulfur's protective ligands in synthetic schemes without phosphines (as in SILAR). Coordination between sulfur and ODE to form polysulfide chains (section 2.4.2.2.1) is likely; a similar solution/suspension of red octatomic sulfur (S_8) has failed to form with other high temperature alkene such as squalene. Elucidating the coordination chemistry of ODE-S's sulfur on the QD surfaces is important for gauging the QD products' stability at application stage. In particular, if the coordination is the polysulfide chain as

described, then an environment that can effectively reduce disulfide bridges will, over time, destabilize the nanocrystals.

In 1-pot processes, it is difficult to supplement the weaker ligands, TOPO and HDA, to balance the phosphonic acids added along with the cadmium as precursors during growth and overcoat. TOPO facilitates chalcogen reaction rates and yields and also acts a Group II stabilizing ligand that competes with phosphonic acids at high temperature [140]; its higher polarity should also help suppress the size of the Cd-OPA polymer network on the surface of the nanocrystals, thus relieving the steric hindrance met by CdSe and CdS monomers. Any solvent chosen as carrier during overcoating must be close to inert due to the high temperature conditions and the presence of oxidation prone $CdTe_xSe_{1-x}$ emitters; alkanes and alkenes are nonetheless poor solvents for both TOPO and HDA. Current schemes therefore drive the overcoating process by providing the system with significant excess of sulfur precursors; as Cd-OPA is continuously supplied for overcoat, complete reversal of steric hindrance is not expected and the CdSe/CdS interface likely retains some alloyed character, which increases the probability that emitter materials reside on the surface of the final nanocrystals and compromise their stability.

Nonetheless, the 1-pot protocols described in this thesis should provide solid groundwork for future improvements. In addition to successful inclusion of sulfur, robust morphology and uniformity, their QD products have demonstrated efficacy for water solubilization, with near unity reaction yield and negligible loss to aggregation. Most important of all, preliminary data has suggested that with the inclusion of sulfur, the $CdTe_xSe_{1-x}$ emitters—now CdS@ $CdTe_xSe_{1-x}$ QDs—have gained the stability that they previously lacked to undergo a second overcoating procedure, the recipe of which can then be optimized specifically for overcoating. Aside from ensuring complete protection of the emitter, this separate overcoating procedure can also introduce ZnS that offers stronger carrier confinement than CdS.

Experimental efforts on this front have been performed using all purified chemicals as well, which ensure reproducibility and are also less forgiving to work with; thus this second overcoating procedure has remained a work in progress.

3.4.4 On Flocculation: Sizing the Cadmium Phosphonate Coordination Polymers as a Protective Ligand and Surface Barrier

As the process that separates QDs from their growth solution (both synthesis and overcoat), flocculation is ubiquitous in QD protocols but often described with few details. While publications focusing on size- and shape- selections have investigated the effects of flocculations in more depth (ex. [113]), specifics of the process—how much solvent and anti-solvent to add, for example—are rarely provided.

Yet, at the same time, most researchers experienced with the handling of QDs are aware that the manner by which flocculation is performed dictates the health of the QD population and its quantum yield (QY). Flocculation protocols are considered too "aggressive" not only when they remove too much of the QDs' protective surface ligands and cause them to be no longer suspendible in any solvent, but also when they instigate a major drop in QY; yet there are few guidelines on whether a gentle flocculation is actually adequate for its intended purpose, i.e. if it provides "workable" QDs that are sufficiently free of residual precursors, ligands and extraneous populations (MSNCs) from synthesis to proceed to the next step, and that behave predictably and consistently once they are there.

Reported QY values are therefore meaningful only if the QDs emerging from the specific cleanup condition are actually usable. For $CdTe_xSe_{1-x}$ QDs, performing flocculations has required the same rigor as needed for synthesis. In addition to removing MSNCs, flocculation has determined how "friendly" the QDs are to the

next step, be it overcoating or water solubilization, presumably by controlling the amount of strongly-bound cadmium-phosphonate (Cd-OPA) polymer remaining on the QD surfaces. This polymer, as previously discussed, may become not only an unaccounted source of cadmium but also MSNCs as well.

The number of flocculations performed has been found to be less consequential than the choice and volume of solvent versus non-solvent. In particular, non-polar hexanes in insufficient volumes have rendered the polar Cd-OPA polymer network increasingly difficult to remove with repeated use, presumably by deviating enough from a theta solvent to collapse the polymer on the nanocrystals (section 2.4.1.3). The hexanes in each round also carry increasingly lower concentrations of residual and relatively polar synthesis chemicals including amines and TOPO. The outcome is high QY, robust long-term storage ability but poor workability of the nanocrystals in subsequent steps.

Toluene is more effective in dissolving the coordination polymer and easing their removal from the surface of the nanocrystals, at the cost of QY and storage ability. It is more polar than hexanes, with Snyder polarity index $P' = 2.4$ compared to 0.1 of the latter [19,167,175] (exact values of polarity may differ slightly between sources—based on the methods used to determine the values—but the relative differences are similar).

Earlier in this project, chloroform (P'=4.1) was observed to be capable of suspending un-overcoated, flocculated CdTe-containing QDs and maintaining their QY for hours. Despite being cited as a good solvent early in the development of colloidal synthesis [126], suspension in chloroform has been known to cause speedy fluorescence loss, followed by aggregation. This unexpected display of robustness in early $CdTe_xSe_{1-x}$ QDs was immediately followed by a challenge when attempts were made to water solubilize them via polymer encapsulation (section 3.7). Adsorption of the

amphiphilic polymer was so inefficient that the QDs remained completely soluble in hexanes after the process and with little loss of QY. The extent of water solubilization, if any, was also inconsistent, until a rigorous protocol was used for flocculation.

The purity of starting chemicals from synthesis further modulated the outcome of flocculation. The most chloroform-compatible QDs were synthesized after TOP and TOPO purifications, which likely encouraged more extensive polymerization of the Cd-OPA (section 2.4.2.2.2). Over time, it became clear that amphiphilic polymer encapsulation could only work efficiently when the early $CdTe_xSe_{1-x}$ QDs were more aggressively cleaned up and lost their ability to sustain themselves in chloroform; in achieving the latter, they lost their ability to sustain in air as well, given their lack of an overcoat.

Compatibility of gently flocculated $CdTe_xSe_{1-x}$ QDs in chloroform, coupled with observations that its survival in chloroform correlates with the amount of Cd-OPA salts precipitated at flocculation, suggested the Cd-OPA bonds are not only strong but also likely dominant in the form of polymers on the nanocrystals, which then render the surface more polar and well protected compared to the triplet of octyl chains supplied by TOP ligands or a single one by monomeric phosphonates or amines. Chloroform is a good QD solvent when the surface of the QDs is dominated with TOPO ligands [93,126], which are also more polar. The strongly coordinating polymer may be key to suppressing cadmium sublimation in CdTe as part of its oxidation process, which would have led to unchecked loss of CdTe past the surface into the inner structure of the nanocrystals [50]; supporting this reasoning is the observation that while these $CdTe_xSe_{1-x}$ QDs loses fluorescence in air, the process can be very slow prior to flocculation—sometimes taking days. In such cases, cadmium phosphonate polymers on CdTe-containing QDs may fulfill a similar protective role as CdO in CdSe QDs, the formation of which is ligand-independent and is resistant to

non-solvent breakdown—and Te-containing QDs' sensitivity to flocculation reflects their reliance on the cadmium phosphonate polymer to protect them against environmental assault. The corollary would be that CdSe QDs are less sensitive (but not insensitive) to flocculation conditions, which would explain why flocculation protocols in literature (mostly for CdSe QDs) have traditionally been described in a less rigorous manner compared to the needs of this project.

One postulation from size focusing of single material QDs is that the highest QY and narrowest size distribution is achieved when equilibrium between the surface monomer and QDs minimizes the rate of surface atom exchange, the latter allowing time for optimal surface reconstruction [153]. Dependence on the external polymer for oxidation protection would imply a significant role played by the concomitant state of surface ligands during the surface optimization of $CdTe_xSe_{1-x}$ QDs. As overcoating must remove the ligand "cap" to deposit inorganic protective material, the key to its success may lie in minimizing the lag time between ligand disruption and new material deposition. This would explain why long overcoating processes are often problematic for the alloyed QDs—the transition between the two steps may not be seamless enough, allowing time for significant surface atom exchanges between the emitters after ligand disruption but before sulfide incorporation.

A proper flocculation for CdTe-containing QDs should, therefore, achieve a balance between retaining the protective properties of the phosphonate polymer and restricting its size to warrant surface accessibility. Specifically, an optimized flocculation avoids dissociating the bonds between the nanocrystals and the ligands, but trims down the bulk of the phosphonate polymer by dissolving it and breaking it down with a proper mixture of solvent(s) and non-solvent(s). Longer chain alcohols have proved more effective for this purpose, likely due to steric hindrance that prevents them from diffusing deep enough to reach the crystal-ligand interface. Ethanol (P'=4.3) has been the "standard" non-solvent for CdTe and phosphonate-

containing QDs after methanol (P'=5.1), the classic non-solvent for CdSe QDs, was deemed too aggressive; this reasoning alone, however, is likely too simplistic in explaining why ethanol has been a better non-solvent choice. The non-solvent's effectiveness in breaking down the coordination polymer goes hand in hand with the solvent's ability to spread out the polymer, rendering the QDs well suspended as single nanocrystals but also more prone to attack by other agents. Methanol's immiscibility with the common solvent hexanes has traditionally been solved by the addition of butanol, which exerts its own solvent / non-solvent effect. In all cases, for a flocculation to perform properly, the solvent and non-solvent should be considered as one system to be optimized; they must be fully miscible and the ideal ratio of the two may require adjustments upon gradual removal of the growth solution from synthesis (ex. dissolved TOPO), which acts as a co-solvent in the initial round of flocculation. Ultimately, a robust flocculation protocol is well-paced in its cleanup and ensures good resolution in each step, the latter also critical to removing extraneous QD populations such as the MSNCs.

3.5 Protocols for Synthesis, Overcoating & Flocculation of (CdS@)$CdTe_xSe_{1-x}$ QDs

There's no "unifying" protocol that broadly describes the synthesis and overcoating of (CdS@)$CdTe_xSe_{1-x}$ QDs, with NIR fluorescence that is sufficiently narrow for the original motivation of this project, i.e. to create a series of imaging probes suitable for multi-channel NIR imaging. The difference in kinetics between the alloying Te and Se precursors affects concentrations of QDs that form in the solution, which in turn determines the quantity of precursors needed for the process. The rate of precursor depletion is further modulated by the size evolution of the nanocrystals over time. As Ostwald ripening must be avoided but too high concentrations of precursors lead

to extraneous nucleation, the appropriate concentration "windows" at any time point during synthesis and overcoating are very narrow. There is also a practical limit on how much the Group II Cd-OPA precursors can be supplied, as the major solvent and weak/facilitating ligands, TOPO and hexadecylamine (HDA), are both difficult to supplement given their solid forms at room temperature.

Consider this scenario: two populations of 5nm diameter QDs, with 1st absorption peak at ~700 and ~725nm, are needed. Consulting the plot of estimated 1st absorption peak for 5nm $CdTe_xSe_{1-x}$ QDs determined based on bulk optical bowing factor (Figure 2.2), the goal translates to making QDs of compositions $CdTe_{0.9}Se_{0.1}$ (for 700nm) and $CdTe_{0.6}Se_{0.4}$ (for 725nm), respectively. The chemist proceeds to inject 0.9mmol TOP-Te+0.1mmol TOP-Se and 0.6mmol TOP-Te+0.4mmol TOP-Se into a two reaction vessels, each with the same amounts of ligands, solvents and group II precursors.

The following is likely to occur: the first synthesis, for $CdTe_{0.9}Se_{0.1}$, forms nucleates at a higher concentration due to the fast kinetics of tellurium precursors, and the high surface area / volume ratio of small nanocrystals means they will sooner exhaust the precursors in the reaction vessel, and at smaller sizes than the synthesis for $CdTe_{0.6}Se_{0.4}$. Supplying Cd-OPA in a steady pace helps to prevent Ostwald ripening (which would then require focusing to re-establish a narrow distribution), but only to a certain extent because the phosphonate/amine ratio eventually becomes too high for growth to proceed; supplying chalcogen precursors perturbs the smooth composition gradient and makes it even less predictable. It is hence a challenge to match the two populations in size, and the composition of each is also likely deviate from the target and to a different extent, with the higher [Se] sample potentially being more problematic; composition gradient, a function of size and composition, deviates then. The overall outcome is that the absorption and fluorescence wavelengths of the two populations can be far from predicted.

Optimized synthesis protocol should minimize the difference between prediction and outcome. While there is no "unifying protocol", the series of protocols at their current state, compiled based on the properties and quality of products they yield, share the majority of their attributes and are sensitive to wavelength modulating parameters such as %Te in Group VI precursors, temperatures and amine/acid ratio. While this statement is intuitively obvious, it has not been necessary true. Early in the project, overly high ligand concentrations prevented wavelength extension into the NIR, presumably due to a very sluggish growth that is kinetically sufficient to incorporate only tellurium into the major emitter population; selenium was left out and eventually formed MSNCs. The first step towards optimization is therefore determining the range of precursor concentrations that "sensitize" the protocol to wavelength modulating parameters. Using pure starting chemicals is essential for clarifying these trends.

3.5.1 Protocol for the Synthesis of $CdTe_xSe_{1-x}$: Without Overcoating

Synthesis of $CdTe_xSe_{1-x}$ without overcoating allows for relatively large initial precursor–ligand concentrations—which translate to higher nucleate and QD concentrations—within the Cd-OPA maximum concentration limit that still allows for efficient growth, as there is no need to "make room" for CdS incorporation. The protocols presented this subsection are therefore suitable only for the preparation of emitters for separate overcoating procedures and with proper flocculation in between.

In order to reproduce the protocols to be described below, which are only minutes-long in duration and hence allow little time for temperature stabilization, the temperature controller must be well calibrated and uses a temperature ramping rate that minimizes temperature overshooting. These requirements can be verified

beforehand by checking the temperature profile upon heating a high temperature solvent such as squalene. The stir rate should also be controlled as it affects heat distribution and thermocouple reading. The growth temperature is in particular sensitive to instrumentation, being the collective outcome of nucleation temperature, the starting growth solution and injection volumes that determine the temperature drop after injection, and the extent of rebound in temperature immediately after injection, which is the combined effect of the temperature of the heat pad (determined during ramping to nucleation temperature) and the temperature controller's feedback response to the sudden plummet in its reading.

The following tools and setups have therefore been used for syntheses:

- Glassware: 4-neck round bottom flask, 50mL. 14/20 joint.
- Temperature control: REX-D100 Controller (RKC Instrument, South Bend, Indiana) or equivalent that ramps at a consistent rate of $(T_2-T_1)/10$ min (REX-D100 ramps at this rate in its default factory setting). Type K thermocouple (Omega Engineering, Stamford, CT). Variable autotransformer ("Variac"; Model 3PN1010, Staco Products, Dayton, OH) set at 140V maximum.
- Stirrer (Model PC-420D, Corning, Lowell, MA): set at a stir rate of ~800rpm. Use only egg-shaped magnetic stir bars and never those cleaned in acid baths; the stir bars should be dedicated for syntheses and washed with alcohols and hexanes (no water) between runs.
- Stopwatch with seconds measurement.
- Heat gun with fan-only mode, to be used for reducing the cooling time (usually by ~50%).

There is no time for introducing materials into the glove box after degassing begins, thus all needles, syringes and vials should already be inside the N_2 environment before starting synthesis. The volumes needed for all precursors to be injected

should be calculated, and scaled up accordingly to account for the un-injectable "dead volume" inside the needle, which is ~ 0.15mL (an excess of ~0.3mL is recommended to ensure sufficient volumes can be drawn for injection). The schlenk line should be at steady base pressure.

TOPO, TOP, hexadecylamine (HDA) and octylphosphonic acids (OPA) are purified as described in Appendix 5.3. Squalene 98%, diphenylphosphine (DPP) 98% and anhydrous hexanes (95%) are used as purchased, from Sigma-Aldrich (St Louis, MO). Precursors stock solutions including Cd-OPA (=0.5M Cd-OPA in TOP), TOP-Te, TOP-Se are prepared according to the instructions in section 3.3. The protocol below describes the general steps; exact quantities of chemicals, temperatures, time points and injection rates for different wavelengths of $CdTe_xSe_{1-x}$ QDs will be listed in Table 2. Samples are labeled ***PL X/Y***, with X being the fluorescence peak wavelength and Y, the FWHM of the fluorescence peak in nm after flocculation.

1. Measure the appropriate amounts of recrystallized TOPO and HDA and place in a 50mL 4-neck flask. Pull vacuum and degas flask at room temperature to make sure base pressure can be reached—this ensures the flask is completely sealed.

2. With Variac setting at ~60-70% full power, ramp the temperature to ~60°C (TOPO melts), then ~105°C (HDA melts) and finally the degassing temperature T_{degas}, which is 125°C for this protocol series. Make sure thermocouple tip is steadily positioned well above the stir bar but inside the flask content.

3. Degas TOPO and HDA for 10 minutes. At the end of 10 minutes, the mixture should be at base pressure; if not, the timing should be consistent between runs to avoid inconsistent evaporative loss of amines. Prepare TOP+DPP for

injection (use 21G or smaller needle) in the glove box. Retrieve syringe from glove box and inject.

4. Degas flask content for an extra 5 minutes. The pressure should fall back to base pressure within this time frame.

5. Switch to N_2. Turn Variac to full power (100%) and change temperature set point to nucleation temperature T_{Nuc}+1.0°C to begin ramping, which generally takes between 17-20minutes. Do not use glass wool to speed up the process as it may create temperature control problems later. The longer ramp time is due to the very high nucleation temperature, which is also approaching the boiling point for HDA. During the temperature ramping period, prepare syringes for injection during both nucleation and growth in the glove box.

6. The following set of syringes is to be prepared:
    A. Cd-OPA+TOP-Te+Squalene for NUCLEATION; 5-6mL syringe / 16G needle.
    B. TOP-Se for NUCLEATION (except for CdTe only QDs); 1mL syringe / 21G needle. Do not use 16G needle for 1mL (or any non-Luer locked) syringe as the pressure inside the flask will dislodge the two.
    C. Cd-OPA for GROWTH; 1mL syringe / 21G needle.

Shake all precursor stock solutions, including the TOP-chalcogens and in particular, the 0.5M Cd-OPA in TOP solution immediately before drawing out volumes. When mixing *Syringe A*, add Cd-OPA last, then mix the content by drawing and injecting the solution in and out of the preparation vial several times before loading. Keep the syringes in the glove box until it is time to inject.

7. Once the flask content stabilizes at T_{Nuc}+1.0°C (do not wait as amine content may decrease via evaporation), retrieve the syringes from glove box and unlock the needle cap for all of them. Immediately proceed to the following step, which must be performed at quick succession.

8. NUCLEATION **start timer, t_{Nuc} = 0sec**: Lower temperature set point to $T_{Gro\text{-}set}$ = 315°C, insert both *Syringe A* and *Syringe B* needles through separate septa. When temperature drops 1.0°C to nucleation temperature, inject A, then B immediately. Note the temperature drop for future reference. Do not remove the heat pad.

9. GROWTH: begin *Syringe C* Cd-OPA injection to supplement Group II precursors for growth at designated time $t_{Cd\text{-}Gro}$ (=15sec for this protocol series), at the specified injection rate(s) $r_{Cd\text{-}Gro}$; in some cases, $r_{Cd\text{-}Gro}$ increases over time, similar to during SILAR when more precursors are introduced for consecutive semiconductor monolayer growth. Follow the rate as closely and as evenly as possible; for example, if 0.9mL Cd-OPA is to be injected over the course of 1 minute, with 1/3=0.3mL in the first 30 sec and 2/3=0.6mL in the second 30 sec, then during the first 30sec the injection rate can be 0.1mL / 10 sec, and during the second 30sec, 0.2mL / 10 sec. Note the temperature during growth, T_{Gro}, and record for future references; with appropriate temperature controller settings, nucleation temperature ~350-360°C and injection of ~3.0-3.5mL total, the temperature should bounce back to the set point temperature (315°C) almost immediately with minimal heat input and without overshooting. It is likely, however, that T_{Gro} will deviate several degrees from 315°C.

10. At the end of growth (time t_{Gro}, = 90sec for this protocol series), turn Variac to 0% power, remove heat pad and use the fan-only mode of the heat gun to speed up the cool rate by ~ 2x. Flask content should cool to 80°C in ~5-6min.

Samples can be taken at this point for absorption and fluorescence measurement.

11. Inject 12mL anhydrous hexanes retrieved from the glove box, transfer solution into N2-filled septum vial and transfer into glove box for storage.

Table 2: Specifications of synthesis conditions for $CdTe_xSe_{1-x}$ QDs.

	CdTe *Em: 668/31	**CdTeSe** **Em: 737/37	**CdTeSe** ***Em: 764/47
TOPO *Starting chemical*	4.640 g (12.000 mmol)	4.640 g (12.000 mmol)	4.640 g (12.000 mmol)
Hexadecylamine *Starting chemical*	1.449 g (6.000 mmol)	1.449 g (6.000 mmol)	1.449 g (6.000 mmol)
TOP *Inject after 10min degas*	2.679 mL (6.000 mmol)	2.679 mL (6.000 mmol)	2.679 mL (6.000 mmol)
DPP *Inject after 10min degas*	0.0209 mL (0.120 mmol)	0.0261 mL (0.150 mmol)	0.0209 mL (0.120 mmol)
Squalene *Nucleation: Syringe A*	2.900 mL	2.955 mL	2.955 mL
TOP-Te 1.0M *Nucleation: Syringe A*	0.100 mL (0.100 mmol)	0.045 mL (0.045 mmol) (Te 30%; Se 70%)	0.045 mL (0.045 mmol) (Te 30%; Se 70%)
0.5M Cd-OPA in TOP *Nucleation: Syringe A*	0.300 mL (0.150 mmol Cd)	0.300 mL (0.150 mmol Cd)	0.300 mL (0.150 mmol Cd)
TOP-Se 1.2M *Nucleation: Syringe B*	N/A	0.0875 mL (0.105 mmol) (Te:Se 3:7)	0.0875 mL (0.105 mmol) (Te:Se 3:7)
0.5M Cd-OPA in TOP *Growth: Syringe C*	0.700 mL (0.350 mmol Cd)	0.900 mL (0.450 mmol Cd)	1.200 mL (0.600 mmol Cd)
T_{Nuc} *Nucleation Temp.*	350°C (T ↓ to 302.5°C after	355°C (T ↓ to 303°C after	357°C (T ↓ to 305.5°C after

	Syringe A injection)	Syringe A+B injection)	Syringe A+B injection)
t_{Nuc} *Time of Nucleation (always 0: begin timing)*	0 sec	0 sec	0 sec
$T_{Gro-set}$ *Growth Temp.: Set point*	315°C	315°C	315°C
t_{Cd-Gro} *Time, start Growth Cd-OPA (Syringe C) injection*	15sec	15sec	15sec
r_{Cd-Gro} *Injection Rate of Growth Cd-OPA (Syringe C)*	0.7mL/60sec for t=15-75sec Done at 75sec	0.3mL/30sec for t=15-45sec 0.6mL/30sec for t=45-75sec Done at 75sec	0.3mL/30sec for t=15-45sec 0.6mL/30sec for t=45-75sec Done at 75sec
t_{Gro} *Total Growth time*	90sec	90sec	90sec
T_{Gro} *Growth Temp. (Mean)*	308°C	311°C	318°C

TEM and spectral data of these QDs will be shown in section 3.6.1.1.

3.5.2 Protocol for the Synthesis of CdS@$CdTe_xSe_{1-x}$: With Sulfur Incorporation / Overcoating

1-pot approaches that combine synthesis and overcoating require lower starting precursor-ligand concentrations to create less nucleates, so that enough Cd-OPA can be supplemented for CdS incorporation without stalling the growth process. Sulfur input begins the overcoating process of the $CdTe_xSe_{1-x}$ emitter QDs and helps to

exhaust the supplied tellurium and selenium precursors such that the QD composition matches the chalcogenide precursor input's.

These protocols have created QDs that are air stable for days to weeks; however, the two samples that underwent water solubilization via encapsulation by poly(maleic anhydride alt-1-tetradecene) (see section 3.7 for details) did not exhibit sufficient stability for biological applications, have suffered an average loss of 60% of their QY after 1 day in water. As there was no signs of aggregation or precipitation of these water-solubilized QDs, it is likely that the overcoating is not thick enough for complete protection against oxidation. Out of the QDs synthesized and overcoated using the following protocols, the sample PL 786/62 was most likely to have a complete overcoat given its distinctly larger size after overcoating under TEM and its air stability upward of 14 days; this sample, however, did not undergo water solubilization.

The tools and preparation required are the same as for the protocols for synthesis without overcoating (section 3.5.1). Degassing steps are also identical, with the exception of DPP being introduced with Nucleation *Syringe A*; as expected, the most significant difference occurs during and after growth, with further temperature modulations and multiple injections of Cd-OPA and sulfur precursors. The full, generalized protocol is once again described first, followed by a table with exact quantities of chemicals, time and temperature for different wavelengths (Table 3). The protocols for two more samples, PL672/35 and PL770/61, are presented in their original worksheet format in Appendix 5.4.

1. Measure the appropriate amounts of recrystallized TOPO and HDA and place in a 50mL 4-neck flask. Pull vacuum and degas flask at room temperature to make sure base pressure can be reached—this ensures the flask is completely sealed.

2. With Variac setting at ~60-70% full power, ramp the temperature to ~60°C (TOPO melts), then ~105°C (HDA melts) and finally the degassing temperature T_{degas}, which is 125°C for this protocol series. Make sure thermocouple tip is steadily positioned, well above the stir bar but inside the flask content.

3. Degas TOPO and HDA for 10 minutes. At the end of 10 minutes, the mixture should be at base pressure; if not, the timing should be consistent between runs to avoid inconsistent evaporative loss of amines. Prepare TOP for injection (use 21G or smaller needle) in the glove box. Retrieve TOP syringe from glove box and inject.

4. Degas flask content for an extra 5 minutes. The pressure should fall back to base pressure within this time frame.

5. Switch to N_2. Turn Variac to full power (100%) and change temperature set point to nucleation temperature T_{Nuc}+1.0°C to begin ramping, which generally takes between 17-20minutes. Do not use glass wool to speed up the process as it may create temperature control problems later. The longer ramp time is due to the very high nucleation temperature, which is also approaching the boiling point for HDA. During the temperature ramping, prepare syringes for injection during both nucleation and growth in the glove box.

6. The following set of syringes is to be prepared:

    A. Cd-OPA+TOP-Te+DPP+Squalene for NUCLEATION; 5-6mL syringe / 16G needle.

B. TOP-Se (+TOP-S) for NUCLEATION; 1mL syringe / 21G needle. Do not use 16G needle for 1mL (or any non-Luer locked) syringe as the pressure inside the flask will dislodge the two.
C. Cd-OPA for GROWTH; 1mL syringe / 21G needle.
D. ODE-S for OVEROCOAT; 16G needle for quick injection
E. Cd-OPA for OVERCOAT; 21G needle

Shake all precursors stock solutions, including the chalcogenide solutions and in particular, the 0.5M Cd-OPA in TOP solution immediately before drawing out volumes. When mixing *Syringe A*, add Cd-OPA last, then mix the content by drawing and injecting the solution in and out of the preparation vial several times before loading. Keep the syringes in the glove box until it is time to inject.

7. Once the flask content stabilizes at T_{Nuc}+1.0°C (do not wait as amine content may decrease via evaporation), retrieve the syringes from glove box and unlock the needle cap for all of them. Immediately proceed to the following step, which must be performed at quick succession.

8. NUCLEATION **start timer, t_{Nuc} = 0sec**: Lower temperature set point to $T_{Gro-set}$ = 315°C, insert both syringes A and B needles through separate septa. When temperature drops 1.0°C to nucleation temperature, inject A, then B in close sequence. Note the temperature drop for future reference. Do not remove the heat pad.

9. GROWTH: begin *Syringe C* Cd-OPA injection to supplement Group II precursors for growth at designated time t_{Cd-Gro}, at the specified injection rate(s) r_{Cd-Gro}; in some cases, r_{Cd-Gro} increases over time, similar to during SILAR when more precursors are introduced for consecutive semiconductor monolayer growth.

Follow the rate as closely and as evenly as possible; for example, if 0.9mL Cd-OPA is to be injected over the course of 1 minute, with 1/3=0.3mL in the first 30 sec and 2/3=0.6mL in the second 30 sec, then during the first 30sec the injection rate can be 0.1mL / 10 sec, and during the second 30sec, 0.2mL / 10 sec. Note the temperature during growth, T_{Gro}, and record for future references; with appropriate temperature controller settings, nucleation temperature ~350-360°C and injection of ~3.0-3.5mL total, the temperature should bounce back to the set point temperature (315°C) almost immediately with minimal heat input and without overshooting. It is, however, likely that the mean T_{Gro} will deviate several degrees from 315°C.

10. At the end of growth (time t_{Gro}), turn Variac power to 0% and remove heat pad.

11. OVERCOAT: Wait for temperature to cool to $T_{ODE\text{-}S}$, inject *Syringe D*, ODE-S in one go and record the time, $t_{ODE\text{-}S}$. For samples provided with an overcoating temperature set point $T_{OC\text{-}set}$ (=200°C for this protocol series), change it and when temperature reading falls to near $T_{OC\text{-}set}$, place heat pad under flask again and return Variac to 100% power. If $T_{OC\text{-}set}$ is "NA" ("not applicable"; for samples with short overcoating duration), ignore this step. Note that this step is likely to overlap, timing wise, with the next step.

12. OVERCOAT: Start *Syringe E* Cd-OPA to supplement Group II precursors for overcoat at designated time $t_{Cd\text{-}OC}$, at the specified injection rate(s) $r_{Cd\text{-}OC}$. Note the temperature during overcoat, T_{OC}, and record for future references. Mild overshooting (from the high temperature of the heat pad after synthesis) is expected and accounted for in setting $T_{OC\text{-}Set}$, which is lower than the actual target overcoating temperature; for an actual target overcoating temperature between 210-215°C, for example, $T_{OC\text{-}Set}$ is set at 200°C; T_{OC} should not exceed

220°C with appropriate temperature controller settings. Begin cool down to 80°C at time t_{end}.

13. Inject 12mL anhydrous hexanes retrieved from glove box, transfer solution into N_2-filled septum vial and transfer into the glove box for storage; <0.5mL ethanol can be added to keep the solution fluid, but only if necessary.

Table 3: Specifications of synthesis conditions for CdS@$CdTe_xSe_{1-x}$ QDs.

	CdTeSeS #Em: 733/43	**CdTeSeS ##Em: 750/45**	**CdTeSeS ###Em: 782/61**
TOPO *Starting chemical*	6.960 g (18.000 mmol)	6.960 g (18.000 mmol)	6.960 g (18.000 mmol)
Hexadecylamine *Starting chemical*	0.869 g (3.600 mmol)	0.724 g (3.000 mmol)	0.869 g (3.600 mmol)
TOP *Inject after 10min degas*	0.670 mL (1.500 mmol)	0.670 mL (1.500 mmol)	0.670 mL (1.500 mmol)
Squalene *Nucleation: Syringe A*	2.940 mL	2.940 mL	2.923 mL
DPP *Nucleation: Syringe A*	0.0042 mL (0.024 mmol)	0.0052 mL (0.300 mmol)	0.0042 mL (0.024 mmol)
TOP-Te 1.0M *Nucleation: Syringe A*	0.060 mL (0.060 mmol)	0.060 mL (0.060 mmol)	0.060 mL (0.060 mmol)
0.5M Cd-OPA in TOP *Nucleation: Syringe A*	0.240 mL (0.120 mmol Cd)	0.300 mL (0.150 mmol Cd)	0.240 mL (0.120 mmol Cd)
TOP-Se Various M *Nucleation: Syringe B*	1.8M: 0.0167mL (0.030 mmol) (Te:Se 2:1)	1.2M: 0.100 mL (0.120 mmol) (Te:Se 1:2)	1.2M: 0.100 mL (0.120 mmol) (Te:Se 1:2)
TOP-S 2.24M *Nucleation: Syringe B*	0.3348 mL (0.7500 mmol)	NA	NA
0.5M Cd-OPA in TOP *Growth: Syringe C*	0.180 mL (0.090 mmol Cd)	0.210 mL (0.105 mmol Cd)	0.210 mL (0.105 mmol Cd)
ODE-S, Saturated	4.140 mL	0.900mL	4.320mL

Overcoat: Syringe D			
0.5M Cd-OPA in TOP *Overcoat: Syringe E*	0.300 mL (0.150 mmol Cd)	0.300 mL (0.150 mmol Cd)	0.300 mL (0.150 mmol Cd)
T_{Nuc} *Nucleation Temp.*	357.5°C (T ↓ to 301.7°C after Syringe A+B injection)	357.5°C (T ↓ to 306.5°C after Syringe A+B injection)	357.5°C (T ↓ to 308°C after Syringe A+B injection)
t_{Nuc} *Time of Nucleation (always 0: begin timing)*	0 sec	0 sec	0 sec
$T_{Gro\text{-}set}$ *Growth Temp.: Set point*	315°C	315°C	315°C
$t_{Cd\text{-}Gro}$ *Time, start Growth Cd-OPA (Syringe C) injection*	30sec	30sec	30sec
$r_{Cd\text{-}Gro}$ *Injection Rate of Growth Cd-OPA (Syringe C)*	0.030mL/30sec for t=30-210sec (3min total) Done at 210sec	0.07mL/60sec for t=30-90sec 0.14mL/60sec for t=90-150sec Done at 150sec	0.07mL/60sec for t=30-90sec 0.14mL/60sec for t=90-150sec Done at 150sec
t_{Gro} *Total Growth time*	240sec	180sec	180sec
T_{Gro} *Growth Temp. (Mean)*	323°C	323°C	324°C
T_{ODE} *ODE Inject Temp.*	245°C	285°C	260°C
t_{ODE} *ODE Inject time*	360sec (6min)	240sec (4min)	255sec (4min)
$T_{OC\text{-}Set}$ *Overcoat Temp.: Set point*	200°C	NA (No heat input; T falls naturally during	200°C

		overcoat)	
$t_{Cd\text{-}OC}$ *Time, start Overcoat Cd-OPA (Syringe E) injection*	480sec (8min)	270sec (4min30sec)	540sec (9min)
$r_{Cd\text{-}OC}$ *Injection Rate of Overcoat Cd-OPA (Syringe E)*	0.01mL/20sec for t=8-18min Done at 18min	0.05mL/30sec for t=270-330sec 0.10mL/30sec for t=330-390sec Done at 390sec	0.01mL/30sec for t=9-14min 0.02mL/30sec for t=14-19min Done at 19min
T_{OC} *Overcoat Temp. (Mean)*	208°C	225°C	200°C
t_{end} *Time, end Overcoat & cool*	20min	6min30sec	23min

TEM and spectral data of these QDs will be shown in section 3.6.1.2. TOP-S has been introduced in Nucleation *Syringe B* (with Se precursors) with the intended goal of elevating group VI concentration early to drive full Te and Se incorporation, while permitting a lower [Se] such that the Te:Se ratio is 2:1—near the composition at which the longest fluorescence wavelengths can be achieved based on optical bowing estimation (Figure 2.2). Inclusion of sulfur in the protocols has widened the fluorescence profiles with no observable changes in the size and shape uniformity of the nanocrystals under TEM; overall, these sulfur-inclusive protocols have produced QDs with the best morphology and uniformity to date, while also showing evidences suggestive of strengthened type II character for a given wavelength (see section 3.6.3).

3.5.3 Protocol for Flocculation of (CdS@)$CdTe_xSe_{1-x}$

Flocculations that prepare (CdS@)$CdTe_xSe_{1-x}$ QDs for storage, overcoating and water solubilization are performed in the N_2 environment in its entirely, using anhydrous

solvents including anhydrous hexanes, ethanol, propanol, butanol and methanol, all of which are available from Sigma Aldrich (St Louis, MO). Syringes are employed for solvent transfer to ensure consistent volumes are used between runs for a given protocol. As the protocol changes, the conditions may require small changes. The following guidelines may help with modifications:

- Always start with a spin-down to remove as much insoluble Cd-OPA + amines salts (off-white in color) as possible. The spin speed can be high as long as the QDs do not flocculate.

- For crashing out, the non-solvent volume is ideally close to the minimal amount required to flocculate the QDs, such that non-QD materials are most likely to stay in the supernatant to be discarded. QDs should therefore be thoroughly suspended in the solvent before adding the non-solvent, and the non-solvent should be added slowly and with continuous shaking so that the minimal volume needed can be determined. Higher solvent volumes lead to cleaner QDs after the crashout when this condition is met; its maximum volume is limited by the non-solvent's ability to crash out the QDs. Meanwhile, centrifuge speed can be adjusted according to the weight of the QDs to allow better-paced, better resolved flocculations: the heavier $CdTe_1Se_{1-x}$ QDs, in general, can be flocculated at a slower spin speed compared to CdSe QDs, further preventing the precipitation of unwanted ligands etc. from the supernatant.

- MSNCs' fluorescence (often blue to yellow) tends to be sufficiently far removed from the (CdS)@$CdTe_1Se_{1-x}$ QDs' to be easily observable in the supernatant during the early rounds of crashout. Checking for the signal is therefore a good way to estimate the concentrations of MSNCs in addition to looking for them under TEM, in which the ultra small nanocrystals can be

elusive. As previously noted, the Cd-OPA and amine salt pellets are also good "hiding places" for MSNCs. MSNC fluorescence should no longer be visible in the supernatant of the last round of crashout.

- If the synthesis produces large quantities of Cd-OPA+amine salt that cannot be effectively removed with hexanes as solvent—this can manifest as the QD-hexanes stock solution "gelling up" after days in storage—replace 50% of the hexanes volume with toluene in every round of crashouts except the first one. However, store the QDs in hexanes only.

The protocols below have been developed based on crashing out the full volume of growth solution from one synthesis as described in sections 3.5.1 and 3.5.2. They can be scaled down for partial volumes, provided that the growth solution is well mixed when divided into aliquots.

3.5.3.1 The 1-Alcohol "Standard" Flocculation Protocol

This protocol assumes that the QD growth solution contains 12mL anhydrous hexanes (+ <0.5mL ethanol) in storage, as is the case for all synthesis protocols described above. If not, add hexanes and make sure the solution is completely fluid (i.e., with no clumps of TOPO) before proceeding to step 1.

1. SALT REMOVAL 1: Spin down the solution at 3.9krpm, 5min. A salt pellet should precipitate. Transfer the supernatant (with the QDs) into a fresh 50mL centrifuge tube.

2. SALT REMOVAL 1: Place 6mL hexanes into the salt pellet and re-suspend it by vortexing, then spin down again at 3.9krpm/5min. This washes the pellet to collect all QDs and the pellet should be off-white afterwards. Transfer the

hexanes supernatant into the supernatant from step 1, so the growth solution has 18mL hexanes total. Discard pellet.

3. 1st CRASHOUT: Add 18mL ethanol slowly and with constant shaking to mix it well. Centrifuge at 3.3krpm for 5min to flocculate the QDs. This should leave mostly MSNCs in the supernatant; if some QDs remain in the supernatant, transfer the supernatant into a different tube (so to avoid extended contact between the QD pellet and ethanol), add ethanol in 3mL increments and spin at 3.3kprm/2.5min to flocculate them.

4. Discard the supernatant. Reverse the centrifuge tube with QD pellets and set it upside down on a paper towel for several minutes to drain remaining solvent (ethanol doesn't evaporate quickly). Re-suspend all QDs in 6mL hexanes. Vortex briefly.

5. SALT REMOVAL 2: Spin down at 3.9krpm / 5min. A small off-white pellet will likely precipitate. Transfer the QD-containing supernatant into a fresh tube while filtering the solution with a 0.1-0.2um PTFE syringe filter. There should be no clogging at this point, but if there is and the clog is lightly- or un-colored in the filter, spin the supernatant again to remove more salt. If the clog is of the same color as the QDs, then it is likely that the QDs have aggregated.

6. 2nd CRASHOUT: Add an additional 6mL hexanes (→ 12 mL hexanes total). Then add 12 mL ethanol slowly and shaking the tube to ensure good mixing. Spin down 3.3krpm/5min.

7. Discard the supernatant. Reverse the centrifuge tube with QD pellets and set it upside down on a paper towel for several minutes to drain remaining solvent. Re-suspend the QDs in 3mL hexanes and vortex briefly.

8. SALT REMOVAL 3: Spin down again at 3.9krpm/5min. Salt rarely precipitates at this point but if there is, transfer the QD-containing supernatant into a fresh tube.

9. 3rd CRASHOUT: Add additional 3mL hexanes (→ 6 mL hexanes total). Then add 6 mL ethanol slowly and shaking the tube to ensure good mixing. Spin down at 3.3krpm/5min.

10. Discard the supernatant. Reverse the centrifuge tube with the QD pellet and set it upside down on a paper towel to drain remaining solvent. Re-suspend in 3mL hexanes and store in a close-capped vial (do not use septum vial as the solution dries out quickly over time). ≤0.1%v/v of TOP can be added at this point, if the QDs have to be stored long term.

3.5.3.2 *The Multi-Alcohol "High Resolution" Flocculation Protocol: for Growth Solutions with Difficult to Remove MSNCs.*

Multi-alcohol flocculations was originally developed for syntheses using as-purchased rather than recrystallized 98% hexadecylamine, which retained a small population of MSNCs (and their QD progenies) that was poorly removed by the "standard" flocculation protocol. Over the course of this project, the general strategy of using multiple alcohols during flocculation to improve separation of different QD subpopulations has proven applicable to a variety of synthesis and overcoating protocols, although the appropriate solvent / non-solvent volumes and endpoints do differ and at times significantly.

The following protocol was successfully used on QDs synthesized using protocols almost identical to those delineated in section 3.5.1, but with as-purchased 98% HDA

and also stored in 8mL TOP + 6mL anhydrous hexanes instead of 12mL anhydrous hexanes. Loss analysis has been performed on the QDs left in the supernatant to be discarded from each crashout; they were flocculated separately and imaged by TEM, the data from which will be shown in Figure 3.12 in section 3.6.2.

1. 1st CRASHOUT: In the growth solution stored with 6mL hexanes + 8mL TOP, add 30mL ethanol. Spin down at 3.3kprm/5min. Decant and drain supernatant.

2. SALT REMOVAL: Re-suspend QDs in 3mL hexanes. Spin down insoluble Cd-OPA + amine salt pellet at 3.9krpm/5min and transfer the QD-containing supernatant to a fresh tube. Wash pellet with 1mL hexanes and combine supernatant with the 3mL QD solution.

3. 2nd CRASHOUT: Add 2mL hexanes so that total hexanes volume is 6mL. Add 12mL 1-propanol. Spin down at 3.6krpm/5min. Decant and drain supernatant.

4. 3rd CRASHOUT: Repeat 2nd crashout—re-suspend QDs in 6mL hexanes, add 12mL 1-propanol and spin down at 3.6krpm/5min. Drain supernatant.

5. 4th CRASHOUT: Re-suspend QDs in 1mL hexanes. Add 10mL 1-butanol and spin down at 4.5krpm/5min. Decant and drain supernatant.

6. 5th CRASHOUT: Re-suspend QDs in 6mL hexanes. Add 2mL 1-butanol and 6mL methanol and spin down at 3.0krpm/5min. Decant and drain supernatant.

7. Re-suspend QDs in 1mL hexanes, filter with 0.2um syringe filter and spin down residual salt at 3.9krpm/5min. Transfer the QD-containing supernatant to a closed capped vial and adjust hexanes volume for storage.

3.5.3.3 *Flocculating (CdS@)$CdTe_xSe_{1-x}$ for TEM: A Quick Note*

While the above flocculation protocols are designed to clear all MSNCs from the (CdS@)$CdTe_xSe_{1-x}$ QDs for storage and further processing, flocculations performed on QDs for TEM have aimed to retain the extraneous nanocrystal populations for imaging. The growth solution has a small aliquot retrieved for TEM before transfer into the glove box, and flocculation on this aliquot is performed as described in section 3.5.3.1 but scaled down according to the aliquot volume. The ethanol: hexanes ratio is elevated from 1:1 to ~3:1 for each crashout. If extraneous populations were found in this TEM aliquot, the storage QD solution also undergoes TEM to confirm that the "standard" flocculation protocol manages to clear them completely.

3.6 Data Pertaining to the Synthesis and Overcoating of (CdS@)$CdTe_xSe_{1-x}$ QDs

3.6.1 Properties of (CdS@) $CdTe_xSe_{1-x}$ QDs

3.6.1.1 $CdTe_xSe_{1-x}$ QDs Synthesized Using Protocols Described in 3.5.1.1

TEMs of the $CdTe_xSe_{1-x}$ QD series synthesized using identical (marked by asterisks *) or similar protocols to those described in section 3.5.1, including the average sizes of the nanocrystals, are shown in Figure 3.4.

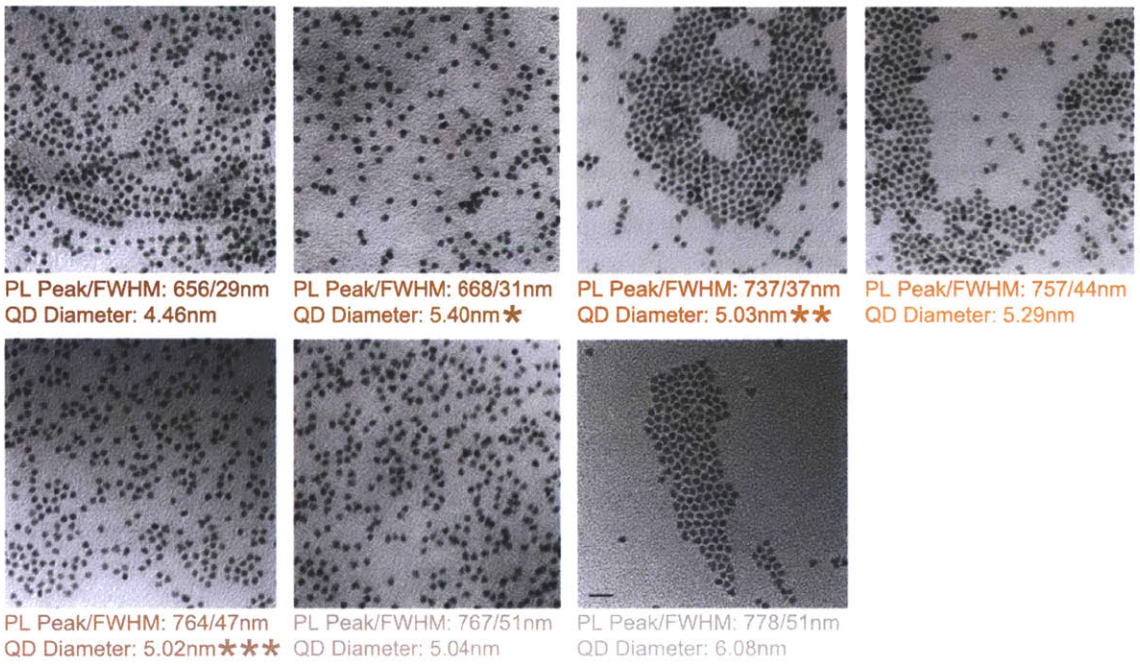

Figure 3.4: TEM of $CdTe_xSe_{1-x}$ QDs with peak fluorescence from 656 to 778nm. The first two samples are CdTe QDs. */**/*** denote samples with their synthesis protocol described in section 3.5.1. Morphologically, the nanocrystals in this series fare very well in both shape and uniformity, but slightly worse than those to be shown in Figure 3.6, which include sulfur in their precursors, as the ligands and TOPO quantities were optimized for as-purchased 98% HDA rather than the recrystallized amine used in these syntheses. Optimization for the use of recrystallized HDA as well as inclusion of sulfur would involve increasing the amount of TOPO while decreasing the amounts of HDA and Cd-OPA during emitter growth. Scale bar=20nm.

Figure 3.5 below shows the optical spectra of the same series of QDs:

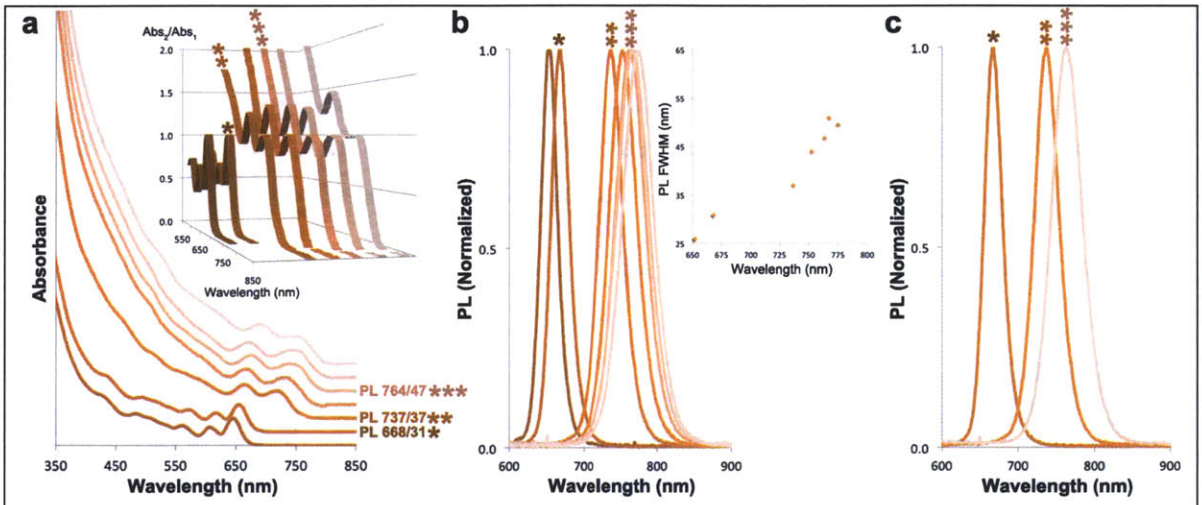

Figure 3.5: Optical spectra of $CdTe_xSe_{1-x}$ QDs. */**/*** denote samples with their synthesis protocol described in section 3.5.1. The two lowest wavelength samples are CdTe QDs. a) Absorption spectra, each showing a 2nd absorption band near the band edge. Significance of the relative height ratio of the two local maxima, Abs_2/Abs_1, which is shown in the upper corner with Abs_1 normalized to 1, will be discussed later section 3.6.3. b) Fluorescence spectra showing symmetric profiles, the upper right corner shows their FWHM vs. peak wavelength. c) Fluorescence spectra showing only the marked samples.

Notably, the size range of these QDs is quite small, in marked contrast from the series of homogenously alloyed $CdTe_{0.66}Se_{0.34}$QDs reported by Bailey and Nie [13], which spanned a similar range of wavelengths but with sizes between 2.7 to 7.0nm. By holding constant the quantity and timing of tellurium entry, the synthesis protocols presented in section 3.5.1 uniformizes the amount of nucleates and hence, the amount of precursors needed for growth and simplifies protocol optimization for the whole series, but at the cost of strengthened type II character especially for long wavelength samples; fluorescence tuning is expected to occur mostly via changes in

composition and its gradient, adding a small number of monolayers that are Se and S-enriched. That a composition gradient exists in these QDs and is likely strengthening as wavelength increases will imply a drop of quantum yield, which will be seen in the next QDs series that includes the addition of sulfur.

3.6.1.2 CdS@CdTe$_x$Se$_{1-x}$ QDs Synthesized Using Protocols Described in 3.5.1.1

TEMs of the CdS@CdTe$_x$Se$_{1-x}$ QD series synthesized using identical (marked by hash symbols #) or similar protocols to those described in 3.5.2 are shown in Figure 3.6. Quantum yield (QY) and size information are also included; details on how QY values are determined can be found in Appendix 5.1.

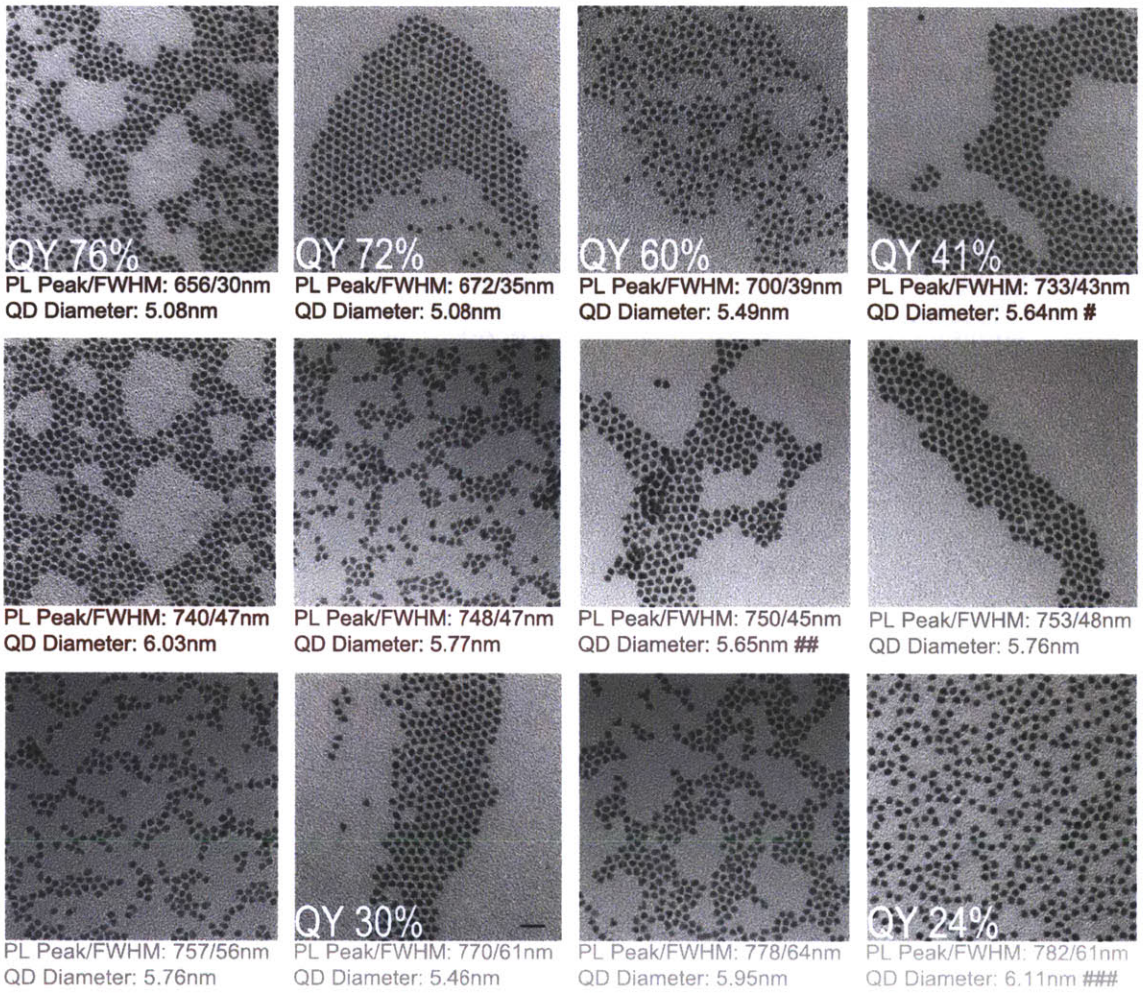

Figure 3.6: TEM of CdS@$CdTe_xSe_{1-x}$ QDs with fluorescence peaks from 656nm to 782nm. The first sample has a CdTe emitter. #/##/### denote samples with their synthesis protocol described in section 3.5.2. Post standard crashout (section 3.5.3.1) quantum yields, if measured, are also indicated. Crashout of the **PL740/47** sample followed the flocculation protocol described in section 3.5.3.3 for TEM, thus retaining the CdS MSNCs nucleated during the overcoating stage; for comparison, sample **PL700/39**, which encountered a similar problem, was flocculated using the standard protocol described in section 3.5.3.1 and was free of extraneous nanocrystal populations. Scale bar=20nm.

As in the case of $CdTe_xSe_{1-x}$ QDs (Figure 3.4), the sizes of these QDs are fairly consistent through the wavelength series, with only a mild increasing trend towards

longer fluorescent wavelengths. Meanwhile, the quantum yield decreases, also likely due to a strengthening type II character as tellurium entry conditions were held consistent for this series as well. Figure 3.7 shows the absorption and fluorescence spectra of the same series of CdS@$CdTe_xSe_{1-x}$ QDs:

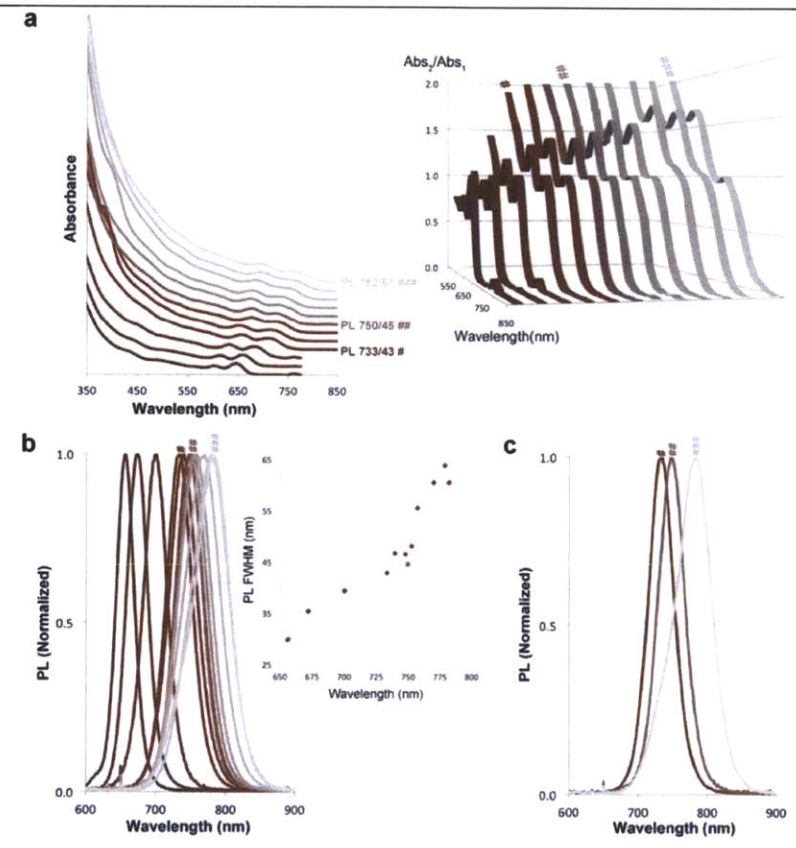

Figure 3.7: Optical spectra of CdS@$CdTe_xSe_{1-x}$ QDs. #/##/### denotes samples with synthesis protocol described in section 3.5.2. a) Absorption spectra also contain prominent 2nd absorption band features adjacent to each band edge; at lower wavelengths, the presence of CdS is evident in some samples. Upper right corner also shows a normalized Abs_2/Abs_1 plot with a clear increasing trend of Abs_2 towards longer fluorescence wavelengths. b) Fluorescence spectra and its FWHM vs. peak wavelength; the slight increase in FWHM after sulfur inclusion (see Figure 3.8) may be due to CdS further augmenting the type II character of the QDs, given that these QDs are highly uniform morphologically. c) Fluorescence spectra of only the marked samples. The slight "shoulder" on the hypsochromic side of **PL782/61** (###)'s fluorescence peak has been observed occasionally after overcoating and is not removable by flocculation.

Fluorescence peak FWHM as function of peak wavelength of this CdS@$CdTe_xSe_{1-x}$ QD series is compared against that of the $CdTe_xSe_{1-x}$ QD series in Figure 3.8. Also included

in the plot is an older $CdTe_xSe_{1-x}$ QD series synthesized using protocols similar to those described in section 3.5.1 but with as-purchased 98% HDA. The PL FWHM values for the sulfur-free emitters have been fairly consistent over the course of this project, even though the synthesis protocols have evolved significantly and the resulting QD morphology has seen vast improvements (see Figure 3.13 and Figure 3.14, section 3.6.3).

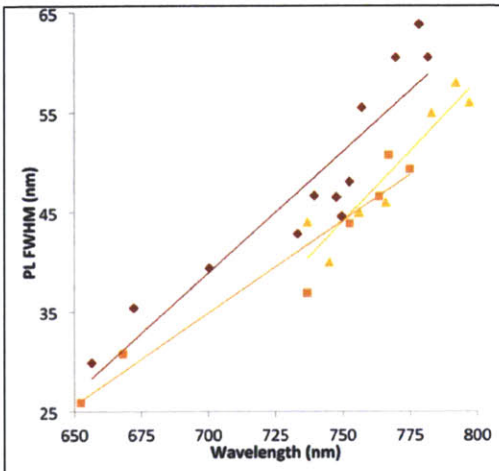

Figure 3.8: Fluorescence FWHM vs. peak wavelength of (CdS@)$CdTe_xSe_{1-x}$ QDs. Key: orange: $CdTe_xSe_{1-x}$ QDs synthesized as described in section 3.5.1 (also seen in Figure 3.5 b); red: CdS@$CdTe_xSe_{1-x}$ QDs synthesized as described in section 3.5.2 (also seen in Figure 3.7 b); yellow: $CdTe_xSe_{1-x}$ QDs synthesized as described in section 3.5.1, but with as-purchased 98% HDA. Colored lines are linear regression plots of the experimental data points.

The crystal structure and composition of a subset of CdS@$CdTe_xSe_{1-x}$ QD samples were examined by X-ray diffraction (XRD) and inductively coupled plasma atomic emission spectroscopy (ICP-AES). XRD (Figure 3.9) reveals the crystal structure of these QDs is of mixed zinc blende and wurtzite character, which has been observed in both single-semiconductor (ex. CdSe [211]) and $CdTe_xSe_{1-x}$ QDs [144]. It is practically very challenging to determine experimentally if the mixing occurs on the population scale, as in subpopulations of pure wurtzite and pure zinc blende being mingled together, or if it occurs on the individual scale, as in each QD carrying both crystalline phases [211].

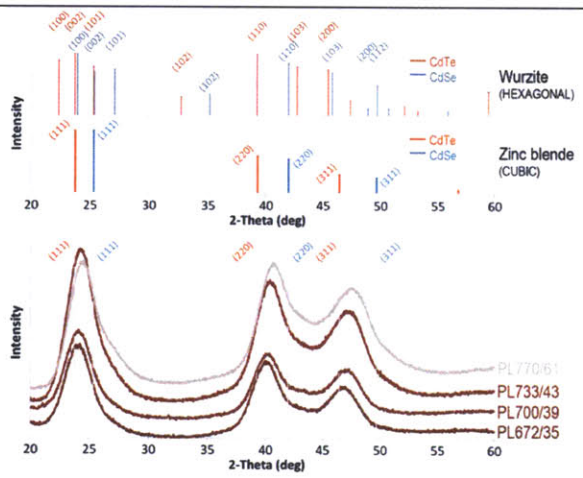

Figure 3.9: Crystal structure of selective CdS@$CdTe_xSe_{1-x}$ QD samples, analyzed by X-ray diffraction (XRD). For reference, XRD patterns of bulk wurtzite and zinc blende CdTe and CdSe in the same 2θ range, as well as the Miller indices (*h k l*) of the peaks' corresponding crystal planes, are also provided (top two plots). CdS@$CdTe_xSe_{1-x}$ QD samples are of mixed zinc blende and wurtzite character, with the former being dominant. In the 2θ=20-30°range, zinc blende CdTe and CdSe has one prominent peak whereas wurtzite has three due to the latter's loss of symmetry in its crystal structure. For the same reason, the 2θ=37-50° range carries two prominent peaks in zinc blende but three in wurtzite. The broad diffraction peaks in QDs compared to bulk are caused by their finite sized crystal domains. Based on this data, CdS@$CdTe_xSe_{1-x}$ QDs are expected to be close to zinc blende, in that their XRD patterns do not contain the prominent (103) wurtzite peak at 2θ ~42-45° that should fall between the (220) and (311) zinc blende peaks. Nonetheless, the non-zero intensity count in the region is indicative of the presence of some wurtzite, and its elevated relative value, compared to the (220) zinc blende peak (equivalent to (110) wurtzite), in longer wavelength CdS@$CdTe_xSe_{1-x}$ QDs suggest stronger wurtzite character in these samples. This is not surprising as CdSe and CdS, which are more abundant in these samples (see Figure 3.10), favor the wurtzite lattice more than CdTe, which favors zinc blende unless the kinetics of the synthesis is very aggressive. A shoulder on the right hand side of the (111) peak is also observed in longer wavelength CdS@$CdTe_xSe_{1-x}$ QDs, which is likely a manifestation of the (101) wurtzite peak. An in-depth study will be needed to determine with certainty whether the zinc blende phase co-exists with wurtzite within each QD or whether it forms its own subpopulation of nanocrystals. The sample peaks of CdS@$CdTe_xSe_{1-x}$ QDs fall between CdTe and CdSe values as expected from their alloyed compositions, and the shift towards CdSe as wavelength increases agree with the composition data, as shown next in Figure 3.10.

Elemental analysis by ICP-AES (Figure 3.10) confirms the presence of sulfur and at a composition equivalent to 1-1.5 monolayers of CdS overcoat. It also indicates that the Te:Se compositional ratios in these QDs are sensitive and above all, similar to the molar ratio of tellurium and selenium precursors introduced during synthesis.

	PL672/35	PL700/39	PL733/43	PL770/61
Cd%	1.08	1.17	1.11	1.10
Te%	0.64	0.65	0.51	0.42
Se%	0.00	0.13	0.23	0.24
S%	0.36	0.22	0.26	0.34
Te:Se in QDs		0.83 : 0.17	0.69 : 0.31	0.64 : 0.36
Te:Se in precursors	0.80 : 0.20	0.80 : 0.20	0.66 : 0.33	0.57 : 0.43
% CdS Vol	29.2%	17.6%	21.4%	28.7%
CdS Monolayers	1.5	<1.0	1.0	1.5

Figure 3.10: ICP-AES elemental analysis of 4 samples in the CdS@$CdTe_xSe_{1-x}$ wavelength series. Sulfur is present at quantities equivalent to 1 to 1.5 monolayers of overcoat, which is ~50% of what is ideal for full oxidation protection. Moreover, alloying between the $CdTe_xSe_{1-x}$ emitter and the CdS overcoat is possible, which would further compromise the surface coverage of CdS and its ability to protect the emitter against oxidative damage. The relatively low CdS% in PL700/39 is likely due to the nucleation of CdS, which is visible both in the TEM and the absorption spectrum of the sample (Figure 3.6 and Figure 3.7). Each sample is also enriched in cadmium, consistent with previous observations of QDs with strong, dative X-type phosphonate ligands. Increasing the Se composition in the QDs is at least partly responsible for the extension of wavelength between samples **PL700/39**, **PL733/43** and **PL770/61**, which are of equivalent sizes (Figure 3.6) (composition gradient may play a role as well), and was implemented by introducing more Se precursors at nucleation while the amount of Te precursors was held constant at 0.06mmol. Overall, the Te: Se compositional ratios in the QDs and the precursors agree well with one another ("what you add is what you get"), easing the prediction of fluorescence wavelength at the planning stage of synthesis. While the QDs consistently contain more Te, which is expected from the kinetic difference between TOP-chalcogenide precursors and a non-unity reaction yield, the small difference in their Te: Se ratio from their precursor input's suggests a diffusion-based, sterically driven growth, which is nonetheless not conductive to creating a sharp emitter / overcoat composition gradient during overcoating. The 64% Te: 36% Se ratio of **PL770/61** should be able to achieve the longest wavelength based on optical bowing calculations (Figure 2.2).

As already mentioned, the general trend of decreasing quantum yield as wavelength increases in the CdS@$CdTe_xSe_{1-x}$ QD series is likely due to the strengthening of their type II character, which is also suggested by the trend of Abs_2/Abs_1 and the distance between the two absorption bands ($d_{abs1\text{-}abs2}$) that will be discussed in further details in section 3.6.3. Coverage of the Cd-OPA coordination polymer surface ligand may also modulate QY values; reduced coverage may favor the incorporation of CdS especially in longer wavelength samples but compromise QY. While QY is an important performance parameter, its values are only meaningful at the application stage and are irrevocably connected to the environmental stability of Te-containing nanocrystals.

This CdS@$CdTe_xSe_{1-x}$ QD series display sufficient air stability for amphiphilic polymer encapsulation experiments, which will be described in detail in section 3.7. Air stability is quantified as the ability to hold on to its air-free QY value in a dilute ($absorbance_{max}$ at 350nm < 0.1) hexanes solution that is stored under room light and capped in air. To date, only one sample (***, PL 782/61) has demonstrated no drop in QY value for more than 4 days, and insufficient surface coverage of overcoating sulfides is likely the cause of this instability. Short-term stability of these QDs, while sufficient for determining the appropriate methods for water solubilization, has prevented these QDs from becoming truly application-ready. Figure 3.11 presents the air stability data of 4 samples in this QD series:

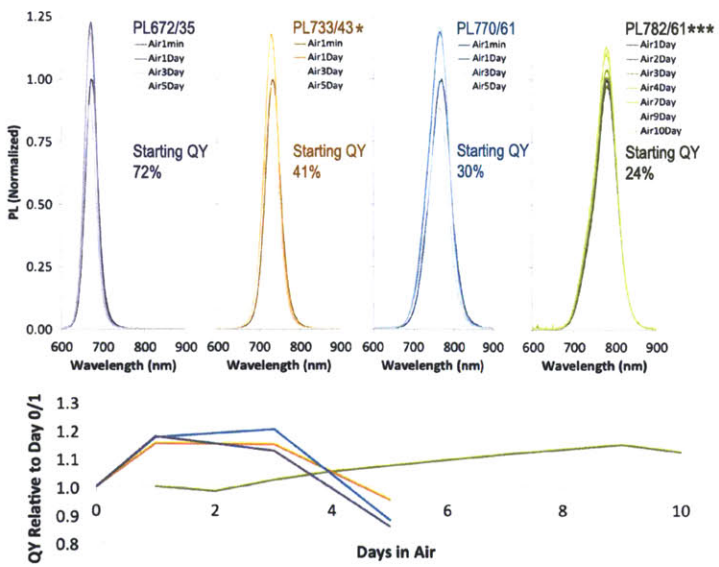

Figure 3.11: Stability of selected CdS@$CdTe_xSe_{1-x}$ QD samples, including two (*/***) with synthesis protocols described in 3.5.2. a) PL profile of each sample, the concentration of which in hexanes were consistent, recorded after various durations of air storage; b) the area of the PL peaks relative to the first recorded value, which is equivalent to the relative QY compared to the starting value provided in a). Water solubilization experiments performed concurrently on other aliquots of **PL672/35** and **PL733/43** sped up and confirmed oxidative degradation that is suggested in this plot after Day 4 (see Figure 3.19).

3.6.2 Removal of MSNCs formed during Synthesis by Multi-Alcohol "High Resolution" Flocculation

The protocol described in section 3.5.3.2 is generally suitable for cleaning up synthesis and overcoating products in which the major and extraneous QD populations are too similar in size and composition to be separable by the 1-alcohol "standard" flocculation protocol (section 3.5.3.1), assuming that a similar solvent / ligand system has been used to prepare the nanocrystals as those described in sections 3.5.1 and 3.5.2.

The example shown in Figure 3.12 is the cleanup of a $CdTe_xSe_{1-x}$ synthesis that was performed using similar protocols as described in section 3.5.1 but used as-purchased

98% hexadecylamine. After 1st to 4th crashouts (labeled EtOH, PrOH-I, PrOH-II and ButOH respectively in accordance to the alcohol used in each), the supernatant was retained, flocculated separately with ethanol (for 1st crashout) and methanol (for 2nd to 4th crashout) and centrifuged at 8000rpm/5min to retain as many nanocrystals as possible; each pellet was then re-suspended in hexanes, imaged with TEM and its absorption and fluorescence spectra determined.

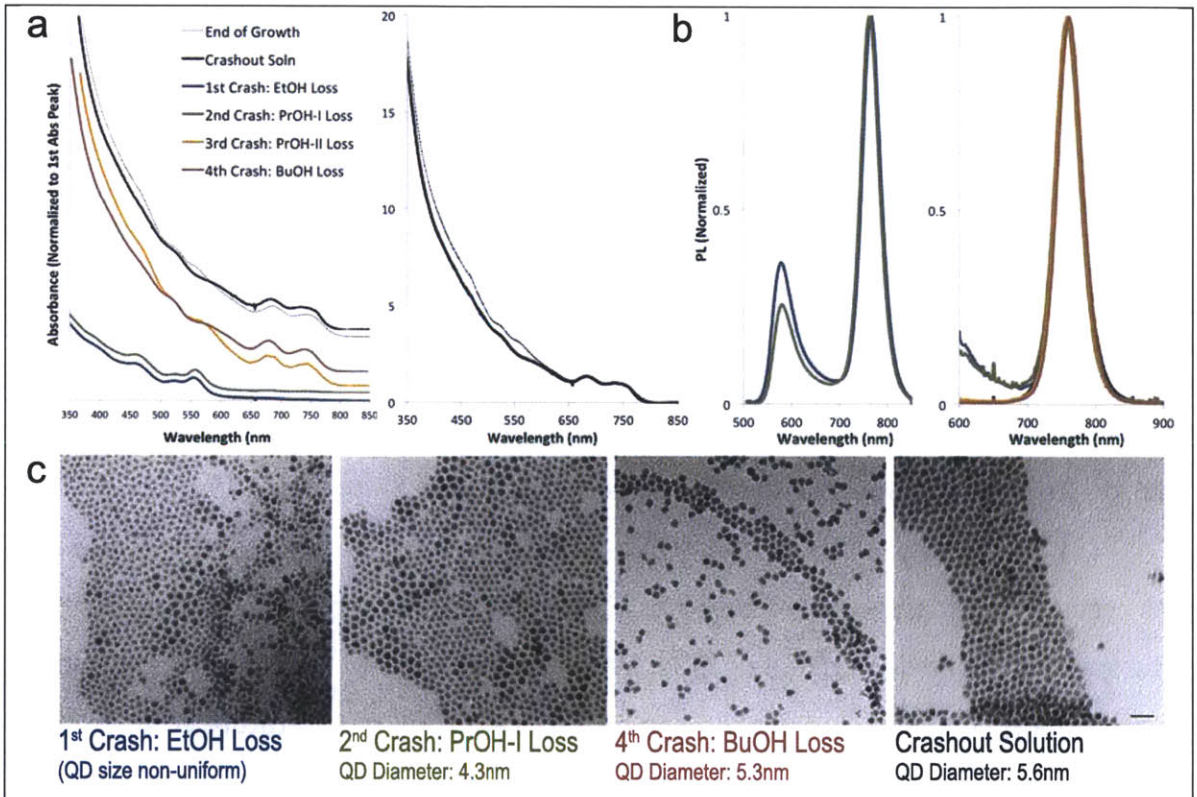

Figure 3.12: Multi-alcohol "high resolution" flocculation, as described in section 3.5.3.2, performed on the products of a $CdTe_xSe_{1-x}$ synthesis contaminated with MSNCs. ***End of Growth*** refers to the QDs as synthesized, i.e. it contains all subpopulations in the growth solution prior to crashout. ***Crashout soln*** is the final, flocculated stock solution of QDs in hexanes. a) Absorption spectra. Left: loss from the first two crashouts (**EtOH, PrOH-I**) is dominated by a smaller but uniform MSNC population with 1st absorption peak at ~560nm, separated from the major population characterized by the double peak feature in the NIR. Right: comparison between ***End of Growth*** and ***Crashout Soln*** only, both curves normalized to the 1st absorption peak to accentuate the difference in features. It is impossible to determine

from the ***End of Growth*** curve alone that extraneous QD populations are present, due to the lack of spectral references for $CdTe_xSe_{1-x}$ QDs. b) Fluorescence spectra. Left: although the small extraneous MSNC population dominates the first two crashout losses in absorption, its fluorescence in the visible wavelengths remains weak compared to the NIR fluorescence from the minute quantities of major population left behind; thus signals from MSNC populations can easily become "invisible" if the major population has not been removed by flocculation. Also, non-zero signal strength between the two distinct peaks suggests that the two populations are actually not distinct. Right: the major population peak is almost identical in every round of the crashout. c) TEM. The presence of multiple QD populations is especially observable in the loss from the 1st ethanol crashout; some populations are likely non-fluorescent. The 4th crashout by butanol turns out to perform size-selective precipitation for the major population. Scale bar=20nm.

3.6.3 Reading the Spectral Profiles of $CdTe_xSe_{1-x}$ QDs

As previously discussed, there have not been sufficient data to create references for the spectral profiles of $CdTe_xSe_{1-x}$ QDs. While the influence of composition gradients on the shape of absorption profiles can be deduced from past literature comparing type I versus type II QDs, it remains difficult to be distinguished from "health" parameters, i.e., those that are purely determined by synthesis conditions, such as crystallinity and uniformity. Literature on $CdTe_xSe_{1-x}$ QDs have measured the composition gradient of their products using elemental analysis [13], which is theoretically sufficient as a characterization tool but is in practice prone to errors from residual precursors and MSNCs remaining in the solution or unintentional selective separation during flocculation. Irreproducibility of synthesis protocols also makes it difficult to verify the gradient or compare between reports.

Observations from this project have made apparent that the shape and width of $CdTe_xSe_{1-x}$ QDs' fluorescence spectra are unreliable indicators of the health of the QD population. In fact, dominance of non-fluorescent species in "bad" samples often results in the narrowest fluorescent spectra. As seen in Figure 3.13 and Figure 3.14, which showcase various qualities of QDs with similar fluorescence peaks (~680nm and 740nm respectively) and their spectral profiles, samples with poor morphology and wide distributions of nanocrystal size and shape can give rise to a photoluminescence (PL) spectrum that is symmetric, narrow and essentially equivalent to that recorded from robust samples.

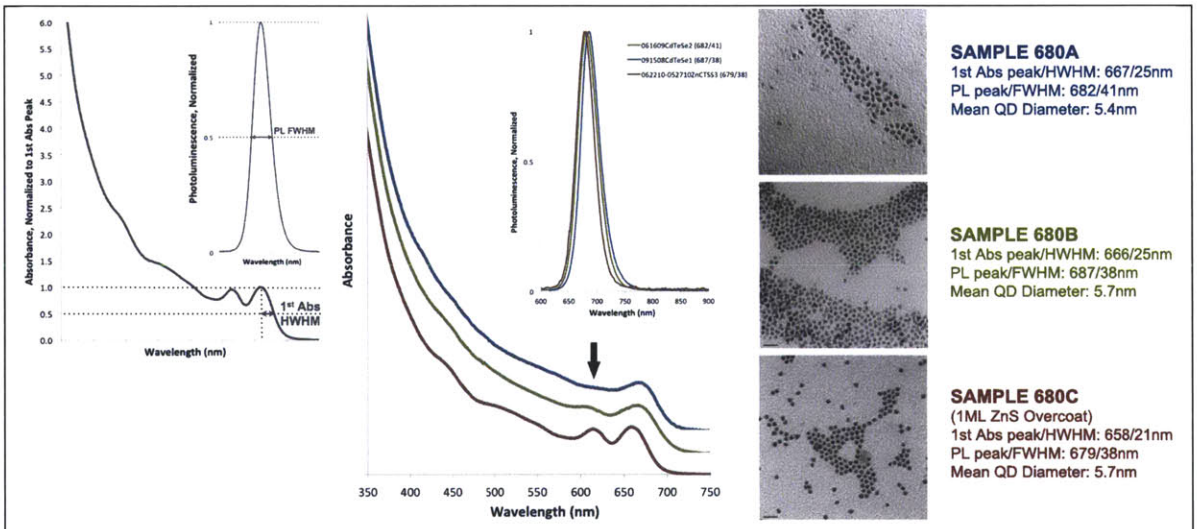

Figure 3.13: Morphological variations in QDs with fluorescence spectra of peak ~680nm and FWHM ~40nm. Sample 680A, an early sample, is heavily contaminated with MSNCs and has poor size and shape uniformity in the major population, which is not apparent from its fluorescence or absorption profile without a reference for the latter. TEM inspection is therefore necessary. Sample 680B has no MSNCs but still has suboptimal shape control; Sample 680C, meanwhile, has very good shape and size uniformity. Sample 680C was synthesized using a protocol similar to those described in section 3.5.2 and is, in effect, **PL656/30** in Figure 3.6 overcoated with an extra monolayer of ZnS from a second overcoating process. It is important to note, however, that while Sample 680C is morphologically robust, its absorption profile is not a "standard" unless the composition gradient of the sample is also known. Fluorescence spectra are therefore poor indicators of

sample quality for $CdTe_xSe_{1-x}$ QDs. Absorption spectra reveals more information: the black arrow points to a 2nd absorption band feature that is likely related to the composition gradient; the HWHM values of the 1st absorption peak may in fact be better indicators of major population uniformity. TEM scale bar = 20nm.

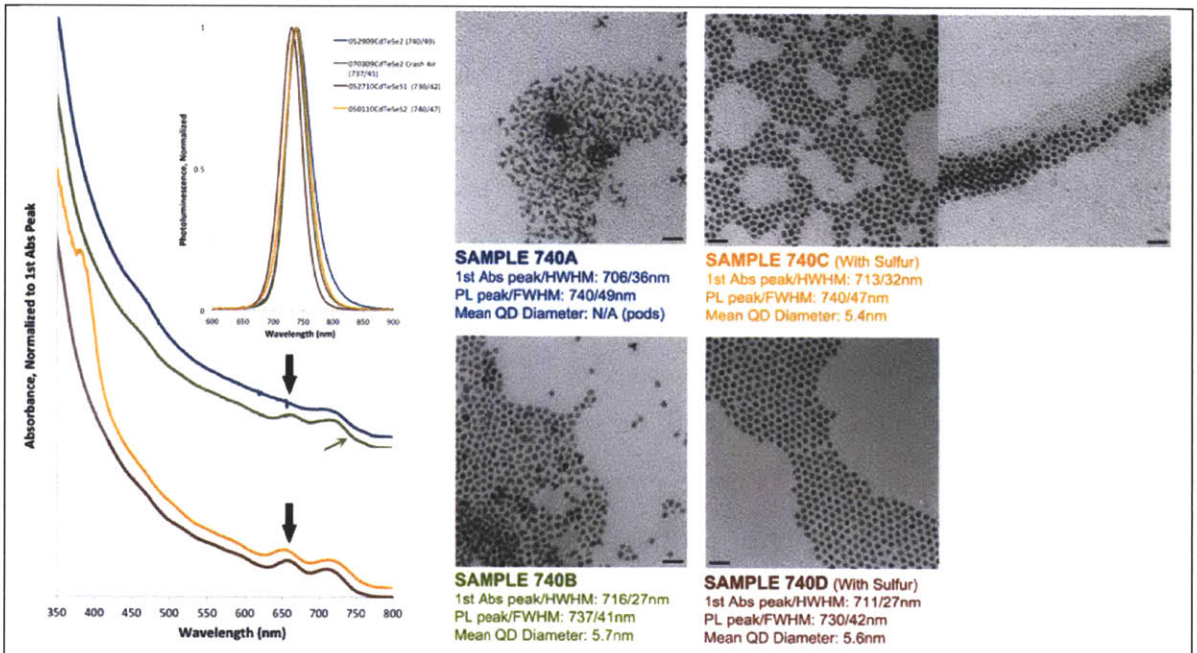

Figure 3.14: Morphological variations in QDs with fluorescence spectra of peak ~740nm and FWHM ~45nm. Sample 740A, similar to 680A in Figure 3.13, is an early sample and exhibits very poor nanocrystal morphology that does not reflect in its spectral profiles. Sample 740B has no MSNCs but retains minor shape problems in the major population; the small "kink" (pointed by the green arrow) and flattening / lengthening of the tail of its absorption curve is also seen in 740A and likely indicative of a subpopulation with a stronger type II character. This subpopulation may also appear as a small bump separate from the rest of the curve. Sample 740C has good major population uniformity but developed MSNCs during CdS overcoating, which have been intentionally retained for this TEM. As commonly observed for extraneous populations, the MSNCs form localized "colonies" on TEM samples that could be easily overlooked. The MSNCs shown here are relatively benign in that they are, size and spectrum wise, very distinct from the major population, appearing in the absorption profile as a "notch" at ~400nm that is far removed from the band edge, which is as well defined as Sample 740D that was synthesized with a similar protocol but free of MSNCs. Again, this figure shows that the fluorescence profile provides little clue to sample quality. The black arrows also point to the 2nd absorption band feature likely related to the composition gradient. Scale bar=20nm.

Absorption profiles are expectedly more variable in $CdTe_xSe_{1-x}$ QDs and reveal more information on the population(s) of nanocrystals present in the samples. Notably, they contain a pronounced 2nd absorption band at the immediate left of the 1st absorption peak, as seen in Figure 3.5 and Figure 3.7 and indicated by black arrows in Figure 3.13 and Figure 3.14. This 2nd absorption band, separated from the 1st absorption peak by the distance $d_{abs1\text{-}abs2}$ (Figure 3.15) was previously assigned to the lowest excitonic state associated with CdSe, X_{CdSe}, in quasi type II CdTe-CdSe QDs [38], although energetically it fails to match any of CdSe transition's states that are all positioned at lower wavelengths for the given sizes of nanocrystals; rather, the higher transition state of CdTe ($2S_{3/2}S_e$) should contribute to its oscillator strength. The tracking of this band's evolution with respect to the 1st absorption peak has been possible for the entire $CdS@CdTe_xSe_{1-x}$ QD series developed for this project, as pure CdTe emitter samples that emit at the shortest wavelengths have also consistently displayed this 2nd absorption band (Figure 3.5), as well as absorption features from higher transitions with details that are seldom achieved for CdTe QDs.

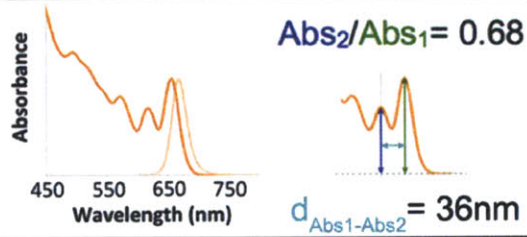

Figure 3.15: Definition of Abs_2/Abs_1 and $d_{abs1\text{-}abs2}$ in the absorption profile and its values in a CdTe QD sample (PL656/29 in Figure 3.4, Figure 3.5).

The ratio of the local maximum of the 2nd absorption band with respect to the 1st absorption peak's, Abs_2/Abs_1, is a potential indicator of the compositional gradient, provided that the QD populations under comparison are of similar size and synthesis conditions permit the fine features of the absorption profiles to be readable. Abs_2/Abs_1 can quantify the transition from type I to type II electronic structure, which is akin to creating an increasingly strong composition gradient that moves the

compositional structure of the nanocrystals from an alloy to a core-shell. The spatial separation of the electron and hole wavefunctions to form type II QDs—with the electrons being first delocalized between the core and a thin shell to form quasi-type II structures before being confined to a further thickened shell—are known to weaken oscillator strength at the band edge and lower its absorptivity value including Abs_1; the first literature on type II CdTe-CdSe QDs reported a band edge so diminished that the absorption profile becomes essentially a monotonically decreasing curve [83]. Reports on quasi type-II QDs, in which CdSe is grown in monolayer increments on type I CdTe emitters of known size and concentration, has provided visual information on how the type I-to-II transition is reflected in the absorption profile [38, 197, 88, 198]. The most evident change is the increasing prominence of the 2^{nd} absorption band with respect to the 1^{st} absorption peak, until the latter is no longer a local maximum but a shoulder. For the absorption curve to achieve monotonicity, however, loss of definition of these transition bands is needed, which is usually observed after more CdSe monolayers are added and appears to be overall more indicative of the synthetic conditions that control the "smoothness" of the curves from the start rather than the evolution of the band edge that indicates electron delocalization from the CdTe core.

Abs_2, which reflects the oscillator strength of higher energy transitions in CdTe in (CdS@)$CdTe_xSe_{1-x}$ QD absorption curves, also increases in magnitude as the nanocrystals grow in size as both charge carriers become more delocalized. The increasing trend of Abs_2/Abs_1 is therefore also present in the size series absorption profiles of single semiconductor QDs such as CdTe and CdSe QDs, which are devoid of composition gradients, and can be observed when synthesis is sufficiently well-paced for every size population to retain identifiable absorption features. Published size series of CdSe and CdTe QDs in which the increasing prominence of the 2^{nd} absorption band is evident can be found in [65,127,199]. One way to visually differentiate this category of Abs_2/Abs_1 increase—which has been reported for near

homogeneously alloyed $CdTe_{0.66}Se_{0.34}$QDs [13] as well—from the one due to type II carrier separation and diminished band edge (and Abs_1) is the spectral distance between Abs_1 and Abs_2, $d_{Abs1\text{-}Abs2}$, which decreases in the former case but increases in the latter. The decrease in $d_{Abs1\text{-}Abs2}$ can be attributed to the loss of quantum confinement and the collapse of distinct absorption bands. Hence, (CdS@)$CdTe_xSe_{1-x}$ QDs should be able to employ Abs_2/Abs_1 as a fast indicator of composition gradient, provided that the populations under comparison are similar enough in size.

The influence of synthesis conditions on the "smoothness" of absorption features and especially the actual values of Abs_2/Abs_1 is best appreciated by comparing the absorption profiles of similarly sized QDs of one and uniform composition (for example, the CdTe absorption profile in Figure 3.5 versus the same wavelength samples in [65, 199]). $d_{Abs1\text{-}Abs2}$ does not appear to change significantly with respect to synthesis conditions. Smoothening of absorption bands from their expected definition (based on the extent of quantum confinement as dictated by the nanocrystals' size and its relative magnitude to the material's Bohr radius) are, if not indicative of non-uniformity, likely associated with diminished coverage of the nanocrystals by surface ligands, the latter thus serving as a weaker dielectric that is less capable of confining charges or regulating interparticle surface atom exchanges. These atom exchanges make possible size focusing in single material QDs but are likely to increase the fluorescence spread of alloyed QDs, as previously discussed.

Optimizing the synthetic conditions for this project has, indeed, suppressed smoothing of absorption profiles and retained well-defined and easily distinguishable 1st and 2nd absorption bands for (CdS@)$CdTe_xSe_{1-x}$ QDs, even those fluorescing at long wavelengths. Thus Abs_2/Abs_1 can be used as a qualitative indicator of the composition gradient. The gradual increase of Abs_2/Abs_1 in (CdS@)$CdTe_xSe_{1-x}$ QDs begins from pure CdTe emitters synthesized for lower wavelengths and $d_{Abs1\text{-}Abs2}$, as the "gap" between Abs_1 and Abs_2, widens at the same time, suggestive of an

increasing type II character in the QDs (Figure 3.16). As previously mentioned, this is expected as the protocols for this QD series supply a consistent amount of tellurium and only at the start of synthesis for alloying, thus the extensions in fluorescent wavelength are largely realized by the addition of selenium and/or sulfur with only minor increases in nanocrystal size.

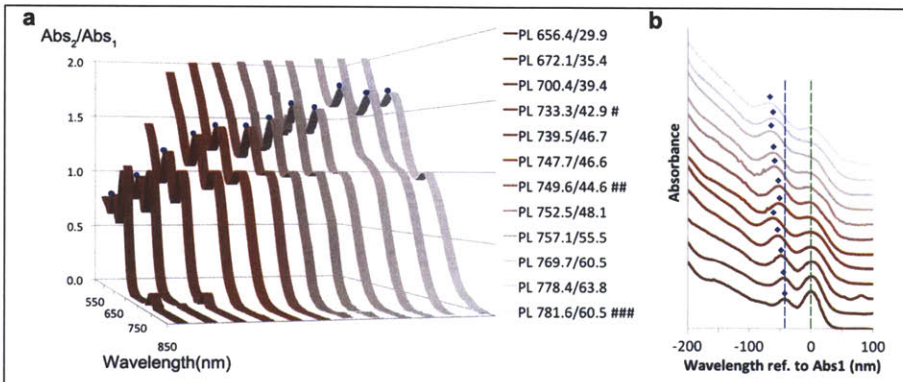

Figure 3.16: Evolution of Abs_2/Abs_1 and $d_{abs1\text{-}abs2}$ in CdS@$CdTe_xSe_{1-x}$ QDs. a) Abs_2/Abs_1 = Abs_2 after normalizing Abs_1 value to 1. Blue dots indicate the position of Abs_2 and highlight the increasing Abs_2/Abs_1 trend as fluorescent wavelength increases. The increase is not monotonic, given that the samples are not time series of a single synthesis but rather the product of individually tailored ones, which may differ in their CdTe-CdSe-CdS composition gradients. The overall size increase of this QD series, though minor (all sizes fell between 5.0-6.1nm; Figure 3.6), is thus also non-monotonic. b) Aligned *Abs1* plot, using green and blue dashed lines as visual references, shows that $d_{abs1\text{-}abs2}$ follows a trend that echoes that of Abs_2/Abs_1 shown in a). The increase in $d_{abs1\text{-}abs2}$ suggests steepening of the composition gradient and type II character as fluorescent wavelength increases, which agrees with the observation of falling QY as shown in Figure 3.6. While homogenous alloying is very unlikely, how the compositional structure of these QDs compares to true type II CdTe-CdSe QDs' (i.e. in which the composition gradient approaches infinity) cannot be deduced from this plot alone.

Dedicated experiments on carrier lifetimes will be needed to scientifically establish a connection between Abs_2/Abs_1, $d_{Abs1\text{-}Abs2}$ and the composition gradient, but availability of such an indicator will simplify the quality control process of (CdS@)$CdTe_xSe_{1-x}$ QDs, by 1) offering guidelines that can help create reference absorption profiles for QDs of

this alloy system and 2) circumventing the need to collect multiple aliquots during synthesis to obtain composition gradient information that is so vital to optimizing the optical properties of these QDs.

Over the course of the project, improved uniformity of (CdS@)$CdTe_xSe_{1-x}$ QDs has coincided with a drift towards higher Abs_2/Abs_1 and larger $d_{Abs1\text{-}Abs2}$ for a given fluorescence peak wavelength (Figure 3.17). If the relationship between Abs_2/Abs_1, $d_{abs1\text{-}abs2}$ and compositional gradient were true, then the nanocrystals have also been gaining a stronger type II character but notably sans an increase in fluorescence peak FWHM. This may be due to a steeper CdTe-CdSe gradient favoring a reduced statistical variation in composition among the QDs—via the formation of CdTe onlu nucleates, for example—the latter canceling out the widening of the fluorescence spectra. Sulfur incorporation in CdS@$CdTe_xSe_{1-x}$ QDs may further influence the composition gradient.

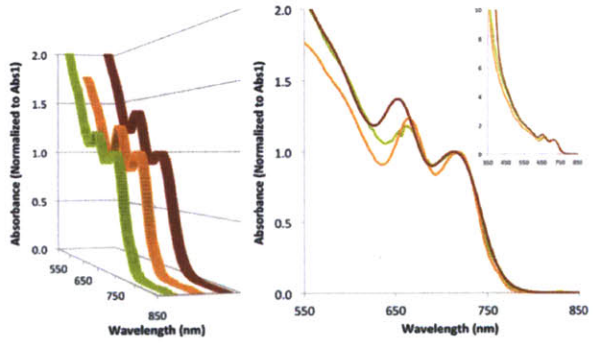

Figure 3.17: Increase in Abs_2/Abs_1 and $d_{abs1\text{-}abs2}$ as (CdS@)$CdTe_xSe_{1-x}$ QDs synthesized for this project improved in morphology and uniformity. All absorption spectra are normalized to the value of Abs_1. **Green**: before 98% HDA purification, see SAMPLE740B (PL737/41) in Figure 3.14 for TEM. **Orange**: PL 737/37** $CdTe_xSe_{1-x}$ QDs; TEM in Figure 3.4. **Red**: CdS@$CdTe_xSe_{1-x}$, TEM seen in Figure 3.6 as PL740/47.

On a last note, data cumulated on 2-pot overcoating has suggested that in order for efficient overcoating to proceed, the ligand condition (likely the dominance of Cd-OPA polymer) that retains the double absorption peak/band feature is to be reversed. When $CdTe_xSe_{1-x}$ emitters lack sulfur protection, the loss of Cd-OPA not only

smoothens their absorption features but also instigates a rapid increase in fluorescence peak FWHM, which can be symmetric or one sided, as well as a loss in quantum yield. Thus an optimized overcoating process may be, from the practical perspective, one that efficiently "switches" the protection mode of $CdTe_xSe_{1-x}$ emitters from organic ligand to inorganic sulfide coverage. The preparation of $CdS@CdTe_xSe_{1-x}$ may accomplish just that, by starting this ligand-to-sulfide exchange process while the $CdTe_xSe_{1-x}$ QDs are well-equilibrated with their native growth solution. The resulting CdS overcoat, even if it may not be thick enough to offer full oxidation protection, is sufficient to protect the QDs through flocculation, in which the QDs must shed their excess of Cd-OPA, and through the degassing / temperature ramping that begin a second overcoating process.

3.7 Water Solubilization & Functionalization

Readers interested in water solubilization of QDs are invited to consult Liu et al., Choi et al. [36,37,106] and their references on the different techniques currently available, the strengths of each and its disadvantages. The method by which hydrophobic nanocrystals are made water-soluble post-synthesis or overcoat determines the size and charge distribution; unless further modifications are done, these parameters will also decide their fate *in vivo*. Zwitterionic (thus neutral overall), small (hydrodynamic diameter <5.5nm) probes evades adsorption by serum proteins and allows fast renal clearance with minimal residual accumulation within the animal, while probes that are charged, larger in size or both tend to collect for days to years in different organs including, mainly, the liver and the spleen. For these probes with longer *in vivo* retention times, their time in blood circulation—which is equal to the time they are effective as vascular probes—can nonetheless be modulated via neutralization of charged surface groups (such as carboxylates or amines) and size increase to slow

their leakage into tissues (ex. through fenestrations along the endothelium). This can be done by coupling to the probes high molecular weight methoxy-terminated poly(ethylene glycol) (PEG), which also shields the charged functional groups. The effect of PEG molecular weight on *in vivo* uptake by different organs is further detailed in Choi et al. [36,37].

Water solubilization of CdS@$CdTe_xSe_{1-x}$ QDs for this project has been performed via polymer encapsulation, in which an amphiphilic polymer is adsorbed on the nanocrystals' organic surface ligands from synthesis / overcoating to achieve hydrophilicity. Compared to ligand exchange, in which the new ligands displace the original ligands, polymer encapsulation yields products that are readily derivatizable and poses less risk of compromising their quantum yields, but at the cost of yielding hydrodynamic diameters larger than allowable for renal clearance even before pegylation [147]. Slower clearance is not a concern for the purpose of this project as the imaging probes are prepared for non-clinical imaging experiments on animal models, which actually benefit from relatively long fluorophore circulation times. In fact, commercial cell labeling and *in vivo* non-targeted (vascular) NIR QD imaging probes (Qtracker series, Invitrogen, Carlsbad, CA) also employ the amphiphilic polymer approach as detailed in Wu et al. [210] and Ballou et al. [18]. The amphiphilic polymer is 40%octylamine-poly(acrylic acid) (the structure is illustrated in Figure 3.1). A cellular probe is made by adsorbing cell penetrating peptides onto the water solubilized QDs, which has been replicated in this project as illustrated in Figure 3.1. For vascular probes, coupling of the amphiphilic polymer's carboxylate groups to a 5000Da methoxy-terminated poly(ethylene glycol) (PEG) extends the *in vivo* circulation half-life of the probes to 70 minutes, which is sufficient for imaging [18].

The 40%octylamine-poly(acrylic acid) polymer construct was originally intended for the (CdS@)$CdTe_xSe_{1-x}$ probes and was, in fact, used in the earliest biological experiments (Figure 3.1 and Figure 3.2). However, the EDC coupling procedure for

making the amphiphilic polymer could not be replicated upon switching to a new batch of poly(acrylic acid) as starting chemical; the yield was poor and the product had difficulty dissolving in chloroform, which was the first step of the encapsulation process. Instead, the polymer had to be synthesized using the Reversible Addition-Fragmentation Chain Transfer (RAFT) method [34]. Aggregation and low yield remained significant problems, however, when encapsulation of (CdS@)$CdTe_xSe_{1-x}$ QDs was attempted with RAFT-synthesized 50%octylamine-poly(acrylic acid). Attempts to water solubilize the QDs via ligand exchange using the recently reported imidazole-PEG construct (50% Imidazole monomer + 50% methoxy-PEG11 or methoxy-PEG16 monomer) [106] were also met with similar issues.

These setbacks were at first suspected to be due to the QDs' phosphonate network surface ligands rendering them "unworkable" even after rigorous flocculations (section 3.5.3.1). But the problems were resolved and without additional processing required when poly(maleic anhydride alt-1-tetradecene) (M_w~9000; M_n~7300) [136] was employed as amphiphilic polymer for encapsulation. Once hydrated, the polymer differs from 40%octylamine-poly(acrylic acid) in that its intercalating, hydrophobic alkyl chains are longer (14 carbon in length versus 8) and that it lacks the nitrogen atom that connects these chain to the hydrophilic, carboxylate-rich backbone. Commercially available version of the polymer, which was used for experiments in this project, has been discontinued but methods of producing the polymer with various alkene chain lengths via radical polymerization / RAFT has been published [110,183]. It should be noted that the octadecene version of the same copolymer, which is also sold commercially, causes significant aggregation and is not suitable for water solubilization of the QDs.

The next subsections will describe the protocol for encapsulating CdS@$CdTe_xSe_{1-x}$ QDs with poly(maleic anhydride alt-1-tetradecene) for water solubilization and its related data on hydrodynamic size and stability.

3.7.1 Water Solubilization of $CdS@CdTe_xSe_{1-x}$ QDs with Poly(maleic anhydride alt-1-tetradecene) Encapsulation

Poly(maleic anhydride alt-1-tetradecene) M_w~9000, high purity bis(hexylmethylene) triamine, anhydrous chloroform stabilized with ethanol is purchased from Sigma Aldrich (St Louis, LA). Deionized water, reagent grade, is from Ricca Chemical Company (Arlington TX). Both 0.5x Tris-borate-EDTA buffer and sodium borate buffer have pH ~ 9.0. A notable difference between this preliminary protocol and the published version [136] is the omission of the sonication step because aggregation never occurred. The data to be described in section 3.7.3 was generated following this protocol.

1. Make stock solutions of poly(maleic anhydride alt-1-tetradecene) ("polymer") and bis(hexylmethylene) triamine ("crosslinker" in anhydrous chloroform, each at the concentration of 8mg/mL (or 0.125mL/mg). These solutions are stored in 4°C until use.

2. According to Pelligrino et al. [136], 100 monomer units should be introduced to cover each $1nm^2$ of nanocrystal surface area. Assuming the QDs are ~6nm in diameter and the average number of monomer units per poly(maleic anhydride alt-1-tetradecene) is 25, 3.3mg polymer (or 0.4mL of its chloroform-based stock solution) is needed for water solubilizing 1.0nmol of $CdS@CdTe_xSe_{1-x}$ QDs.

3. Prepare a 20mL septum vial with continuous N_2 supply and in a water bath, the latter to suppress evaporative cooling of the solution later. Add 0.4mL polymer stock solution into the vial. Immediately dry 1.0nmol of QDs (stored in

N_2, hexane post-flocculation) in a separate vial, re-suspend them in 0.1mL anhydrous chloroform and add this solution dropwise into the 0.4mL polymer stock solution while stirring at low speed (~150rpm).

4. Let stir at low speed (~150rpm) for 1 hour—the slow speed prevents splashing and keeps all solution at the bottom of the vial. The N_2 supply should dry most of the solution by the end of the 1 hour.

5. Start vacuum and dry solution for ~15minutes or until base pressure is reached. Switch back to N_2.

6. Re-suspend the QDs in 0.47mL anhydrous chloroform, then add 30uL of the crosslinker stock solution (i.e. 0.24mg crosslinker, or 10 /nm^2 QD surface as specified by Pelligrino et al. [136]) and let stir for 15minutes. This step can be performed in air, but the septum cap should remain on to slow down evaporation.

7. Start vacuum and dry solution for ~15minutes or until base pressure is reached. Release to air.

8. Stirring at ~600rpm, add 0.5mL 0.5x Tris-EDTA-borate buffer and stir for 5 minutes. The QDs should solubilize readily without apparent cloudiness. Fluorescence loss should also be minimal.

9. Increase 0.5x Tris-EDTA-borate buffer volume to 4mL and dialyze 5x using 50k MWCO, 4mL centrifugal filtering devices and a spin speed of 7000rpm (4 minutes are usually sufficient to filter the solution each round)—if EDC coupling (for pegylation) is needed later, switch to 50mM sodium borate during dialysis.

10. Re-suspend in 0.5mL 50mM sodium borate buffer and filter with 0.2um PES filter. The solution, which should remain clear and fluorescent, is ready for storage. The products are analyzed for size with dynamic light scattering (DLS). Any remaining small aggregates should be removed by gel filtration chromatography (GFC) prior to pegylation.

Subsequent experiments have shown that the polymer encapsulation step (step 4) can be shortened to 30 minutes and also, the crosslinking step is not needed to stabilize the polymer cap after water solubilization. Stability test of water-solubilized and PEGylated products (Figure 3.19 in section 3.7.3) was performed on QDs prepared with two major changes in the protocol. The crosslinking step was removed altogether as the introduction of amines may destabilize the ligand-nanocrystal interface, with the weaker-binding but abundant amines replacing the strongly bound but few in quantity phosphonates. In the future, long-term stability of the QDs with and without the crosslinker should be compared.

3.7.2 Coupling of methoxy-PEG on CdS@$CdTe_xSe_{1-x}$ QDs Water Solubilized with Poly(maleic anhydride alt-1-tetradecene)

The following preliminary protocol describes the PEGylation of 0.5nmol CdS@$CdTe_xSe_{1-x}$ QDs with 5000Da methoxyPEG, based on the guidelines published by Ballou et al. [18]. While DLS data suggest promising results in coupling efficacy (Figure 3.18 in section 3.7.3), fluorescence instability that is believed to be caused by insufficient overcoating has prevented the products from proceeding to serum protein adsorption or *in vivo* experiments. PEGylation is performed by a simple EDC coupling of amine-terminated methoxyPEGs to carboxylates formed upon hydration of maleic anhydrides on the amphiphilic polymer backbone. The solvent is 50mM

sodium borate buffer, free of phosphates and Tris that comprise EDC coupling efficiency. Amine-terminated methoxyPEGs (abbreviated as NH_2-mPEG in the protocol) of molecular weights 750Da and 5000Da are purchased from Creative PEG works (Winston Salem, NC); EDC (*N*-Ethyl-*N*′-(3-dimethylaminopropyl) carbodiimide hydrochloride) ≥98% is from Fluka (Sigma Aldrich, St Louis, LA) and stored in 4°C until the time of use. Deionized water, reagent grade, is from Ricca Chemical Company (Arlington TX).

1. Prepare borate buffer solution of NH_2-mPEG: 0.1mL/mg for NH_2-mPEG 750Da, 0.02mL/mg for NH_2-mPEG 5000Da.

2. In a vial, introduce 0.5nmol of water solubilized CdS@$CdTe_xSe_{1-x}$ stored in 50mM sodium borate buffer. Add in NH_2-mPEG such that [NH_2-mPEG]/[QD] = 2kx for NH_2-mPEG 750Da and = 6kx for NH_2-mPEG 5000Da, which translate to 75uL and 300uL of their stock solution respectively. Finally, introduce sufficient volumes (371uL; 146uL) of 50mM sodium borate buffer so that the total volume of each reaction is 500uL. Begin stirring.

3. Prepare EDC solution in DiH_2O (pH~6) for immediate use, at a concentration of 0.1mL/mg. Add 0.14mg (14uL of solution) into the stirring contents of the vial. Let stir for 2 hrs.

4. Increase 50mM sodium borate buffer volume to 4mL and dialyze 2x using 50k MWCO, 4mL centrifugal filtering devices. The solution should remain clear and fluorescent throughout. The products can then undergo DLS size analysis and gel filtration chromatography (GFC) to check for and remove any small aggregates. Upon confirmation of satisfactory physical and optical properties, the probes can proceed to evaluation for serum protein adsorption. If the result is negative, the products are ready for *in vivo* use.

3.7.3 Data from Water Solubilization and PEGylation of CdS@$CdTe_xSe_{1-x}$ QDs

GFC and DLS data collected from water-solubilized CdS@$CdTe_xSe_{1-x}$ QDs, with or without pegylation, is illustrated in Figure 3.18. DLS analysis reported the hydrodynamic size of the sample (PL700/39 in Figure 3.6 and Figure 3.7; core diameter = 5.5nm by TEM) to be 10.5nm and 16.6nm after amphiphilic polymer encapsulation and encapsulation+NH_2-mPEG 5000Da coupling, respectively. For comparison, commercial Qdot565 (4.6nm inorganic crystal; Invitrogen, Carlsbad, CA) has a hydrodynamic radius 14.2nm after 40% octylamine-poly(acrylic acid) encapsulation [145], while Qdot655 (9nm inorganic crystal; also from Invitrogen) has a reported hydrodynamic radius value of 22.6nm after the attachment of NH_2-mPEG 5000kDa on the same amphiphilic polymer cap [17]. Whether the relatively small hydrodynamic radius, especially after water solubilization, is due to poly(maleic anhydride alt-1-tetradecene) being more compact after hydration in the 50mM sodium borate buffer or being at lower concentrations is yet to be determined, as is whether the amount of PEG coupled on the surface is sufficient to shield all surface charges that would lead to serum protein adsorption and shorter circulation time *in vivo*. Robust *in vivo* vascular retention may require further increase in probe size to match the values of the commercial products, either by increasing the coverage of the polymer, the PEG or both or switching to an even higher molecular weight NH_2-methoxyPEG. Reaction yield for both steps has shown a vast improvement over early samples (Figure 3.1 and Figure 3.2) (>95% compared to <2%), with no appreciable loss as aggregates in all cleaning steps following water solubilization and PEGylation.

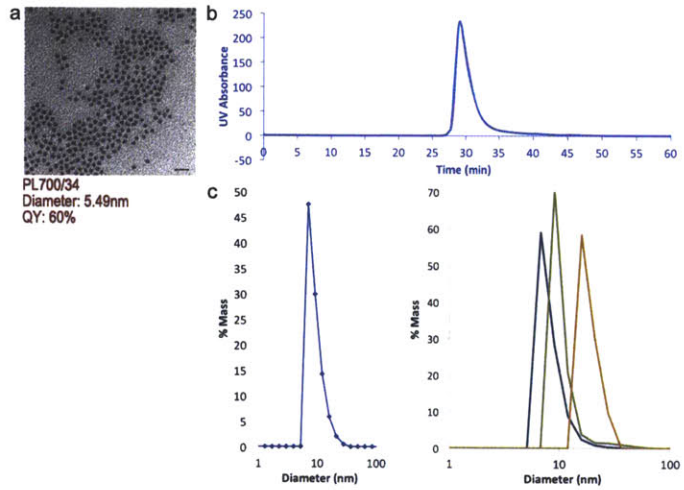

Figure 3.18: GFC and DLS data of water solubilized, PEGylated CdS@$CdTe_xSe_{1-x}$ QDs. a) TEM of sample **PL700/39** before water solubilization. Scale bar=20nm. b) GFC data after encapsulation with poly(maleic anhydride alt-1-tetradecene); again, UV absorption was used to detect the presence of QDs exiting the column. Unlike early samples (Figure 3.1), QDs exited the size exclusion column at close to one time point, suggesting the absence of aggregates that would have left the column earlier. c) DLS data also shows a uniform size peak for the water solubilized QDs (left); after PEGylation (right), the size of the QDs increases according to the molecular weight of the NH_2-mPEG coupled to the amphiphilic polymer cap. **Blue**=water solubilized QDs without PEG; **Green**=water solubilized QDs coupled with NH_2-mPEG 750Da; **Brown**=water solubilized QDs coupled with NH_2-mPEG 5000Da.

Water-solubilized QDs, with or without PEGylation, suffered significant fluorescence loss over a period of one day (Figure 3.19). As no aggregation or precipitation from water was observed and the quantum yield of the pre-water solubilized sample also fell over time (albeit at a much slower pace), it was determined that the oxidation protection on these CdS@$CdTe_xSe_{1-x}$ QDs was incomplete. Experimental focus has therefore returned to determining the proper methods for overcoating and stabilizing the inorganic nanocrystal within each probe.

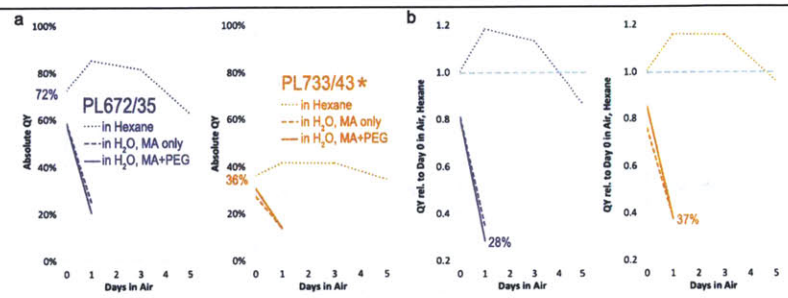

Figure 3.19: Comparative stability of two CdS@$CdTe_xSe_{1-x}$ QDs samples before and after water solubilization using poly(maleic anhydride alt-1-tetradecene) and with or without PEGylation with 5000Da methoxy-poly(ethylene glycol). All samples were pre-diluted to concentrations appropriate for spectroscopic measurements on Day 0 and stored in air for the duration of the experiment. a) Absolute QY values. While the hexanes samples were quite stable and their QY did not fall below their initial value until 5 days later, once the QDs were solubilized in water the drop of QY occurred in 1 day, with PEGylation making a relatively minor impact. The longer wavelength sample (**PL733/43**) showed a smaller drop in absolute QY despite starting at a lower value; its relative QY drop compared to pre-water solubilization was also smaller, which was better observed in b), compared to the shorter wavelength sample (**PL672/35**). This smaller relative QY drop, which translates to better stability, is likely due to the $CdTe_xSe_{1-x}$ emitters being more Se-rich and therefore exhibited better tolerance against oxidation.

3.8 Future Work for Developing *In vivo* NIR imaging probes based on $CdTe_xSe_{1-x}$ QDs

The work described in this chapter has emphasized on the creation of morphologically and spectrally uniform $CdTe_xSe_{1-x}$ nanocrystals, using synthesis protocols that are developed with reproducibility as a main criterion. Uniformity and reproducibility are difficult-to-convey parameters in literature but are essential for quality control and development of application-ready products. They elucidate trends that are helpful for protocol optimization and ensure that these trends will remain

true in the long run, even after the protocols change hands and the lots of starting chemicals have run out in the companies that manufacture them. In the case of $CdTe_xSe_{1-x}$ QDs' application as fluorophores for *in vivo* multiplexed imaging probes, the QDs must be sufficiently consistent in their physical and optical properties such that their fluorescence signal can be trusted to depend only upon the biological information to be gathered. This implies consistent wavelengths, quantum yield, physical size, surface charge and concentrations of functional moieties, and the ability to re-create the probes in sufficient qualities on demand and with a reasonable shelf life such that the timing of the experiments need only to suit the application itself (such as the time points of imaging studies) and not when the probes will suffer a loss in quality.

The $CdTe_xSe_{1-x}$ QDs developed for this project has achieved morphological uniformity, which has been proven to be key to their acquiring a predictable behavior during overcoating, water solubilization and post-synthesis processing in general. Purity of starting chemicals and tight process control are critical, and the nanocrystals gain workability only after a strict protocol for flocculation has been developed and followed consistently. Tellurium composition *x* in the QDs approaches the ratio of tellurium and selenium precursors supplied during synthesis, which is highly useful for predicting the spectral properties of the products from synthesis, and sulfur has been incorporated into the nanocrystals in amounts significant enough to form a preliminary overcoat. Water solubilization has also been successful with $CdS@CdTe_xSe_{1-x}$ with near unity yields, as well as PEGylation that is needed to make vascular imaging probes and adsorption of the cell penetrating peptide PEP-1 to make cellular probes. The main shortcoming of these hydrophilic CdS@ $CdS@CdTe_xSe_{1-x}$ QDs is their current lack of long-term fluorescent stability in water, which is believed to be due to insufficient CdS incorporation and possibly aggravated by too gentle of a $CdTe_xSe_{1-x}$ emitter / CdS overcoat composition gradient such that sulfurization at the nanocrystal surface is not complete, resulting in premature oxidative degradation

especially in an aqueous environment. The 1-pot overcoating approach is likely the root cause of the problem by carrying the chemical "history" of nucleation and growth, which includes substantial amounts of strongly binding acids in the form of Cd-OPA and can equalize the incorporation of emitter CdTe+CdSe and CdS as it does to CdTe and CdSe. Nonetheless, the 1-pot approach is also essential for stabilizing the $CdTe_xSe_{1-x}$ QDs enough such that they can undergor a second overcoating procedure, which can then be optimized solely for overcoating—by introducing ZnS, for example, for better carrier confinement, higher quantum yield and a lesser type II character compared to using CdS. It also encourages the exhaustion of Te and Se precursors.

The timing of sulfur entry during the 1-pot process is worthy of more investigation. The difference in stability between samples PL733/43 and PL782/61 in the $CdS@CdTe_xSe_{1-x}$ series, for example, with the latter being more stable in air, is likely due to the timing, temperature and quantity of not only the sulfur but also the Cd-OPA being introduced, which modulate the emitter / overcoat gradient. Higher precursor concentrations are not always more effective; too high of concentrations causes CdS nucleation as seen in sample PL700/40; high concentrations of phosphonates in Cd-OPA also hinders monomer incorporation. Avoiding too early of an incorporation of sulfur is also important as it can shorten the fluorescence wavelength without any stability benefit.

Experiments on the second overcoat attempted for this project have so far focused on using purified chemicals, with the intention of ensuring reproducibility of the entire probe development process. It is nonetheless possible that purity of starting chemicals does not require as strict a control during this second overcoating step to achieve the needed reproducibility; thus well-known overcoating procedures such as SILAR [100] and the dimethyl cadmium / bis(trimethylsilyl) method [72] may be tested again for both efficacy and reproducibility.

The water solubilization protocol as described in section 3.7 is preliminary and further optimization in, for example, the duration of the poly(maleic anhydride alt-1-tetradecene) polymer adsorption step, may improve the stability of the products. As previously mentioned, the effect and necessity of the bis(hexylmethylene) triamine crosslinking step is yet to be confirmed.

Last but not least, if future applications can specify a small number of fluorescent wavelengths of interest, it may be worth optimizing the synthesis protocol for those few selected wavelengths to minimize their type II character as much as possible and without re-introducing uniformity problems. As the (CdS@)$CdTe_xSe_{1-x}$ QDs are developed as a wavelength series in this project, optimizing the protocol for each wavelength is too time-consuming to be practical and the protocols have been designed such that tuning the fluorescent wavelength does not require significant changes in the timing and quantity of precursor entry (especially Cd-OPA)'s. The cost of this approach, which is implemented by holding constant the timing and quantity of tellurium entry, is the augmentation of type II character in the QDs fluorescing at longer wavelengths. While the absorption spectra should offer clues to the composition gradient, measurement of carrier lifetimes is ultimately the most (and only) reliable way of gauging its amplitude. Minimizing the type II character should improve quantum yield and produce sharper fluorescence profiles.

4 Visual Presentation and Quantitative Morphometry of the Murine Calvarial Bone Marrow using *In vivo* Multiplexed Imaging

This chapter returns to the motivation of the thesis, which is to expand our knowledge of the bone marrow (BM) microenvironment via *in vivo* multimodal, multiplexed microscopy. The cause for developing a protocol for quantitative characterization of the BM's morphology, or morphometry, is straightforward: to provide a simple, systematic method to describe co-localization (or lack thereof) data, which is spatial / topographical in nature and often difficult to convey due to the intricate tissue architecture of the BM. Developing a well-defined visual presentation method for 3-D *in vivo* multiplexed images serves two purposes: 1) condenses the visual information such that it can be communicated with ease; and 2) prepare the imaging stacks for quantitative analysis. While the NIR $CdTe_xSe_{1-x}$ QDs developed for this project have yet to be used in their intended biological applications due to their fluorescence instability, commercial QD vascular probes fluorescing in early NIR (non-targeted Qtracker655, Invitrogen, Carlsbad, CA) have aided tremendously in the development of these methods, an example of the analysis data has already been shown in Figure 1.2 f. These analyses have helped to unveil the complex associations between BM structure and its function, and describe the activities of HSPCs, immune cells and cancer cells in a systemic manner that should more efficiently point to the mechanisms underlying the physiological and pathological processes in which these cells are involved.

The protocol developed for visual presentation and quantitative morphometry of the BM from *in vivo* multiplexed imaging data to be presented here has been published [107,108]. This chapter will describe in better detail the purpose of each step as well as its outcome; the illustrations also showcase NIR QDs vascular probes at work.

There are four major steps in this protocol, with "V" denoting steps that aim to improve visual presentation and "M" for steps intended for morphological analysis, which at present are mostly distance measurements that describe the geometrical relationships between the endosteum, osteoblasts and blood vessels:

V1: Calvarial tilt correction
V2: Signal strength equalization as a function of depth
M1: Segmentation (i.e., binarization of images)
M2: Euclidean distance measurement

Unless otherwise specified, all images in this chapter were captured in two-photon mode from Col2.3 –GFP mice with C57BL/6 background. 35uL of Qtracker655, 2uM stock solution (Invitrogen, Carlsbad, CA) was diluted with 115.5uL 1x PBS + 3.5uL 10x PBS and injected retro-orbitally into the anesthetized animal immediately before imaging. Bone signal was the second harmonic generation from its collagen and collected through a 400-500nm band-pass filter. Osteoblasts were detected by its EGFP fluorescence that was collected through a 500-590nm band-pass filter. Qtracker655's red fluorescence was collected through a 625-675nm band-pass filter. A titanium: sapphire femtosecond pulse laser, mode locked at 920nm, was used to excite all three channels. The planes and axis of imaging are defined as shown in Figure 1.2 c, with X-Y as the imaging plane and Z quantifying imaging depth.

4.1 Visual Presentation of the BM

The BM does not have a well-defined tissue layer structure that is often observed in the biopsy of other organs (for example, skin: epidermis / basement membrane / dermis / hypodermis), which makes its morphology relatively difficult to describe

verbally or on a 2-D visual platform. The complexity of BM microarchitecture and the well-accepted notion that these physical structures influence the BM's role as a niche—as evidenced by the naming of candidate HSPC niches as osteoblastic niche, endosteal niche and vascular niche etc. [122]—necessitates the need to present the 3-D character of the BM in an accurate, consistent and easily readable manner.

Pre-requisite for good visualization is that the original *in vivo* imaging data must be robust, with strong signal-to-noise ratio and the fluorescence signal from each labeled biological entity being largely confined to within its own optical channel, i.e., there is minimal spectral overlapping between the fluorophores (Figure 4.1). Two-photon microscopy using 1 um Z-stepping created 3-D image stacks that captured with clarity the boundaries of small features, especially the capillary network enmeshed between the endosteum and the osteoblasts (see Figure 1.2 b). Qtracker655, as the only fluorescent probe introduced into the animal subjects, was also instrumental in resolving these small capillaries. It did not exhibit any leakage into the intervascular space, which would have blurred the vascular boundaries and is often observed when smaller-sized organic vascular dyes (such as Evans blue, also known as T-1824, which circulates as a dye-albumin complex; albumin's effective radius is ~7.5nm [121,214]) are used. Also, since the blood flow rate in these ultra-small vessels (<1 um diameter) was unknown and the resolution required for analysis prolonged imaging times, the QDs' resistance to photobleaching also ensured a more comprehensive view of the BM vasculature.

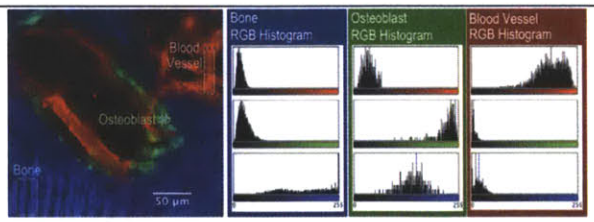

Figure 4.1: Check for fluorescence signal confinement within its assigned optical channels in *in vivo* BM images. The white boxes in the *in vivo* BM image on the left demarcate sample regions of the bone, the osteoblasts and the blood vessels and their corresponding histograms are shown on the right. Signals from the bone and the vasculature were well confined within their optical channels (blue and red, respectively), while osteoblast fluorescence (green) extended into the blue channel. This "leakage" causes the osteoblasts to carry a cyan hue in the image, and while the osteoblasts remain easily distinguishable from the bone by eye, it adds difficulty during segmentation (*step M1*) when the image analysis program must define the boundary between the osteoblasts and their adjacent bone. Also seen in this figure is the well-defined vasculature (red) after intravenous injection of Qtracker655, with capillaries of micron-diameter range showing clean boundaries that are required for proper segmentation. Scale bar=50um.

Methods developed for visual presentation of the BM must not create artifacts or eliminate structures. While image processing programs with impressive visualization and analytical capabilities have been developed (ex. [25]), many are written for specific tissue types to limit the computations required; "guidelines" incorporated in the software code that originate from the modeling of these tissue types can significantly compromise the outcome's accuracy when working on the imaging data from other tissues. Given our understanding of the BM anatomy is far from complete, there is insufficient *a priori* knowledge on BM morphology—on how the vascular network should align or how the osteoblasts should distribute, for example—to create a model for automating image visualization and analysis. Thus BM visualization and morphometry has been performed manually with the help of the open-source image processing software Image J [1].

Step *V1: Calvarial tilt correction* maximizes the area of BM cavity that can be viewed in every X-Y image, thus minimizing the number of images needed to convey the 3-D visual information of the cavity. It is accomplished by correcting the tilt of the calvarium that originates from both the anatomy of the animal and the angle of its placement on the stage during imaging. Because the boundaries of the cavities follow the curvature of the sandwiching bones, the practical outcome is also that the tissue thickness over each X-Y image is normalized for all points in that image, which translates to a uniform "illumination" over the area. Figure 4.2 illustrates the principles and outcome of step *V1*.

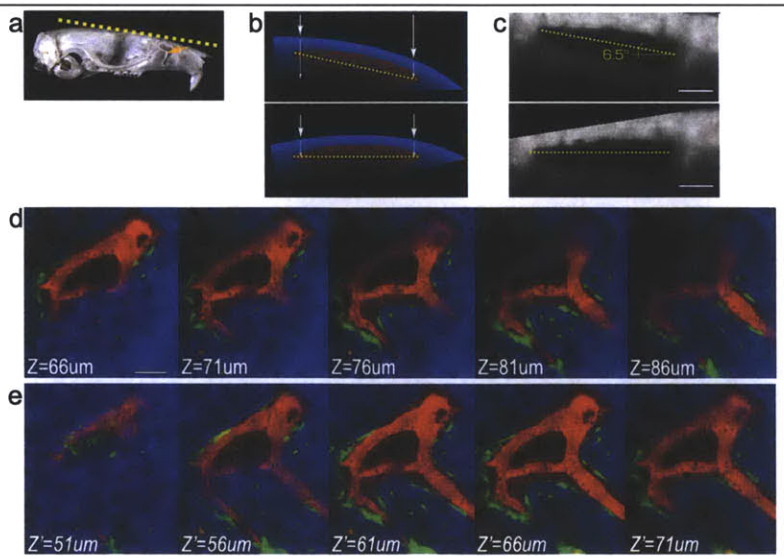

Figure 4.2: Visual presentation of the BM—step *V1*, calvarial tilt correction. a) A mouse skull with its natural tilt shown in a yellow dotted line. b) Illustration of the motivation of step *V1*. Blue presents the bone and red, the BM cavity space. An image stack is composed of optical sections, each a "slice" along the vertical (Z-axis) direction. Before tilt correction, every slice can only capture a small cross-sectional area of the cavity; the thickness of tissue to be crossed by photons (shown by white arrow and its length) also varies across the horizontal X-Y plane, resulting in uneven "illumination" from one side of the image to another. Rotating the image stack such that the tilt approaches zero in both the coronal and sagittal planes solves these problems. c) *In vivo* image of the bone channel only, re-sliced in the X-Z plane to show the tilt of the cavity before and after tilt correction. d) An *in vivo* multiplexed image stack showing the bone (blue), osteoblasts (green) and vasculature (red) of a BM cavity, pre-tilt correction. A span of 20um in depth is needed to visually convey the sinusoid that runs along the periphery of the cavity. e) The same image stack after tilt correction. A single image, *Z'*=66, is sufficient to visualize the entire sinusoid of interest, and the same span of 20um in depth is sufficient to show the cavity opening in the bone and is therefore enriched in visual information. Illumination is also more uniform in this image stack, which is especially evident when comparing the brightness of the lower right versus upper left corner of each image. Scale bar=50um.

Step *V2: Signal strength equalization as a function of depth* aims to recover the loss of signal in deep imaging planes due to absorption from overlying tissues. It is performed mathematically, based on the understanding that 1) intensity is presented

as greyscale values in the images and 2) intensity attenuation due to tissue absorption can be described as an exponential decay function, which corresponds to the Beer-Lambert's law:

$$\frac{I}{I_0} = e^{-\mu_a cz} \qquad (Eq.8)$$

in which *I* is light intensity, μ_a is the absorption (extinction) coefficient specified by the absorber, c is the absorber concentration, and *z*, the path length, in this case the thickness of tissue traversed by the photons or the imaging depth.

Once this decay function, as a function of *z*, is determined for a 3-D image stack, it can be normalized and its inverse applied to the stack to recover the lost signal. Calvarial tilt correction (step *V1*) is a pre-requisite as it uniformizes the tissue thickness, and hence the value of *z* for all pixels within each X-Y image plane, allowing the correction of each image by a single constant. It is important to note that this step does not increase the signal-to-noise ratio, only easing the viewing of features already present but are too dim to see by eye; moreover, for this method to work, the fluorophore supplying the signal must not photobleach at all for the duration of capturing the original image stack. Figure 4.3 explains in detail the principles and outcome of step *V2*.

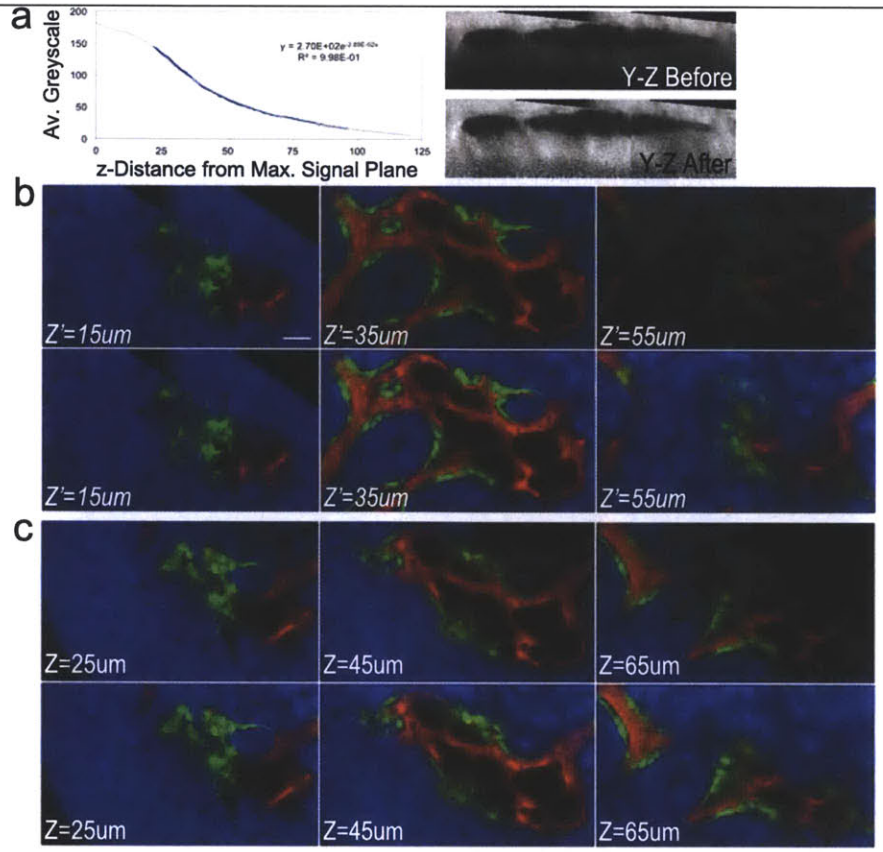

Figure 4.3: Visual presentation of the BM—step *V2*, signal strength equalization as a function of depth. a) Loss of fluorescence as a function of imaging depth *z* fits well to an exponential decay curve (light blue line placed over dark blue data), as seen in the plot of average greyscale intensity of each X-Y plane in the bone (blue) channel versus the plane's pixel distance away from the one with maximum signal intensity, set as z=0, which generally approximates the position of the bone surface. The decay curve is specific to the color channel as well as the image stack, and steeper in the blue compared to the green and red channels as expected from tissue optics. For signal equalization, the inverse of this exponential decay curve is mathematically applied to the image stack from which it was determined, with all greyscale values in each X-Y plane multiplied by one constant. The outcome is illustrated on the right, in which a Y-Z (vertically) re-sliced bone image shows an equalized fluorescence intensity as a function of *z*. b) Comparison of a tilt-corrected BM image stack in all 3 colors in the X-Y perspective, before (upper row) and after signal equalization (lower row). Tilt correction ensures that signal attenuation is uniform throughout each X-Y plane, which is pre-requisite for the one-constant-per- plane mathematical approach to amplify the signal strength of deeper planes. c) Signal strength equalization demonstrated with an image stack that is visually presented with its original calvarial tilt. The upper row shows the original image stack without tilt correction or signal equalization, the lower row, after signal equalization and then, re-introduction of the

calvarial tilt. In the original images stack, the "bright" lower left corner is showing features closer to the skull surface than the "dim" upper right corner with its thicker overlying tissue. After signal equalization, the "brightness" of the two corners becomes much more uniform, with the upper right corner signal being amplified significantly while the lower left corner stays relatively unchanged. What is clear from this visual orientation, in which the modified and unmodified pixels are positioned side by side, is that although signal equalization eases the observation of dim features, it does not improve the quality of the image—thus the upper right corner of the image, while bright, still looks "grainy" with its lower signal-to-noise ratio. Scale bar=50um.

4.2 Morphometry, or Quantitative Analysis of the BM Anatomy

The ability to perform quantitative morphometry goes hand in hand with robust visualization as it begins with segmentation (step *M1*), or definition of objects from their background. Segmentation creates the needed boundaries to become outlines or endpoints from which measurements can be made; for BM images, it has been performed by applying a threshold on each color channel individually and creating binarized images. Edge-finding algorithms are difficult to implement on BM imaging data due to the intricacy and irregularity of anatomical features, especially in the vascular channel. Algorithms that can help elucidate the structure of the vascular tree, such as those that predict connectivity based on ray tracing or local-unidirectional cylinder models, not only require manual inspection for accuracy [5] but may also assume unidirectional vessel morphology [152], which is prone to omit branching points that are widely and densely distributed in the BM vascular network in the form of loops and shunts.

As expected, deep tissue objects captured with low signal-to-noise ratio are most likely to suffer from poor segmentation fidelity. Thus quantitative measurements must often be limited to a shallower depth (as seen bracketed in Figure 1.2 a) compared to the maximum depth at which features are discernible by eye, especially after visual presentation steps *V1* and *V2* are implemented. It is important to visually check for accurate image binarization, which include removing unwanted noise pixels, confirming connectivity of small features such as capillaries and ensuring spatial specificity of anatomical features (i.e. no overlapping of physical structures) before proceeding to measurements (step *M2*).

Step M2 provides Euclidean distance measurements between different anatomical features in the BM. Euclidean distance is defined between points $P = (p_1, p_2, \ldots p_n)$ and $Q = (q_1, q_2, \ldots q_n)$ in a space of dimension n as follows:

$$\sqrt{\sum_{i=1}^{n}(p_i - q_i)^2} \qquad (Eq.9)$$

As full 3-D distance measurement is computationally intensive, distance measurements have been performed on the three Cartesian planes: X-Y, Y-Z and X-Z in 2D and the final measurement is the minimum of the three values for each Cartesian point.

ImageJ's built-in "Distance Mapping" function performs 2-D Euclidean distance measurements, by marking each pixel in the background with a greyscale value that equals the pixel distance from that point to the closest boundary of an object. Using the binarized vascular image stack (red channel) to define objects, for example, one obtains a greyscale map that describes the distance between every non-vascularized pixel in the image to its nearest vessel wall. Binarized image stacks of the other channels can then be applied as masks and identify the physical nature of these non-

vascularized points—the green channel specifies them as osteoblasts, for example. By combining the two pieces of image data and calculating the output's greyscale histogram, a distribution of distances between the osteoblasts and their nearest blood vessel is obtained. Illustration of this procedure is shown in Figure 4.4.

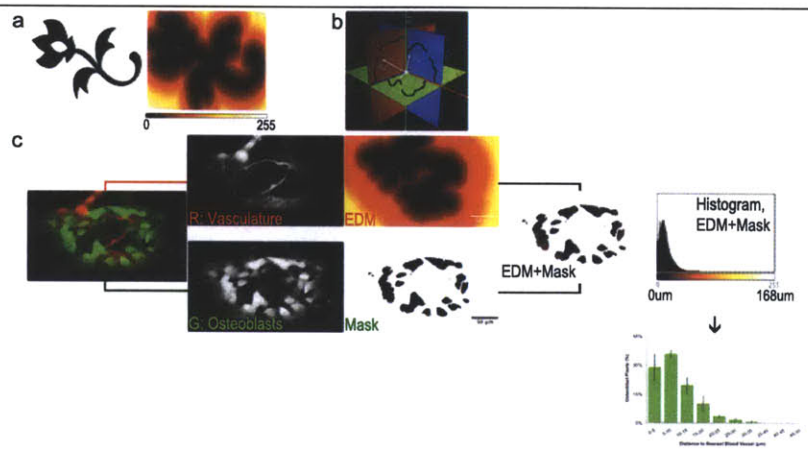

Figure 4.4: Quantitative morphometry of the BM—step *M2*, Euclidean distance measurement (EDM). a) Principle of EDM in 2-D. For a binarized black object on white background such as this flower, the "Distance Map" function in ImageJ assigns to each background pixel a greyscale value that represents the pixel distance it is away from the closest object pixel—in this case, the nearest edge pixel of the flower. The greyscale distance is re-colored using ImageJ's "Red-Hot" LUT as shown in the bar below. b) To expedite computation, 3-D EDM of every point is estimated by first performing 2-D EDM on the three cartesian planes (X-Y, Y-Z, X-Z) and then taking the minimum of the three distance values, d_{xy}, d_{yz}, and d_{xz}. c) The process flow of making distance measurements between two BM anatomical components, the vasculature and the osteoblasts. The original image stack (one image is shown here) is separated according to its R/G/B color channels, each of which is then segmented to create a binarized image stack. Afterwards, the binarized image stack created from the red (blood vessel) channel is used to create an EDM stack, in which every non-vascular pixel is assigned the greyscale value that corresponds to its pixel distance to the nearest vessel wall. When the binarized image stack from the green (osteoblast) channel is applied as a mask on the EDM stack, the EDM stack becomes "white-out" but for the non-vascular pixels that co-localize with the positions of osteoblasts—i.e. the pixels that are relevant to this measurement. ImageJ readily creates a histogram of this masked EDM stack, the data of which describes the distance between the osteoblasts and their nearest blood vessels after applying a scaling factor that calculates actual physical distances from pixel distances. This plot is identical to Figure 1.2 f.

Morphometry is not limited to distance measurements. Volumetric measurements—for example, vascularized volume fraction in the BM cavity—can be performed with

ease once the image stacks are successfully segmented, by counting the pixels occupied with blood vessels and comparing the value to the cavity pixel count that is known from the binarized image stack of the bone.

Methods described in this chapter, from visualization to quantitative analysis, is by no means restricted in application to images of the bone marrow. They should adapt well to *in vivo* multiplexed images of other tissue types, having no BM-specific criteria in their principles or implementation. Nonetheless, no matter the tissue type or the components within that are being observed or measured, the accuracy and significance of knowledge gained is ultimately limited by the quality of the original image stacks, defined by parameters such as signal-to-noise ratio, specificity of fluorescence contrast to its own optical channel, and the maximum imaging depth at which the image quality is maintained. While steps *V1* and *V2* condense the visual information contained within the image stacks and render it more presentation-friendly, they do not enhance the quality of the imaging data itself. Therefore, they cannot substitute the need for robust fluorophores and imaging optics, which must also work well in concert with one another. Instead, these methods are themselves separate but equally important tools for making the most out of biological studies performed using *in vivo* multiplexed imaging.

5 Appendices

5.1 Details of Equipment and Methods used for the Characterization of QDs and *In vivo* imaging

Temperature control for the synthesis of QDs, purification of starting chemicals and making of QD precursors

The temperature controller REX-D100 (RKC Instrument, South Bend, Indiana) is used at its default factory setting with type K thermocouple (Omega Engineering, Stamford, CT) and variable autotransformer ("Variac"; Model 3PN1010, Staco Products, Dayton, OH) set at 140V maximum.

Absorbance spectroscopy

UV-Vis HP 8453 diode array spectrophotometer (Agilent, Santa Clara, CA) for up to 800nm detection; Cary 5000 UV-Vis-NIR spectrophotometer (Agilent, Santa Clara, CA) for detection range extending beyond 800nm.

Photoluminescence (PL) spectroscopy

Vis-NIR fiber optics spectrometer (USB4000 Vis-NIR; Ocean Optics, Dunedin, FL) with 594nm HeNe excitation. Fluoromax-3 (Horiba, Edison, NJ) for detection up to 800nm and for other excitation wavelengths.

Quantum yield (QY) measurements

QY of QD samples is determined using reference organic dyes that fluoresce at similar wavelengths and have known QY values: Oxazine725 (PL peak 660nm), with QY=11% in ethanol and HITC (PL peak 770nm), with QY=29% in methanol. The calculation is based on the following relationship, in which $Absorbance_{Dye}$ should approximate the value of $Absorbance_{QD}$ [9]:

$$QY_{QD} = QY_{Dye} \times \frac{Absorbance_{Dye}}{Absorbance_{QD}} \times \frac{PL\ Peak\ Area_{QD}}{PL\ Peak\ Area_{Dye}} \times \frac{n^2_{QDsolvent}}{n^2_{Dyesolvent}} \quad (Eq.10)$$

To ensure accuracy, each QY measurement uses fresh reference dye solution prepared the same day, as red- and NIR-fluorescent organic dyes are prone to photobleaching. Also, rather than trying to create two solution of similar absorbance values at the excitation wavelength of choice, three or more different concentrations of the reference dye are first measured for absorbance and PL peak area, which, as long as the solutions are appropriately dilute and proper "blanking" of the spectrophotometer has been performed, the data can be fitted with close-to-unity R^2 value to a linear equation in the form $y=mx+b$ (m=slope, b=y-intercept):

$$PL\ Peak\ Area_{Dye} = m \times Absorbance_{Dye} + b \quad (Eq.11)$$

Once this equation was known, *Eq.10* above can be simplified to:

$$QY_{QD} = QY_{Dye} \times \frac{PL\ Peak\ Area_{QD}}{PL\ Peak\ Area_{DyeLinEst}} \times \frac{n^2_{QDsolvent}}{n^2_{Dyesolvent}} \quad (Eq.12)$$

With $PL\ Peak\ Area_{Dye\ LinEst}$ being calculated from the linear equation using $Absorbance_{QD}$ as the $Absorbance_{Dye}$ value.

Of note, the commercially available NIR QDs, Qtracker 705 and 800, have not been used as references as their QYs reported in accompanying data sheets have deviated from the values re-measured using the method as detailed above, which has worked for other fluorophores with known QY values. A sample of Qtracker705 with a reported QY of 67%, for example, measured 31% when re-measured against Oxazine725; this may be due to sample destabilization (for example, due to aggregation and loss of adsorbed amphiphilic polymer) over time in storage. Literature has also reported discrepancies between the reported and actual QY value

for Qtracker 800 and 655 (90% vs. 71% for Qtracker655; 49 vs. 19% for Qtracker800) [17].

Transmission electron microscopy (TEM)

JEOL200cx (JEOL USA, Peabody, MA). After flocculation of a small volume growth solution aliquot as described in section 3.5.3.3, the hexanes solution is diluted to a concentration suitable for spectroscopic analysis (optical density <0.1 @ 350nm) and dried on a copper TEM grid in a vacuum chamber. Unless otherwise specified, images were taken at 200kV, 80kx magnification and the whole field is presented in the figures in this thesis. The whole grid is surveyed for colonies of MSNCs and other extraneous populations of QDs. Measurement of QD size is performed with ImageJ [1]. An ellipse is drawn around each nanocrystal and its area is measured. The area measurements of >50 QDs from >5 image fields (except for early samples) are then averaged, from which the mean diameter is calculated and reported as size. If ultrasmall MSNCs or QDs with shapes that significantly deviate from a sphere are present, their images are captured but they are not included in size measurements; TEM is the repeated for the storage solution after a "standard" flocculation (section 3.5.3.1) is performed on the growth solution and the size calculation is repeated.

X-ray powder diffractometry (XRD)

X'Pert Pro Multipurpose Diffractometer (PANalytical, Westborough, MA) with Cu K_α as source radiation and a variable divergent slit to fix the irradiated length to 6mm length X 10mm width. The diffractometer was operated at a 2θ range of 20 to 60°; the operating voltage and current were 45kV and 40mA respectively. QD samples are flocculated as described in section 3.5.3.1, suspended in hexanes and dried on ZBH (zero background holder) for crystal structure analysis.

Inductively-coupled plasma atomic emission spectroscopy (ICP-AES)

Activa-S ICP Spectrometer (Horiba Jobin Yvon, Edison, NJ). ICP standard solutions for Cd (1000mg/ml in 2% nitric acid), Te (1000mg/ml in 5% nitric acid) and Se (1000mg/ml in 2% nitric acid) are purchased from Perkin Elmer (Waltham, MA). Standard solution for S (1000mg/L as H_2SO_4; Fluka brand) and nitric acid (≥69% puriss ACS reagent ISO.) are purchased from Sigma-Aldrich (St Louis, MI). Deionized water, reagent grade, is purchased from Ricca Chemical Company (Arlington TX). QD samples are flocculated as described in section 3.5.3.1, then digested overnight in 2% nitric acid for elemental analysis.

Gel filtration chromatography (GFC)

ÄKTAPrime Plus™ System with Superose 6 10/300 GL size exclusion column (GE Healthcare, Pittsburgh, PA).

Size Analysis by Dynamic Light Scattering (DLS)

DynaPro Titan Dynamic Light Scatterer with 830nm diode laser excitation (Wyatt Technology Corporation, Santa Barbara, CA).

Confocal microscopy for *in vitro* live cell imaging

Leica TCS NT Microscope (Leica Microsystems, Buffalo Grove, IL) with argon-488nm / krypton-568nm / HeNe-633nm as laser sources. 100x PLAN APO 1.4NA oil immersion objective lens is used to image live cells. Cells are cultured in their optimal medium and re-plated in 1-well chamber slides (Lab-Tek™, Nalge Nunc International, Rochester, NY) one day prior to labeling and imaging, targeting for ~50% confluence. After labeling, the cells are washed 3x with phosphate-buffered saline (w/ Ca^{2+}, Mg^{2+}), set on ice and immediately imaged.

In vivo murine bone marrow imaging

Lin Lab has developed a video-rate (30 frames per second) laser scanning hybrid confocal/two-photon microscope specifically designed and optimized for live animal

imaging (Figure 1.1; also see [61,107,164]). The scope uses a 30x, 0.9NA water immersion objective (LOMO PLC, St Petersburg, Russia) and is equipped with a titanium: sapphire laser (Mai Tai HP, Spectra Physics, Irvine, California) for two-photon excitation between 700-1100nm, as well as 491nm, 532nm and 633nm solid state lasers for single photon excitation. 6 channels are available for detection. Exact excitation and detection conditions are specified in the text.

5.2 Coordination Chemistry of Metal (II) Carboxylates

Metal-carboxylates are weaker in binding strength and structurally more diverse compared to metal-phosphonates. The paucity of literature on polymer formation in cadmium may mean the process favors smaller, lower atomic number elements (the first ionization energy of cadmium and zinc are similar, at 867.7 and 906.4kJ/mol). Zinc carboxylate can form polymer sheets, as well as polymer chains and the closed, octahedrally-coordinated tetranuclear oxo complexes $M_4O(RCOO)_6$. Stereochemistry of the hydrocarbon side chain and the temperature of the system determines the configuration; both the polymer sheet and chain configurations conform stoichiometrically to a bi-dentate linkage ($RCOO^-/Zn = 2$) referred to in QD literature, but the oxo complex has a lower ratio at 1.5 [11,66,89,118]. *Saturated*, linear metal-alkanoates previously used as QD precursors (cadmium and zinc stearate and mystriate, for example) mostly take on the polymer sheet structure [11,48]; as heat is supplied, however, the polymer chain configuration becomes dominant and when temperature rises above its melting point, the tetranuclear oxo complex, which is accompanied by free acid release and simultaneous decomposition of the highly volatile oxo complexes to form metal oxide. The exception is with the presence of water, which leads to the dominance of tetranuclear oxo complexes even under moderate temperatures [21,48]. In general, temperature of these transformations decreases at longer carboxylate chain length [21]; these phase transformations are also highly reversible, and modulating the equilibrium between these complexes and the polymeric forms results in notable changes in viscosity [11,21,48].

Studies on metal-carboxylates have not considered oleic acid, however, which, as one of the most popular acid in QD synthesis, carries a linear but *unsaturated* hydrocarbon chain. Nonetheless, what is understood about the phase transitions between polymer sheet, chain and oxo complexes offer insights to the structural configurations possibly favored by cadmium and zinc oleate complexes. The

hydrocarbon chain plays the most significant role in controlling the configuration, barring temperature and solvent effects, and the ease with which the hydrocarbon side group of the carboxylates can align in an all *trans* configuration [21] determines the likelihood of each configuration: those that aligns the easiest form polymer sheets, then polymer chains, then tetranuclear oxo compounds. Case in point, carboxylates with linear alkyl chain form polymer sheets but those with *branched* alkyl chains form polymer chains [11,21]. At high temperatures, all carboxylates assume the tetranuclear oxo compound configuration due to entropy.

For oleates, their *cis* double bond mid-chain (carbon 9) renders them unlikely to assume the all-*trans* alignment that favors sheet arrangement. Studies on the crystallization of oleic acid have shown that it is polymorphic, its most stable β phase characterized by a non-segregated arrangement of carboxylate and methyl groups. This arrangement, not seen in other *cis*-monounsaturated acids [82], has been attributed to the equal number of carbons on the two sides of the double bond in oleic acid. Cadmium and zinc oleates are therefore expected to polymerize in smaller scales—as polymer chains, for example, which would differentiate them from the polymer sheet configured cadmium and zinc-phosphonates. In the context of the synthesis and processing of QDs, it may explain why the bulky coordination polymers have appeared exclusively in schemes that incorporate metal-phosphonates but not metal-carboxylates, which are mostly metal-oleate.

5.3 Purification of Starting Chemicals for $CdTe_xSe_{1-x}$ QD Synthesis: Detailed Protocols

Proper preparation of tools and glassware is needed to ensure cleanliness and consistency. All glassware contacting the chemicals should be free of water and other polar solvents (particularly alcohols), which drastically change the yield of the purification processes. Stainless steel spoons can produce substantial amount of particles when scratched, often at the neck of the flasks when scraping chemicals, and should also never be exposed to corrosive environment (ex. the acid bath) that further soften the material. Glass frits and columns used for each chemical are dedicated for their purpose, so that their history of use is known and can be properly cleaned without risking damage to the pores for filtration. Fresh stir bars are preferred, and stir bars that have seen the base or acid baths are never used, both in purification and synthesis.

All temperature ramping performed during purification (and synthesis) is set at a rate that ensure no sudden "spikes" in the temperature profile. This requires the temperature controller to adopt a setting that allows no temperature overshooting. Even with identical loop feedback (PID) settings, however, different thermal controller models in the lab have exhibited significant variations in their ramping and set point maintenance behavior. For this reason, all experiments in the project are performed with one model (REX-D100; RKC Instrument, South Bend, Indiana) that exhibits the least overshooting behavior and ramps at a consistent rate of $(T_2-T_1)/10$ min at its default factory setting. Type K thermocouple is always used (Omega Engineering, Stamford, CT) and the variable autotransformer ("Variac"; Model 3PN1010, Staco Products, Dayton, OH) is set at 140V maximum. Smooth temperature profiles are then achieved by a step-wise temperature set point increase and stabilization towards the target temperature, with the intermediate set points near the melting point of the solid chemicals.

5.3.1 Purification of trioctylphosphine oxide (TOPO) with anhydrous heptane

Successful purification of TOPO via recrystallization has been reported in literature. As an alternate method, distillation has been described as ineffective ([189]; communications with former Bawendi lab members). Other purification methods described involve the use of water, which is avoided to ensure the purified products are completely anhydrous for QD synthesis [12].

The purification protocol has been developed and optimized based on using 200 g, 99% TOPO as the starting chemical. The choice of heptane as the anti-solvent takes into consideration that impurities found in alkanes are usually hydrocarbons of similar molecular weights and sans function groups, thus minimizing the chance that residual heptane in the purified TOPO would include impurities that cannot be removed or lead to secondary reactions during pre-synthesis degassing. Acetonitrile, the anti-solvent previously cited for TOPO recrystallization [189], has multiple families of impurities that include water, acids, bases (ammonia), and multiple species of metals [3,39]; the quantity of the anti-solvent required is also much larger (100g TOPO: 200mL for acetonitrile [189]). Heptane's boiling point at 98°C renders its evaporation rate slower than hexanes, but not so high that removal becomes a challenge.

The purification protocol begins with degassing, which removes residual solvents from the manufacturing process and any impurities with boiling points below TOPO's. Residual solvents in TOPO can lead to poor yields from recrystallization; for example, TOPO is highly soluble in the alcohols (>2.2g TOPO in 1 mL ethanol) and crystallization would fail if even a trace amount of the latter has been mixed in the heptane.

The second step involves two rounds of crystallization and washing with anhydrous heptane. Recrystallization is performed at room temperature, as some impurities are found to solidify into yellow patches that are not easily separable from the TOPO crystals at 4°C. Meanwhile the washes are performed with heptane cooled in dried ice, as TOPO's solubility in heptane is non-trivial. The final step is a slow, evaporative drying of the crystallized TOPO just below its melting point (~50°C), as re-solidified TOPO is notorious difficult to work with (and the hard scraping needed often leads to significant amount of particulate contamination). As dried TOPO crystals are extremely "fluffy", rotovap must be used with caution and may be used only up to a certain point, as the TOPO flakes are easily vacuum-suctioned from the evaporation flask to the rest of the apparatus. The rest of the drying is best performed on the schlenk line.

5.3.1.1 TOPO Recrystallization, The Protocol

99% TOPO from Strem Chemicals (Newburyport, MA) is preferred over 99% TOPO from Sigma Aldrich (St Louis, MO) with its lower impurity concentration. Anhydrous 99% heptane is from Sigma-Aldrich and should be fresh at use; air storage is okay for the duration of the purification.

1. Degas up to 200g of TOPO at near the boiling point of the chemical (~150°C depending on base vacuum and TOPO purity) until pressure is stable. The process should take ~30-45min for each 100g TOPO.

2. For each 100g TOPO (and up to 200g), prepare 75mL anhydrous heptane in a large neck and sealable glass container.

3. When TOPO degas is complete, release to N_2 atmosphere and cool to ~90°C. Release to air and immediately pour into the prepared heptane. Seal cap with

Parafilm and swirl gently until TOPO and heptane is thoroughly mixed and no more "swirl patterns" can be seen in the solution. If the solution turns turbid, heat gently until the TOPO melts and the solution becomes clear again, taking care to not raise the temperature above the boiling point of heptane (~98°C @ 760mmHg).

4. Set the flask aside for the first recrystallization in room temperature. Perturbation should be minimal to allow for a slow, well-paced recrystallization, which should commence within 2 hours. The first recrystallization should be left overnight (~12 hrs.), as impurities weaken the crystal and render the recrystallization process slower than in subsequent runs. The TOPO is ready when "cloves" can be seen in the crystal, and no liquid flows out when the container is tipped.

5. Prepare iced heptane in dry ice bath. Transfer TOPO crystals in small increments into a fine glass frit and wash them twice with approximately equal volume of iced heptane, using a light vacuum to draw the solvent down the frit. Place all clean crystals in a new container; also collect all heptane collected to determine loss.

6. Tare an evaporation flask for rotovap. Dry the heptane collected in 5. on the rotovap and weigh the approximate weight of TOPO lost (should be ~5%). This highly impure TOPO solid should also look very yellow and has an oily/waxy consistency compared to the starting chemical.

7. Perform the second recrystallization of the crystals collected in Step 5, factoring in the loss in TOPO weight determined from Step 6 and also the amount of heptane still present in the clean crystals, which can be determined by weighing the wet crystals and subtract the value by the now known weight

of TOPO inside. Melt the TOPO gently (again, avoid reaching the boiling point of heptane = 98°C) and add the appropriate amount of heptane so that the ratio of 100g TOPO : 75mL heptane is followed; swirl to mix thoroughly. The crystallization should also begin <2hr; for this round, 4 hours (after the start of the crystal forming process; ~6 hours total) should suffice for the recrystallization to complete; again, crystal "cloves" should be visible and no liquid should flow out when container is flipped.

8. Repeat 6. for second wash. If the loss is collected, it should look visibly similar to the recrystallized TOPO, with little to no difference in color and consistency. If not, the recrystallization and wash should be repeated. The total loss from the two recrystallizations should be ~10%.

9. Dry the TOPO crystals. As previously mentioned, TOPO crystals are "fluffy" and hence, of low density—200g of the crystals, once dried, occupy a volume upwards of 500mL. Rotovap can be used for the initial drying, with the water bath temperature gradually increased to 45°C (below TOPO's melting point); when the TOPO becomes dry enough that the risk of contaminating the rotovap becomes significant, the drying process should be moved to a schlenk line. It is advisable to use a long distilling column (30cm length, 24/40 joint) to separate the flask with TOPO from the schlenk line, although in previous experiences, TOPO contamination is not an issue at this stage. As heating mantle cannot distribute heat well in solids, room temperature and long drying time is preferred. This final step should also be performed in smaller batches of TOPO to ensure thorough drying.

5.3.2 Purification of octylphosphonic acid with anhydrous heptane

The choice of n-octylphosphonic acid (OPA) as the acid ligand for QD synthesis takes into consideration that the same acid species is supplied by TOPO both as a starting impurity and a high temperature oxidation product. It is important to note that the purity level (~98%) specified by the manufacturer can be based on total acid content and not the content of the OPA itself. The main purpose of this purification is to remove non-acids from the starting chemical.

Recrystallization is again the chosen method upon determining the proper anti-solvent, which consists of heptane mixed with a small volume of toluene. As the anti-solvent, heptane (boiling point: 98°C @ 760mmHg) offers the advantages as described in the previous section on the purification of TOPO, but is too non-polar (and therefore insoluble to OPA) to permit a well-paced OPA recrystallization at reasonable volumes. On the other hand, OPA recrystallization in the more polar toluene alone is very slow and the yield tends to be poor; using significant amounts of toluene may also leave behind residual acid and water [80]. Just like heptane, toluene has a boiling point (111°C @ 760mmHg) suitable for solubilizing hot OPA (melting point: 100-102°C @ 760mmHg).

Similar to the recrystallization of TOPO, the protocol begins with degassing and proceeds to recrystallization. The protocol is developed based on 35g starting OPA; larger batches are not recommended due to the high cost of the chemical. It should be noted that this protocol does NOT work for long chain phosphonic acids, including tetradecylphosphonic acid and octadecylphosphonic acid.

5.3.2.1 Octylphosphonic Acid Recrystallization, The Protocol

98% Octylphosphonic acid is from PCI Synthesis (Newburyport, MA). Anhydrous heptane 99% is from Sigma-Aldrich (St Louis, MO). Toluene, 99.85%, Extra Dry over Molecular Sieve, Acroseal is from Acros Organics (New Jersey, US).

1. Degas 35g OPA on the schlenk line at 120°C for one hour, or until pressure is stable. Switch to N_2.

2. Prepare 175mL heptane in a large neck, sealable glass container and pre-warm to ~85°C, while keeping the container covered (but not sealed) to slow down evaporation.

3. Decrease OPA temperature to ~105°C and inject 12mL toluene (b.p.=111°C). Then release content to air and quickly but carefully pour the OPA-toluene solution into the warmed heptane. Seal cap with Parafilm and swirl gently until the solution is thoroughly mixed and no more "swirl patterns" can be seen in the solution. If the solution turns turbid and/or the OPA solidifies, maintain the solution temperature at 85-90°C until the solids melt and the solution clarifies again, taking care to not raise the temperature above the boiling point of heptane (~98°C @ 760mmHg).

4. Set the flask aside for recrystallization in room temperature. Perturbation should be minimal to allow a well-paced recrystallization, which should commence quickly (~8-10min) and but will require 40 hours to complete. The crystals should resemble small, iridescent flakes.

5. Prepare iced heptane in dry ice bath. Transfer OPA crystals in small increments into a fine glass frit and wash them twice with approximately equal volume of iced heptane, using a light vacuum to pull the solvent down the frit. Place all clean crystals in a new container. If need to determine loss, collect all the solvent.

6. To determine loss, tare an evaporation flask for rotovap, dry the heptane collected in 5. on the rotovap and weigh the approximate weight of OPA lost (should be ~7%).

7. Dry the OPA crystals on schlenk line, slowly increasing the temperature from room temperature to 80°C. Once again, a long distilling column (30cm length) may be useful to separate the flask from the schlenk line and avoid contamination.

5.3.3 Purification of hexadecylamine

Impurities in hexadecylamine (HDA; boiling point b.p. 322.8°C @ 760mmHg) have been reported to include their isomers and other linear alkyl amines of similar chain lengths. The data sheet for 90% HDA from Sigma Aldrich, for example, lists the presence of 3% tetradecylamine (b.p.: 296°C @ 760mmHg) and 3% octadecylamine (b.p.: 346.8°C). While amines are considered weak ligands that act as facilitators of monomer incorporation, $CdTe_xSe_{1-x}$ QD synthesis has demonstrated sensitivity to lot switching even when 98% hexadecylamine (Sigma) is used.

Studies on the industrial purification of amines has indicated that distillation is effective for separation of amines with distinct boiling points, while isomer extraction requires creating amine complexes (ex. reaction with a reactive carbonyl via treatment with acid [170]) to achieve full resolved separation. Such chemistries often involve an aqueous phase, which is not desirable for preparation of chemicals for QD synthesis. A simple recrystallization using benzene has been recommended for HDA purification in *Purification of Laboratory Chemicals* [12] and in the purification protocol developed for this project, which uses 98% HDA as starting chemical and also comprises of degassing followed by recrystallization, heptane has replaced benzene

for reasons as stated for TOPO and OPA. The primary goal of this purification protocol is to remove non-amine impurities.

5.3.3.1 Hexadecylamine Recrystallization, The Protocol

98% Hexadecylamine (melting point: 38-47°C @ 760mmHg) and anhydrous heptane 99% is from Sigma-Aldrich (St Louis, MO).

1. Degas 125g HDA on the schlenk line with a gradual temperature ramp to 105°C; hold temperature at 105°C, at which reflux should commence, until pressure is stable. Do not attempt to return the small amounts of material deposited on the distillation column into the flask. Switch to N_2.

2. Prepare 187.5mL heptane (general guideline: 1g HDA: 1.5mL heptane) in a large neck, sealable glass container.

3. Lower the temperature of HDA to ~80°C and release it to air. Carefully pour the hot liquid into the heptane. Seal cap with Parafilm and swirl gently until the solution is thoroughly mixed and no more "swirl patterns" can be seen in the solution. If the solution turns turbid and/or the HDA solidifies, heat up the solution in small increments—the final temperature should be well below the boiling point of heptane (~98°C @ 760mmHg).

4. Set the flask aside for recrystallization in room temperature. Perturbation should be minimal to allow a well-paced recrystallization, which should commence in ~30min. In previous runs, the crystallization is allowed 3 days to complete—whether a shorter duration provides the same yield has not been tested.

5. Prepare iced heptane (set in dry ice bath). Transfer HDA crystals in small increments into a fine glass frit and wash them twice with approximately equal volume of iced heptane, using a light vacuum to pull the solvent down the frit. Place all clean crystals in a new container. If need to determine loss, collect all heptane.

6. To determine loss, tare an evaporation flask for rotovap, dry the heptane collected in 5. on the rotovap and weigh the approximate weight of HDA lost (should be ~11%). Much like the case for TOPO, the loss tends to carry a yellow tint compared to the purified product—it also has a higher melting point, thus may be enriched in heavier amines such as octadecylamine.

7. Dry the HDA crystals on schlenk line, slowly increasing the temperature from room temperature to 60°C. Once again, a long distilling column (30cm length) may be useful to separate the flask from the schlenk line and avoid contamination.

5.3.4 Purification of Squalane and Squalene

Purification of Laboratory Chemicals [12] has recommended the recrystallization of squalene using acetone (@ 1.4ml/g) as the anti-solvent in a dry ice bath, which is followed by a cold acetone wash. The purification protocol as described below is the first trial for squalane (the hydrogenated form of squalene); a similar protocol is expected to perform well for squalene but with the acetone: squalene ratio set to 1.4ml/g [12].

A visual clue of the impurity levels in squalane is the degree of yellow to yellow-green hue in the starting chemical. Purified squalane is almost colorless; meanwhile,

comparison of the various bottles of 98% and 99% squalane found in lab revealed that 98% squalane carried a significantly stronger yellow tint, the intensity of which differed between lots and was extracted during recrystallization. The impurities involved were also found to be more viscous than squalane after the decanted acetone had been removed by rotovapping.

5.3.4.1 Squalane Recrystallization, The Protocol

99% Squalane and 99.9% Acetone (CHROMASOLV) are available from Sigma Aldrich (St Louis, MO).

1. Mix 200mL squalane and 100 mL acetone thoroughly in sealable glass container.

2. Place squalene-acetone solution in dry ice bath; a thick gel should form over time, indicating the crystallization of squalane. Meanwhile, cool acetone in dry ice until the temperature matches that of the squalane solution.

3. Decant acetone. Pour in 200mL iced acetone, then decant and repeat 3x for washing. As squalane's melting point is -38°C and dry ice sublimation temperature is -56.4°C, the procedure should be performed quickly and with the temperature of acetone as low as possible.

4. Dry squalane first by rotovap, then on the schlenk line at near boiling point to remove solvents until base pressure is reached. It is then transferred, air-free, into the glove box for storage.

5.3.5 Activated alumina column filtration of trioctylphosphine (TOP)

The use of activated alumina to remove phosphinic acids was recommended for the purification for TOPO [12] and has since been applied to the purification of TOP, which carry similar impurities as its oxide. Adsorptive filtration with activated alumina is largely limited to the removal of acids but not the other impurities such as dialkylphosphines; distillation, which has been tested as an alternate method to filtration, has also shown to be ineffective in removing all impurities from the TOP, presumably due to similar boiling points between the phosphine and its impurities.

Preparation of clean TOP therefore combines the following strategies:

1) Use 97% TOP as starting chemical. The bottles are opened in the glove box immediately before purification to avoid contamination from previous usage.
2) Columns for TOP filtration with activated alumina are dedicated to this purpose only. Filtration takes place in the glove box.
3) Alumina-treated TOP is immediately degassed (and filtered through glass frit to remove any alumina particulates), thus removing most non-acidic impurities with lower boiling points than TOP. Only degassed TOP is introduced into synthesis, including the making of precursor solutions.

5.3.5.1 TOP Purification, The Protocol

97% TOP is available from Strem Chemicals Inc. (Newburyport, MA). Activated aluminum oxide, basic, Brockmann I is available from Sigma Aldrich (St Louis, MO) and should be fresh to ensure minimal amounts of adsorbed water. Econo-Column Chromatography Columns (2.5cm*20cm max vol. 98mL) from Bio-Rad (Hercules, CA) are used for filtration. Fresh Tygon tubing (R-3603; I.D.:3/16in, O.D.:5/16in) may be

used to guide the filtrate from the flow adaptor of the column into the collection container.

1. All columns used for TOP filtration are dedicated for this use only. They (and any Tygon tubing to be used) are thoroughly cleaned with methanol and repeated rinses of hexanes and dried prior to introduction into the glove box. Only fresh bottles of TOP are used.

2. Set up the filtration system in the glove box. 4 columns are usually set up for each 500g bottle of TOP to expedite the process, which is slow as it must occur at near atmospheric pressure. From experience, older or more impure TOP, which tends to be more viscous, also slows the process. For each column, ~80mL space is filled with activated alumina.

3. Pour in TOP continuously and in small increments until filtration is complete. A significant volume of TOP remains in the alumina column at this point; to collect this TOP, a 10mL syringe can be used to "inject" the O_2-free atmosphere into the column through a Tygon tubing connecting the syringe to the cap of the column. Steps 2 and 3 have, in general, taken approximately 40 hours to complete (for each bottle of TOP).

4. A note on cleanup of these columns: TOP oxidation is exothermic and the amount left behind in the columns is sufficient to ignite paper products nearby. Clear the hood of all paper products prior to retrieving the columns from the glove box. Once in the hood, place the columns in a large glass beaker and immediately put in hexanes to flush out the remaining TOP out of the alumina. After the initial hexanes rinse, ethanol should be used as well.

5. Degas the filtered TOP at 145°C. When performed in batches of ~150mL, approximately two hours should be sufficient time for the TOP to reach base pressure. As TOPO and phosphonic acids are known oxidization products of TOP at high temperatures, the temperature and duration of these degassing runs should be consistent.

This protocol can also be used for the purification for TBP, the filtration time of which is much faster with steps 2-3 taking approximately 6 hours. Extra care should be taken during cleanup as TBP oxidizes more aggressively than TOP.

5.4 Protocol for the Synthesis of CdS@$CdTe_xSe_{1-x}$: With Sulfur Incorporation / Overcoating: Original Worksheet Format

The worksheets attached are the protocols for samples PL 672/35 and PL770/61 in their original format. They are included to provide a better picture of how the syntheses are planned and performed. The chemistry and steps are highly similar to the protocols described in section 3.5.2.

	Volume (ml)	Density(g/ml)	Weight (g)	Mol Weight (g/mol)	Moles (mol)	Moles (mmol)		TRUE vol	PREMIX vol
PL672/35									
TOP (w/DPP) Lot8134048 Filtered/Degas	0.6700	0.8300	0.5561	370.6427	0.0015	1.5004	TOP-Te 1.0M vol	0.0600	0.0720
1-Octylphosphonic acid (PCI99.4%)	NA	NA	0.0000	194.2100	0.0000	0.0000	TOP-Se 1.8M (Growth)	0.0083	0.0250
Hexadecylamine 98% ReXtal	1.0692	0.8130	0.8693	241.4600	0.0036	3.6001	TOP vol (w/Cd-OPA)	0.2400	0.2880
0.5M Cd-OPA 1:1.25 in TOP **(Feb10)**	0.2400					0.1200	TOP-S 2.24M (w/TOP-Se)	0.1868	0.5605
Diphenylphosphine 98% (in 25%v/v Squalene)	0.0042	1.0700	0.0045	186.2000	0.0000	0.0240	Squalene vol (w/Te)	2.9400	3.5280
TOPO 99% Lot2178108 ReXtal	8.0000	0.8700	6.9600	386.6421	0.0180	18.0011	DPP	0.0042	0.0050
							Total Te+Se VI mmol	0.0750	
	9.9834	4.9800					Te% in CdTeSe	0.8000	
Growth soln: TOP-Se+ TOP-S immediate, then Cd-OPA slow after injection.							PostInject TOP 97%	0.6700	(Filtered)
TOP-Se 1.8M	0.0083					0.0150	Amine / Acid Post Se	13.7147	
TOP-S 2.24M (Sat 2.5M)	0.1868	Separate needle; entry immediate after Te				0.4185	Amine / Acid Post S	8.0002	
	SUM VI	*0.1952*	*[Se] (M)*	*0.0803*					
0.5M Cd-OPA 1:1.25 Post Se	0.1800					0.0900			
TOP-S 2.24M (Sat 2.5M)	0.3757	Separate needle				0.8415			
Sum vol	*0.5557*	*Divide 3*	*0.1852*						
	*CdOPA*1.5*	*0.3600*	*TOP-S*1.5*	*0.7513*					
ODE-S 1.0M (Sat)	4.0650					4.0650			
0.5M Cd-OPA 1:1.25 Post-S	0.3000					0.1500			
PL672/35	*No wool*	*Stirrer: 850rpm*			Line base p	170mtorr			
Start degas	9:58pm	Temp	125C						
End degas	10:08pm	Final pressure	171mtorr	Stable. Hold at vac 125C					
Inject TOP	10:08pm	125C, vac for 5min (final p=171mtorr); switch to N2							
No Wool. Set T = 358.5C = inject T+1.0C	10:13pm	No wool.							
	Reach 357.5C 10:22pm -->	Set T = 315C							
	Inject **Cd-OPA+TOP-Te+Squalene+DPP (16G needle/6mL syringe),**								
	Then immediately inject TOP-Se+TOP-S (16G needle/3mL syringe, stick in flask before Te inject) @ 357.5C 10:24:00pm								
	Heat pad REMAINS ON; T drops to ~304.5C then rapidly climbs back to **323-324C** growth temp								
	Inject **CdOPA+TOP-S for 3minutes: start 10:24:30pm (30sec)** ; constant rate - 0.185mL / min --> 0.062mL/20sec, with 1mL syringe, 21G needle								
	Hold 30sec (so total CdTeSe growth time=4min). Start natural cool. Immediate set T=200C								
	Inject all ODE-S w/ 21G needle at 6min00sec after natural cooling: @ T=247C. T drop to 212C								
	Heat pad on. T overshoots to 215C then stabilize at 200C								
	Start Cd-OPA inject 10:32:00pm (8:00min/10min total)								
	Rate: 0.03mL/1 min=0.01mL/20sec for 10min								
	Hold for extra 2 min after Cd-OPA done. **@ 20 min (10:44pm) Inject 0.67mL TOP. Start natural cool** to RT								
	10:54pm	30min	76C	Spec					
	10:57pm	33min	T@64C	TDPA in; start ~0.5hr vac + 80C anneal					
NIR Spec: 33min79C V. Dilute, before TDPA	Peak	672.4700							
300msec	FWHM	37.65 (654.05-691.6)		50% peak value	1688.7000				

	Volume (ml)	Density(g/ml)	Weight (g)	Mol Weight (g/mol)	Moles (mol)	Moles (mmol)		TRUE vol	PREMIX vol
PL770/61									
TOP (w/DPP) Lot8134048 Filtered/Degas	0.6700	0.8300	0.5561	370.6427	0.0015	1.5004	TOP-Te 1.0M vol	0.0600	0.0720
1-Octylphosphonic acid (PCI99.4%)	NA	NA	0.0000	194.2100	0.0000	0.0000	TOP-Se 1.8M (Growth)	0.0250	0.0600
Hexadecylamine 98% ReXtal	1.0692	0.8130	0.8693	241.4600	0.0036	3.6001	TOP vol (w/Cd-OPA)	0.2400	0.2880
0.5M Cd-OPA 1:1.25 in TOP **(Feb10)**	0.2400					0.1200	TOP-S 2.24M (w/TOP-Se)	0.3281	0.7875
Diphenylphosphine 98% (in 25%v/v Squalene)	0.0042	1.0700	0.0045	186.2000	0.0000	0.0240	Squalene vol (w/Te)	2.9400	3.5280
TOPO 99% Lot2178108 ReXtal	8.0000	0.8700	6.9600	386.6421	0.0180	18.0011	DPP	0.0042	0.0050
							Total Te+Se Vl mmol	0.1050	
							Te% in CdTeSe	0.5714	
Growth soln: TOP-Se+ TOP-S immediate, then Cd-OPA slow after injection.							PostInject TOP 97%	0.6700	(Filtered)
TOP-Se 1.8M	0.0250					0.0450	Amine / Acid Post Se	13.7147	
TOP-S 2.24M (Sat 2.5M)	0.3281	Separate needle; entry immediate after Te				0.7350	Amine / Acid Post S	8.0002	
0.5M Cd-OPA 1:1.25 Post Se	0.1800					0.0900			
TOP-S 2.24M (Sat 2.5M)	0.1875	Separate needle				0.4200			
ODE-S 1.0M (Sat)	4.1400					4.1400			
0.5M Cd-OPA 1:1.25 Post-S	0.3000					0.1500			
PL770/61	*No wool*	*Stirrer: 850rpm*			Line base p	170mtorr			
Start degas	5:54pm	Temp	125C						
End degas	6:04pm	Final pressure	172mtorr	Stable. Hold at vac 125C					
Inject TOP	6:04pm	125C, vac for 5min (final p=172mtorr); switch to N2							
No Wool. Set T = 358.5C = inject T+1.0C	6:09pm	No wool.							
	At 358.5C 6:28pm --> Set T = 315C 6:30pm								
	Inject **Cd-OPA+TOP-Te+Squalene+DPP (16G needle/6mL syringe),**								
	Then immediately inject TOP-Se+TOP-S (16G needle/3mL syringe, stick in flask before Te inject) @ 357.5C 6:31:15pm								
	Heat pad REMAINS ON; T drops to ~301.2C then rapidly climbs back to 322C growth temp								
	Inject **CdOPA for 3minutes: start 6:31:45pm (30sec)** ; constant rate - 0.18mL / 3min --> 0.03mL/30sec, with 1mL syringe, 21G needle								
	Hold 30sec (so total CdTeSe growth time=4min). Start natural cool.								
	During cool inject TOP-S in 3 batches: 30sec per batch								
		4min30sec	0.625ml	(At 310C)					
		5min0sec	0.625ml						
		5min30sec	0.625ml						
	Inject all ODE-S w/ 21G needle at 6min00sec after natural cooling: @ T=245C. T drop to 208.4C								
		Heat pad on. T overshoots to 215C then stabilize at 200C							
	Start Cd-OPA inject 6:39:15pm (8:00min/10min total)								
		Rate: 0.03mL/1min=0.01mL/20sec for 10min							
	Hold for extra 2 min after Cd-OPA done. **@ 20 min (6:51:15pm) Inject 0.67mL TOP. Start natural cool** to RT								
		7:01pm	30min	79C	Spec				
NIR Spec: 33min79C V. Dilute, before TDPA	Peak	768.7500							
300msec	FWHM	62.9 (734.1-797.05)		50% peak value	923.8000				

5.5 Absorption Cross Section Calculation for Determining $CdTe_xSe_{1-x}$ QD Concentration

Accurate determination of the concentration of alloyed QDs is hindered by the unknown effect of alloying and the composition gradient on the absorption cross section of the nanocrystals. Thus for this project, the concentrations are calculated by first assuming the QDs as pure CdTe and CdSe QDs, and then taking a weighted average of the two concentration values based on their estimated composition. The contribution of each value is decided based on the fluorescent wavelength of the samples, which have been of fairly similar sizes (~5.5nm diameter): PL700 → 80%Te, PL 720 → 70% Te, PL 740→60% Te; all samples with longer fluorescent peaks are assumed to be 50%Te. Because CdTe's extinction coefficient is ~150% the value of CdSe's based on the Leatherdale model (see below), the concentration of QDs for a given absorbance value is expected to be ~150% more if the QDs are assumed to be CdSe compared to CdTe. Thus even if the weighted average method is correct in calculating alloyed QD concentrations, a wrong guess of the QD's composition can still deviate the concentration estimation by this numerical scale—which is not so significant that a practical estimate of the amount of QDs to introduce for post synthesis steps, such as overcoating or water solubilization, cannot be made (the amount of QDs to use for polymer encapsulation, as described in section 3.7, has been determined using the calculations below), but render estimations of other parameters such as reaction yields to be not very meaningful.

Concentrations assuming pure CdSe and pure CdTe QDs are determined based on the method published by Leatherdale et al. [98], but which only described the outcome for CdSe. To determine the absorption cross-section for CdTe QDs, published material constants for CdTe were substituted into the equations. The worksheet attached detailed subsequent calculations that cumulated to the following relationships, with the excitation wavelength set at 350nm:

Absorption cross section $C_{abs,\,CdTe}\,(cm^2)=8.247x10^5*a^3$ *(Eq.13)*

Molar extinction coefficient $\varepsilon_{CdTe}\,(M^{-1}cm^{-1})=2.156x10^{26}*a^3$ *(Eq.14)*

a is the QD radius in cm. To ensure accuracy, the worksheet also includes CdSe to verify that the outcome of the calculations agrees with the values reported in Leatherdale. Furthermore, it confirms that wurtzite versus zinc blende material constants make little difference in the absorption cross section and molar extinction coefficient values for CdSe, which is important to know as only zinc blende CdTe material constants can be found in literature.

```
> restart;
```

Define constants
N_a = Avogadros number
h = Planck's constant
c = speed of light

```
> N_a := 6.022E23 :
  h := 6.626E-34 :
  c := 299792458 :
```

Define hexane optical parameters
Data from Kerl&Varchmin JMolStruc349 1995.

Also input experiment conditions
T = 300K
Wavelength of excitation = lambda_ex = 350nm

```
> a1_hexane := 1.53157227 :
  b1_hexane := -5.5035E-4 :
  a2_hexane := -4.6005 :
  b2_hexane := 2.2803E-3 :
  a3_hexane := 6159.3 :
  b3_hexane := -5.9360 :
  σ1_hexane := 8.9E-5 :
  σ2_hexane := 3E-5 :
  d0_hexane := 0.8262917 :
  d1_hexane := -2.52E-4 :
  d2_hexane := -10.8E-7 :
  σ1_dhexane := 2E-5 :
  Molweight_hexane := 86.18 :
```

```
> T := 300 :
  λ_ex := 350 :
  ω_ex := 2·Pi·c / λ_ex :
```

n_hexane_tab is the tabulated refractive index of hexane = 1.3749 @ 20C

Calculate complex refractive index for hexane, m_hexane := n_hexane - ik_hexane based on parameters above
(Only n_hexane is used later; else has imaginery term in absorption cross section)
n unitless; k unit = M/nm

```
> n_hexanetab := 1.3749 :
```

$$> n_{hexane} := a1_{hexane} + b1_{hexane} \cdot T + \frac{\left(a2_{hexane} + b2_{hexane} \cdot T\right)}{\lambda_{ex}} + \frac{\left(a3_{hexane} + b3_{hexane} \cdot T\right)}{\lambda_{ex}^2} :$$

$$> \rho_{hexane} := d0_{hexane} + d1_{hexane} \cdot T + d2_{hexane} \cdot T^2 :$$

$$> \alpha_{hexane} := evalf\left(solve\left(\frac{\left(n^2_{hexane} - 1\right)}{\left(n^2_{hexane} + 2\right)} = \frac{4}{3} \cdot \frac{\mathrm{Pi} \cdot N_a \cdot \rho_{hexane} \cdot \mathrm{alpha}}{Molweight_{hexane}}, \mathrm{alpha} \right) \cdot (1E7)^3 \right) :$$

$$> k_{hexane} := evalf\left(\frac{\lambda_{ex} \cdot \alpha_{hexane}}{(4 \cdot \mathrm{Pi})} \right) :$$

$$> m_{hexane} := n_{hexane} - I \cdot k_{hexane};$$

$$m_{hexane} := 1.391020384 - 0.3459712800\ I \quad \textbf{(1)}$$

Specific complex refractive index for CdSe and CdTe, 300K
m_semiconductor = n - ik
(note: in some papers, k = extinction coefficient; in others, negative extinction coefficient)

CdTe: Bridgeman method single crystal, bulk, cubic(zincblende) from Adachi et al. JApplPhy74 1993
CdSe: VaporPhase growth single crystal, bulk, cubic(zincblende) (c) and wurtzite (w) rom Ninoyima&Adachi JApplPhys78 1995
(For wurtzite, average two axis data)
CdSe with subscript L uses values from Leatherdale paper for cross checking

$$> n_{cCdTe} := 3.02 :$$
$$k_{cCdTe} := 1.47 :$$
$$m_{cCdTe} := n_{cCdTe} - I \cdot k_{cCdTe};$$

$$m_{cCdTe} := 3.02 - 1.47\ I \quad \textbf{(2)}$$

$$> n_{cCdSe} := 2.93 :$$
$$k_{cCdSe} := 0.809 :$$
$$m_{cCdSe} := n_{cCdSe} - I \cdot k_{cCdSe};$$

$$m_{cCdSe} := 2.93 - 0.809\ I \quad \textbf{(3)}$$

$$> n_{wCdSe} := \frac{(2.84 + 2.82)}{2} :$$
$$k_{wCdSe} := \frac{(0.645 + 0.8785)}{2} :$$
$$m_{wCdSe} := n_{wCdSe} - I \cdot k_{wCdSe};$$

$$m_{wCdSe} := 2.830000000 - 0.7617500000\ I \quad \textbf{(4)}$$

$$> n_{LCdSe} := 2.772 :$$
$$k_{LCdSe} := 0.7726 :$$
$$m_{LCdSe} := n_{LCdSe} - I \cdot k_{LCdSe};$$

$$m_{LCdSe} := 2.772 - 0.7726\ I \quad \textbf{(5)}$$

Absorption cross section (nm^2) per QD; a and lambda_ex in nm
Use Equation 2 from Leatherdale paper (Leatherdale et al. JPhysChemB106 2002)
(Assume Leatherdale used tabulated hexane refractive index value; should be close to 5.501E5cm^-1, or5.501E-2cm^-1)

$$> Cabs_{cCdTe} := evalf\left(\frac{8 \cdot \pi^2 \cdot n_{hexane}}{\lambda_{ex}} \cdot \mathrm{Re}\left(I \cdot \frac{\left(m^2_{cCdTe} - n^2_{hexane}\right)}{\left(m^2_{cCdTe} + 2\, n^2_{hexane}\right)} \right) \cdot a^3_{cCdTe} \right);$$

$$Cabs_{cCdTe} := 0.08247102008\ a^3_{cCdTe} \quad \textbf{(6)}$$

$$> \; Cabs_{cCdSe} := evalf\left(\frac{8\cdot\pi^2\cdot n_{hexane}}{\lambda_{ex}} \cdot \Re\left(I\cdot \frac{\left(m^2_{cCdSe} - n^2_{hexane}\right)}{\left(m^2_{cCdSe} + 2\, n^2_{hexane}\right)} \right) \cdot a^3_{cCdSe} \right);$$

$$Cabs_{cCdSe} := 0.05339758676\, a^3_{cCdSe} \tag{7}$$

$$> \; Cabs_{wCdSe} := evalf\left(\frac{8\cdot\pi^2\cdot n_{hexane}}{\lambda_{ex}} \cdot \Re\left(I\cdot \frac{\left(m^2_{wCdSe} - n^2_{hexane}\right)}{\left(m^2_{wCdSe} + 2\, n^2_{hexane}\right)} \right) \cdot a^3_{wCdSe} \right);$$

$$Cabs_{wCdSe} := 0.05370193521\, a^3_{wCdSe} \tag{8}$$

$$> \; Cabs_{LCdSe} := evalf\left(\frac{8\cdot\pi^2\cdot n_{hexanetab}}{\lambda_{ex}} \cdot \Re\left(I\cdot \frac{\left(m^2_{LCdSe} - n^2_{hexanetab}\right)}{\left(m^2_{LCdSe} + 2\, n^2_{hexanetab}\right)} \right) \cdot a^3_{LCdSe} \right);$$

$$Cabs_{LCdSe} := 0.05521338980\, a^3_{LCdSe} \tag{9}$$

Alternatively,
(check for consistency)
Use Equation 4 from Leatherdale paper (Leatherdale et al. JPhysChemB106 2002)

$$> \; Cabs2_{cCdTe} := evalf\left(\frac{\omega_{ex}}{\left(n_{hexane}\cdot c\right)} \cdot \frac{\left(\mathrm{abs}\left(\frac{\left(3\cdot n^2_{hexane}\right)}{\left(m^2_{cCdTe} + 2\cdot n^2_{hexane}\right)} \right) \right)^2 \cdot 2\cdot n_{cCdTe}\cdot k_{cCdTe}\cdot 4\cdot \mathrm{Pi}}{3} \cdot a^3_{cCdTe} \right);$$

$$Cabs2_{cCdTe} := 0.08247102011\, a^3_{cCdTe} \tag{10}$$

$$> \; Cabs2_{cCdSe} := evalf\left(\frac{\omega_{ex}}{\left(n_{hexane}\cdot c\right)} \cdot \frac{\left(\mathrm{abs}\left(\frac{\left(3\cdot n^2_{hexane}\right)}{\left(m^2_{cCdSe} + 2\cdot n^2_{hexane}\right)} \right) \right)^2 \cdot 2\cdot n_{cCdSe}\cdot k_{cCdSe}\cdot 4\cdot \pi}{3} \cdot a^3_{cCdSe} \right);$$

$$Cabs2_{cCdSe} := 0.05339758676\, a^3_{cCdSe} \tag{11}$$

$$> \; Cabs2_{wCdSe} := evalf\left(\frac{\omega_{ex}}{\left(n_{hexane}\cdot c\right)} \cdot \frac{\left(\mathrm{abs}\left(\frac{\left(3\cdot n^2_{hexane}\right)}{\left(m^2_{wCdSe} + 2\cdot n^2_{hexane}\right)} \right) \right)^2 \cdot 2\cdot n_{wCdSe}\cdot k_{wCdSe}\cdot 4\cdot \pi}{3} \cdot a^3_{wCdSe} \right);$$

$$Cabs2_{wCdSe} := 0.05370193518\, a^3_{wCdSe} \tag{12}$$

$$> \; Cabs2_{LCdSe} := evalf\left(\frac{\omega_{ex}}{\left(n_{hexanetab}\cdot c\right)} \cdot \frac{\left(\mathrm{abs}\left(\frac{\left(3\cdot n^2_{hexanetab}\right)}{\left(m^2_{LCdSe} + 2\cdot n^2_{hexanetab}\right)} \right) \right)^2 \cdot 2\cdot n_{LCdSe}\cdot k_{LCdSe}\cdot 4\cdot \pi}{3} \cdot$$

$$a^3_{LCdSe}\Big);$$

$$Cabs2_{LCdSe} := 0.05521338982\ a^3_{LCdSe} \quad \textbf{(13)}$$

OK.

Determine extinction coefficient (1/(M*cm)) using molar; convert absorption cross section to cm^2

> $\varepsilon_{cCdTe} := solve\left(Cabs_{cCdTe} \cdot 1E7 = \frac{2303 \cdot epsilon}{N_a}, epsilon\right);$

$$\varepsilon_{cCdTe} := 2.156493630\ 10^{26}\ a^3_{cCdTe} \quad \textbf{(14)}$$

> $\varepsilon_{cCdSe} := solve\left(Cabs_{cCdSe} \cdot 1E7 = \frac{2303 \cdot \varepsilon}{N_a}, \varepsilon\right);$

$$\varepsilon_{cCdSe} := 1.396266902\ 10^{26}\ a^3_{cCdSe} \quad \textbf{(15)}$$

> $\varepsilon_{wCdSe} := solve\left(Cabs_{wCdSe} \cdot 1E7 = \frac{2303 \cdot \varepsilon}{N_a}, \varepsilon\right);$

$$\varepsilon_{wCdSe} := 1.404225158\ 10^{26}\ a^3_{wCdSe} \quad \textbf{(16)}$$

> $\varepsilon_{LCdSe} := solve\left(Cabs_{LCdSe} \cdot 1E7 = \frac{2303 \cdot \varepsilon}{N_a}, \varepsilon\right);$

$$\varepsilon_{LCdSe} := 1.443747431\ 10^{26}\ a^3_{LCdSe} \quad \textbf{(17)}$$

REFERENCES

1. Image J: Image Processing and Analysis in Java. [cited 2011 June]; Available from: http://rsbweb.nih.gov/ij/index.html.

2. SIDS Initial Assessment Report for SIAM 19: Higher Olefins: United Nations Environmental Programme Chemicals; 2004.

3. Sigma-Aldrich Solvent Center: Acetonitrile [database on the Internet]. Sigma-Aldrich. 2006 [cited March 17th, 2011]. Available from: http://www.sigmaaldrich.com/solvents.

4. Molecular Probes Handbook, A Guide to Fluorescent Probes and Labeling Technologies. 11th ed. Johnson I, Spence MTZ, editors. Carlsbad: Invitrogen Corporation; 2010.

5. Abdul-Karim M-A, Al-Kofahi K, Brown EB, Jain RK, Roysam B. Automated tracing and change analysis of angiogenic vasculature from in vivo multiphoton confocal image time series. Microvascular Research. 66, 113-25 (2003).

6. Alivisatos AP. Perspectives on the Physical Chemistry of Semiconductor Nanocrystals. The Journal of Physical Chemistry. 100, 13226-39 (1996).

7. Alivisatos AP. Semiconductor Clusters, Nanocrystals, and Quantum Dots. Science. 271, 933-7 (1996).

8. Alivisatos P. The use of nanocrystals in biological detection. Nat Biotech. 22, 47-52 (2004).

9. Allen P, Walker B, Bawendi M. Mechanistic Insights into the Formation of InP Quantum Dots. Angewandte Chemie International Edition. 49, 760-2 (2010).

9¾. Rowling JK. Harry Potter and the Deathly Hallows 1ed. New York, NY: Scholastic, Incorporated. 759, 171-3 (2007).

10. Anderson RR, Farinelli W, Laubach H, Manstein D, Yaroslavsky AN, Gubeli J, Jordan K, Neil GR, Shinn M, Chandler W, Williams GP, Benson SV, Douglas DR, Dylla HF. Selective photothermolysis of lipid-rich tissues: A free electron laser study. Lasers in Surgery and Medicine. 38, 913-9 (2006).

11. Andor JA, Berkesi O, Dreveni I, Varga E. Physical and chemical modification of zinc carboxylate-containing lubricants by molecular structure changes. Lubrication Science. 11, 115-34 (1999).

12. Armarego WLF, Chai C. Purification of Laboratory Chemicals. Sixth ed. Burlington, MA: Butterworth-Heinemann, Imprint of Elsevier; 2009.

13. Bailey RE, Nie S. Alloyed Semiconductor Quantum Dots: Tuning the Optical Properties without Changing the Particle Size. Journal of the American Chemical Society. 125, 7100-6 (2003).

14. Bailey RE, Nie S. Core-shell Semiconductor Nanocrystals for Biological Labeling. Rao CNR, Muller A, Cheetham AK, editors. Weinheim: Wiley-VCH Verlag GmbH & Co. KGaA; 2004.

15. Bailey RE, Strausburg JB, Nie S. A New Class of Far-Red and Near-Infrared Biological Labels Based on Alloyed Semiconductor Quantum Dots. Journal of Nanoscience and Nanotechnology. 4, 569-74 (2004).

16. Ballou B, Ernst LA, Andreko S, Eructiez MP, Lagerholm BC, Waggoner AS. Long-Term Retention of Fluorescent Quantum Dots In Vivo. In: Giersig M, Khomutov GB, editors. Nanomaterials for Application in Medicine and Biology: Springer Netherlands; 2008. p. 127-37.

17. Ballou B, Ernst LA, Andreko S, Harper T, Fitzpatrick JAJ, Waggoner AS, Bruchez MP. Sentinel Lymph Node Imaging Using Quantum Dots in Mouse Tumor Models. Bioconjugate Chemistry. 18, 389-96 (2007).

18. Ballou B, Lagerholm BC, Ernst LA, Bruchez MP, Waggoner AS. Noninvasive Imaging of Quantum Dots in Mice. Bioconjugate Chemistry. 15, 79-86 (2004).

19. Barwick VJ. Strategies for solvent selection -- a literature review. TrAC Trends in Analytical Chemistry. 16, 293-309 (1997).

20. Bazterra VE, Caputo MC, Ferraro MB, Fuentealba P. On the theoretical determination of the static dipole polarizability of intermediate size silicon clusters. The Journal of Chemical Physics. 117, 11158-65 (2002).

21. Berkesi O, Katona T, Dreveni I, Andor JA, Mink J. Temperature-dependent Fourier transform infrared and differential scanning calorimetry studies of zinc carboxylates. Vibrational Spectroscopy. 8, 167-74 (1995).

22. Bernard JE, Zunger A. Electronic structure of ZnS, ZnSe, ZnTe, and their pseudobinary alloys. Physical Review B. 36, 3199 (1987).

23. Bestvater F, Spiess E, Stobrawa G, Hacker M, Feurer T, Porwol T, Berchner-Pfannschmidt U, Wotzlaw C, Acker H. Two-photon fluorescence absorption and

emission spectra of dyes relevant for cell imaging. Journal of Microscopy. 208, 108-15 (2002).

24. Bhattacharya SK, Kshirsagar A. Ab initio calculations of structural and electronic properties of CdTe clusters. Physical Review B. 75, 035402 (2007).

25. Bjornsson CS, Lin G, Al-Kofahi Y, Narayanaswamy A, Smith KL, Shain W, Roysam B. Associative image analysis: A method for automated quantification of 3D multi-parameter images of brain tissue. Journal of Neuroscience Methods. 170, 165-78 (2008).

26. Bodnar I, Gurin V, Molochko A, Solovei N, Prokoshin P, Yumashev K. Optical properties of ultradisperse CdSexTe1-x (0<x<1) particles in a silicate glass matrix. Semiconductors. 36, 298-306 (2002).

27. Bruchez M, Moronne M, Gin P, Weiss S, Alivisatos AP. Semiconductor Nanocrystals as Fluorescent Biological Labels. Science. 281, 2013-6 (1998).

28. Brus L. Quantum crystallites and nonlinear optics. Applied Physics A: Materials Science; Processing. 53, 465-74 (1991).

29. Bryce WA, Hinshelwood C. 707. The reaction between paraffin hydrocarbons and sulphur vapour. Journal of the Chemical Society (Resumed). 3379-87 (1949).

30. Cao G, Hong HG, Mallouk TE. Layered metal phosphates and phosphonates: from crystals to monolayers. Accounts of Chemical Research. 25, 420-7 (1992).

31. Cao G, Lynch VM, Yacullo LN. Synthesis, structural characterization, and intercalation chemistry of two layered cadmium organophosphonates. Chemistry of Materials. 5, 1000-6 (1993).

32. Capps KB, Wixmerten B, Bauer A, Hoff CD. Thermochemistry of Sulfur Atom Transfer. Enthalpies of Reaction of Phosphines with Sulfur, Selenium, and Tellurium, and of Desulfurization of Triphenylarsenic Sulfide, Triphenylantimony Sulfide, and Benzyl Trisulfide. Inorganic Chemistry. 37, 2861-4 (1998).

33. Chan WCW, Nie S. Quantum Dot Bioconjugates for Ultrasensitive Nonisotropic Detection. Science. 281, 2016-8 (1998).

34. Chen Y, Thakar R, Snee PT. Imparting Nanoparticle Function with Size-Controlled Amphiphilic Polymers. Journal of the American Chemical Society. 130, 3744-5 (2008).

35. Cheong WF, Prahl SA, Welch AJ. A review of the optical properties of biological tissues. Quantum Electronics, IEEE Journal of. 26, 2166-85 (1990).

36. Choi HS, Ipe BI, Misra P, Lee JH, Bawendi MG, Frangioni JV. Tissue- and Organ-Selective Biodistribution of NIR Fluorescent Quantum Dots. Nano Letters. 9, 2354-9 (2009).

37. Choi HS, Liu W, Misra P, Tanaka E, Zimmer JP, Itty Ipe B, Bawendi MG, Frangioni JV. Renal clearance of quantum dots. Nat Biotech. 25, 1165-70 (2007).

38. Chuang C-H, Lo SS, Scholes GD, Burda C. Charge Separation and Recombination in CdTe/CdSe Core/Shell Nanocrystals as a Function of Shell Coverage: Probing the Onset of the Quasi Type-II Regime. The Journal of Physical Chemistry Letters. 1, 2530-5 (2010).

39. Coetzee JF. Purification of acetonitrile and tests for impurities. Pure & Applied Chemistry. 13, 427-36 (1966).

40. Cullis CF, Hinshelwood CN, Mulcahy MFR, Partington RG. Labile molecules in the kinetics of hydrocarbon reactions. Discussions of the Faraday Society. 2, 111-32 (1947).

41. Dabbousi BO, Rodriguez-Viejo J, Mikulec FV, Heine JR, Mattoussi H, Ober R, Jensen KF, Bawendi MG. CdSe(ZnS) Core-Shell Quantum Dots: Synthesis and Characterization of a Size Series of Highly Luminescent Nanocrystallites. Journal of Physical Chemistry B. 101, 9463-75 (1997).

42. DaCosta RS, Andersson H, Wilson BC. Molecular Fluorescence Excitation–Emission Matrices Relevant to Tissue Spectroscopy¶. Photochemistry and Photobiology. 78, 384-92 (2003).

43. Dagtepe P, Chikan V, Jasinski J, Leppert VJ. Quantized Growth of CdTe Quantum Dots; Observation of Magic-Sized CdTe Quantum Dots. The Journal of Physical Chemistry C. 111, 14977-83 (2007).

44. Davis RE, Nakshbendi HF. Sulfur in Amine Solvents. Journal of the American Chemical Society. 84, 2085-90 (1962).

45. De Smet Y, Deriemaeker L, Finsy R. A Simple Computer Simulation of Ostwald Ripening. Langmuir. 13, 6884-8 (1997).

46. del Monte F, Levy D. Near-Infrared Dyes Encapsulated in Sol-Gel Matrixes. Chemistry of Materials. 7, 292-8 (1995).

47. Devillanova FA. Handbook of Chalcogen Chemistry: New Perspectives in Sulfur, Selenium and Tellurium. Cambridge, United Kingdom: The Royal Society of Chemistry; 2007.

48. Dreveni I, Berkesi O, Andor JA, Mink J. Influence of the spatial structure of the alkyl chain on the composition of the product of the direct neutralization reaction between aliphatic carboxylic acids and zinc hydroxide. Inorganica Chimica Acta. 249, 17-23 (1996).

49. Dukes AD, McBride JR, Rosenthal SJ. Synthesis of Magic-Sized CdSe and CdTe Nanocrystals with Diisooctylphosphinic Acid. Chemistry of Materials. 22, 6402-8 (2010).

50. Ebina A, Asano K, Takahashi T. Surface properties of clean, and with adsorbed oxygen, surfaces of CdTe (110), {111}, and (100) and of CdSe {0001} studied by electron-energy-loss spectroscopy and Auger-electron spectroscopy. Physical Review B. 22, 1980 (1980).

51. Empedocles SA, Bawendi MG. Quantum-Confined Stark Effect in Single CdSe Nanocrystallite Quantum Dots. Science. 278, 2114-7 (1997).

52. Empedocles SA, Norris DJ, Bawendi MG. Photoluminescence Spectroscopy of Single CdSe Nanocrystallite Quantum Dots. Physical Review Letters. 77, 3873 (1996).

53. Evans CM, Evans ME, Krauss TD. Mysteries of TOPSe Revealed: Insights into Quantum Dot Nucleation. Journal of the American Chemical Society. 132, 10973-5 (2010).

54. Fabian J, Nakazumi H, Matsuoka M. Near-Infrared Absorbing Dyes. Chemical Reviews. 92, 1197-226 (1992).

55. Faraji AH, Wipf P. Nanoparticles in cellular drug delivery. Bioorganic & Medicinal Chemistry. 17, 2950-62 (2009).

56. Farmer EH, Shipley FW. 298. The reaction of sulphur and sulphur compounds with olefinic substances. Part I. The reaction of sulphur with mono-olefins and with 1 : 5-diolefins. Journal of the Chemical Society (Resumed). 1519-32 (1947).

57. Farng LO. Ashless Antiwear and Extreme-Pressure Additives. New York, NY: Marcel Dekker, AG; 2003.

58. Frangioni JV. In Vivo Near-Infrared Fluorescence Imaging. Current Opinion in Biotechnology. 7, 626-34 (2003).

59. Fredoueil F, Massiot D, Janvier P, Gingl F, Bujoli-Doeuff M, Evain M, Clearfield A, Bujoli B. Synthesis and X-ray Powder Structure of a New Pillared Layered Cadmium Phosphonate, Giving Evidence that the Intercalation of Alkylamines into Cd(O3PR).H(2)O Is Topotactic. Inorganic Chemistry. 38, 1831-3 (1999).

60. Freund LB, Nix WD. A critical thickness condition for a strained compliant substrate/epitaxial film system. Applied Physics Letters. 69, 173-5 (1996).

61. Fujisaki J, Wu J, Carlson AL, Silberstein L, Putheti P, Larocca R, Gao W, Saito TI, Celso CL, Tsuyuzaki H, Sato T, Cote D, Sykes M, Strom TB, Scadden DT, Lin CP. In vivo imaging of Treg cells providing immune privilege to the haematopoietic stem-cell niche. Nature. 474, 216-9 (2011).

62. Furis M, Sahoo Y, MacRae DJ, Manciu FS, Cartwright AN, Prasad PN. Surfactant-Imposed Interference in the Optical Characterization of GaP Nanocrystals. The Journal of Physical Chemistry B. 107, 11622-5 (2003).

63. Gao J, Chen K, Xie R, Xie J, Yan Y, Cheng Z, Peng X, Chen X. In Vivo Tumor-Targeted Fluorescence Imaging Using Near-Infrared Non-Cadmium Quantum Dots. Bioconjugate Chemistry. 21, 604-9 (2010).

64. Gao X, Yang L, Petros JA, Marshall FF, Simons JW, Nie S. In Vivo Molecular and Cellular Imaging with Quantum Dots. Current Opinion in Biotechnology. 16, 63-72 (2005).

65. Gaponik N, Talapin DV, Rogach AL, Hoppe K, Shevchenko EV, Kornowski A, Eychmuller A, Weller H. Thiol-Capping of CdTe Nanocrystals: An Alternative to Organometallic Synthetic Routes. Journal of Physical Chemistry B. 106, 7177-85 (2002).

66. Gerbier P, Guerin C, Henner B, Unal J-R. An organometallic route to zinc phosphonates and their intercalates. Journal of Materials Chemistry. 9, 2559-65 (1999).

67. Gerweck LE, Seetharaman K. Cellular pH Gradient in Tumor versus Normal Tissue: Potential Exploitation for the Treatment of Cancer. Cancer Research. 56, 1194-8 (1996).

68. Hale GM, Querry MR. Optical Constants of Water in the 200-nm to 200-micron Wavelength Region. Applied Optics. 12, 555-63 (1973).

69. Hannachi L, Bouarissa N. Electronic structure and optical properties of CdSexTe1-x mixed crystals. Superlattices and Microstructures. 44, 794-801 (2008).

70. Hines M, Scholes G. Colloidal PbS Nanocrystals with Size-Tunable Near-Infrared Emission: Observation of Post-Synthesis Self-Narrowing of the Particle Size Distribution. Advanced Materials. 15, 1844-9 (2003).

71. Hines MA, Guyot-Sionnest P. Synthesis and Characterization of Strongly Luminescing ZnS-Capped CdSe Nanocrystals. The Journal of Physical Chemistry. 100, 468-71 (1996).

72. Howarth M, Liu W, Puthenveetil S, Zheng Y, Marshall LF, Schmidt MM, Wittrup KD, Bawendi MG, Ting AY. Monovalent, reduced-size quantum dots for imaging receptors on living cells. Nat Meth. 5, 397-9 (2008).

73. Hu R, Yong K-T, Roy I, Ding H, Law W-C, Cai H, Zhang X, Vathy LA, Bergey EJ, Prasad PN. Functionalized near-infrared quantum dots for in vivo tumor vasculature imaging. Nanotechnology. 21, 145105 (2010).

74. Ivanov SA, Piryatinski A, Nanda J, Tretiak S, Zavadil KR, Wallace WO, Werder D, Klimov VI. Type-II Core/Shell CdS/ZnSe Nanocrystals: Synthesis, Electronic Structures, and Spectroscopic Properties. Journal of the American Chemical Society. 129, 11708-19 (2007).

75. Jana NR, Chen Y, Peng X. Size- and Shape-Controlled Magnetic (Cr, Mn, Fe, Co, Ni) Oxide Nanocrystals via a Simple and General Approach. Chemistry of Materials. 16, 3931-5 (2004).

76. Jasieniak J, Bullen C, van Embden J, Mulvaney P. Phosphine-Free Synthesis of CdSe Nanocrystals. The Journal of Physical Chemistry B. 109, 20665-8 (2005).

77. Jiang W, Singhal A, Zheng J, Wang C, Chan WCW. Optimizing the Synthesis of Red- to Near-IR-Emitting CdS-Capped CdTexSe1-x Alloyed Quantum Dots for Biomedical Imaging. Chemistry of Materials. 18, 4845-54 (2006).

78. John R, Catherine DH, Pushpalatha S. Theoretical Investigations on II-VI Binary Semiconductors. Chalcogenide Letters. 7, 277-82 (2010).

79. Kabalnov AS, Shchukin ED. Ostwald ripening theory: applications to fluorocarbon emulsion stability. Advances in Colloid and Interface Science. 38, 69-97 (1992).

80. Kadish KM, Mu X, Anderson JE. Recommended methods for the purification of solvents and tests for impurities: Benzene and toluene. Pure and Applied Chemistry. 61, 1823-8 (1989).

81. Kammann KPJ, Phillips A-I, inventors; Ferro Corporation, Cleveland, Ohio, assignee. Catalyzing the sulfurization of olefins by tertiary phosphines, and an oil based material containing an additive amount of a sulfurized olefin so produced. United States of America patent 4331564. 1982.

82. Kaneko F, Yamazaki K, Kitagawa K, Kikyo T, Kobayashi M, Kitagawa Y, Matsuura Y, Sato K, Suzuki M. Structure and Crystallization Behavior of the Beta Phase of Oleic Acid. The Journal of Physical Chemistry B. 101, 1803-9 (1997).

83. Kim S, Fisher B, Eisler H, Bawendi MG. Type-II Quantum Dots: CdTe/CdSe (Core/Shell) and CdSe/ZnTe (Core/Shell) Heterostructures. Journal of American Chemical Society. 125, 11466-7 (2003).

84. Kim S, Lim YT, Soltesz EG, De Grand AM, Lee J, Nakayama A, Parker JA, Mihaljevic T, Laurence RG, Dor DM, Cohn LH, Bawendi MG, Frangioni JV. Near-Infrared Fluorescent Type-II Quantum Dots for Sentinel Lymph Node Mapping. Nature Biotechnology. 22, 93-7 (2004).

85. Kim S-W, Zimmer JP, Ohnishi S, Tracy JB, Frangioni JV, Bawendi MG. Engineering InAsxP1-x/InP/ZnSe III-V Alloyed Core-Shell Quantum Dots for the Near-Infrared. Journal of American Chemical Society. 127, 10526-32 (2005).

86. Kiricuta I-C, Simplaceanu V. Tissue Water Content and Nuclear Magnetic Resonance in Normal and Tumor Tissues. Cancer Research. 35, 1164-7 (1975).

87. Klimov VI, Mikhailovsky AA, Xu S, Malko A, Hollingsworth JA, Leatherdale CA, Eisler H-J, Bawendi MG. Optical Gain and Stimulated Emission in Nanocrystal Quantum Dots. Science. 290, 314-7 (2000).

88. Kloper V, Osovsky R, Cheskis D, Sashchiuk A, Lifshitz E. Suppressed blinking in CdTe/CdSe core-shell quantum dots. physica status solidi (c). 6, 2719-21 (2009).

89. Konkoly-Thege I, Ruff I, Adeosun SO, Sime SJ. Properties of molten carboxylates part 6. A quantiative differential thermal analysis study of phase transitions in some zinc and cadmium carboxylates. Thermochimica Acta. 24, 89-96 (1978).

90. Kopping JT, Patten TE. Identification of Acidic Phosphorus-Containing Ligands Involved in the Surface Chemistry of CdSe Nanoparticles Prepared in Tri-N-octylphosphine Oxide Solvents. Journal of the American Chemical Society. 130, 5689-98 (2008).

91. Kudera S, Zanella M, Giannini C, Rizzo A, Li Y, Gigli G, Cingolani R, Ciccarella G, Spahl W, Parak WJ, Manna L. Sequential Growth of Magic-Size CdSe Nanocrystals. Advanced Materials. 19, 548-52 (2007).

92. Kumar S, Nann T. Shape Control of II–VI Semiconductor Nanomaterials. Small. 2, 316-29 (2006).

93. Kuno M, Lee JK, Dabbousi BO, Mikulec FV, Bawendi MG. The band edge luminescence of surface modified CdSe nanocrystallites: Probing the luminescing state. The Journal of Chemical Physics. 106, 9869-82 (1997).

94. Lach-hab M, Papaconstantopoulos DA, Mehl MJ. Electronic structure calculations of lead chalcogenides PbS, PbSe, PbTe. Journal of Physics and Chemistry of Solids. 63, 833-41 (2002).

95. LaMer VK. Nucleation in Phase Transitions. Industrial & Engineering Chemistry. 44, 1270-7 (1952).

96. LaMer VK, Dinegar RH. Theory, Production and Mechanism of Formation of Monodispersed Hydrosols. Journal of the American Chemical Society. 72, 4847-54 (1950).

97. Larson DR, Zipfel WR, Williams RM, Clark SW, Bruchez MP, Wise FW, Webb WW. Water-Soluble Quantum Dots for Multiphoton Fluorescence Imaging In Vivo. Science. 300, 1434-6 (2003).

98. Leatherdale CA, Woo WK, Mikulec FV, Bawendi MG. On the Absorption Cross Section of CdSe Nanocrystal Quantum Dots. The Journal of Physical Chemistry B. 106, 7619-22 (2002).

99. Ley K, Laudanna C, Cybulsky MI, Nourshargh S. Getting to the site of inflammation: the leukocyte adhesion cascade updated. Nat Rev Immunol. 7, 678-89 (2007).

100. Li JJ, Wang A, Guo W, Keay JC, Mishima TD, Johnson MB, Peng X. Large-Scale Synthesis of Nearly Monodisperse CdSe/CdS Core/Shell Nanocrystals Using Air-Stable Reagents via Successive Ion Layer Adsorption and Reaction. Journal of American Chemical Society. 125, 12567-75 (2003).

101. Li LS, Pradhan N, Wang Y, Peng X. High Quality ZnSe and ZnS Nanocrystals Formed by Activating Zinc Carboxylate Precursors. Nano Letters. 4, 2261-4 (2004).

102. Li Y-H, Gong XG, Wei S-H. Ab initio all-electron calculation of absolute volume deformation potentials of IV-IV, III-V, and II-VI semiconductors: The chemical trends. Physical Review B. 73, 245206 (2006).

103. Li Z-W, Dalton WS. Tumor microenvironment and drug resistance in hematologic malignancies. Blood Reviews. 20, 333-42 (2006).

104. Lim YT, Kim S, Nakayama A, Stott NE, Bawendi MG, Frangioni JV. Selection of Quantum Dot Wavelengths for Biomedical Assays and Imaging. Molecular Imaging. 2, 50-64 (2003).

105. Liu H, Owen JS, Alivisatos AP. Mechanistic Study of Precursor Evolution in Colloidal Group II-VI Semiconductor Nanocrystal Synthesis. Journal of the American Chemical Society. 129, 305-12 (2007).

106. Liu W, Greytak AB, Lee J, Wong CR, Park J, Marshall LF, Jiang W, Curtin PN, Ting AY, Nocera DG, Fukumura D, Jain RK, Bawendi MG. Compact Biocompatible Quantum Dots via RAFT-Mediated Synthesis of Imidazole-Based Random Copolymer Ligand. Journal of the American Chemical Society. 132, 472-83 (2009).

107. Lo Celso C, Fleming HE, Wu JW, Zhao CX, Miake-Lye S, Fujisaki J, Cote D, Rowe DW, Lin CP, Scadden DT. Live-animal tracking of individual haematopoietic stem/progenitor cells in their niche. Nature. 457, 92-6 (2009).

108. Lo Celso C, Wu JW, Lin CP. In vivo imaging of hematopoietic stem cells and their microenvironment. Journal of Biophotonics. 2, 619-31 (2009).

109. Lo YH. New approach to grow pseudomorphic structures over the critical thickness. Applied Physics Letters. 59, 2311-3 (1991).

110. Ma J, Cheng C, Sun G, Wooley KL. A polarity-activation strategy for the high incorporation of 1-alkenes into functional copolymers via RAFT copolymerization. Journal of Polymer Science Part A: Polymer Chemistry. 46, 3488-98 (2008).

111. Ma Q, Su X. Near-infrared quantum dots: synthesis, functionalization and analytical applications. Analyst. 135, 1867-77 (2010).

112. Mahler B, Spinicelli P, Buil S, Quelin X, Hermier J-P, Dubertret B. Towards non-blinking colloidal quantum dots. Nat Mater. 7, 659-64 (2008).

113. Manna L, Scher EC, Alivisatos AP. Synthesis of Soluble and Processable Rod-, Arrow-, Teardrop-, and Tetrapod-Shaped CdSe Nanocrystals. Journal of the American Chemical Society. 122, 12700-6 (2000).

114. Manna L, Wang, Cingolani R, Alivisatos AP. First-Principles Modeling of Unpassivated and Surfactant-Passivated Bulk Facets of Wurtzite CdSe:, A Model System for Studying the Anisotropic Growth of CdSe Nanocrystals. The Journal of Physical Chemistry B. 109, 6183-92 (2005).

115. Masters BR, So PTC. Handbook of biomedical nonlinear optical microscopy. New York, USA: Oxford University Press; 2008.

116. Mazo I, von Andrian U. Adhesion and homing of blood-borne cells in bone marrow microvessels. Journal of Leukocyte Biology. 66, 25-32 (1999).

117. Mendez-Ferrer S, Lucas D, Battista M, Frenette PS. Haematopoietic stem cell release is regulated by circadian oscillations. Nature. 452, 442-7 (2008).

118. Mesubi MA. An infrared study of zinc, cadmium, and lead salts of some fatty acids. Journal of Molecular Structure. 81, 61-71 (1982).

119. Meulenberg RW, Jennings T, Strouse GF. Compressive and tensile stress in colloidal CdSe semiconductor quantum dots. Physical Review B. 70, 235311 (2004).

120. Michalet X, Pinaud FF, Bentolila LA, Tsay JM, Doose S, Li JJ, Sundaresan G, Wu AM, Gambhir SS, Weiss S. Quantum Dots for Live Cells, In Vivo Imaging, and Diagnostics. Science. 307, 538-44 (2005).

121. Moitra J, Sammani S, Garcia JGN. Re-evaluation of Evans Blue dye as a marker of albumin clearance in murine models of acute lung injury. Translational research : the journal of laboratory and clinical medicine. 150, 253-65 (2007).

122. Moore KA, Lemischka IR. Stem Cells and Their Niches. Science. 311, 1880-5 (2006).

123. Morris-Cohen AJ, Frederick MT, Lilly GD, McArthur EA, Weiss EA. Organic Surfactant-Controlled Composition of the Surfaces of CdSe Quantum Dots. The Journal of Physical Chemistry Letters. 1, 1078-81 (2010).

124. Mourad D, Czycholl G. Multiband tight-binding theory of disordered AxB1-xC semiconductor quantum dots. Eur Phys J B. (2010).

125. Mundy GR. Metastasis: Metastasis to bone: causes, consequences and therapeutic opportunities. Nat Rev Cancer. 2, 584-93 (2002).

126. Murray CB. Synthesis and Characterization of II-VI Quantum Dots and Their Assembly into 3D Quantum Dot Superlattices. Cambridge, MA: Massachusetts Institute of Technology; 1995.

127. Murray CB, Norris DJ, Bawendi MG. Synthesis and Characterization of Nearly Monodisperse CdE (E=S,Se,Te) Semiconductor Nanocrystallites. Journal of American Chemical Society. 115, 8706-15 (1993).

128. Murray CB, Sun S, Gaschler W, Doyle H, Betley TA, Kagan CR. Colloidal Synthesis of Nanocrystals and Nanocrystal Superlattices. IBM Journal of Research and Development. 45, 47-56 (2001).

129. Neuhauser RG, Shimizu KT, Woo WK, Empedocles SA, Bawendi MG. Correlation between Fluorescence Intermittency and Spectral Diffusion in Single Semiconductor Quantum Dots. Physical Review Letters. 85, 3301 (2000).

130. Nguyen DX, Bos PD, Massague J. Metastasis: from dissemination to organ-specific colonization. Nat Rev Cancer. 9, 274-84 (2009).

131. Nirmal M, Brus L. Luminescence Photophysics in Semiconductor Nanocrystals. Accounts of Chemical Research. 32, 407-14 (1999).

132. Nirmal M, Dabbousi BO, Bawendi MG, Macklin JJ, Trautman JK, Harris TD, Brus LE. Fluorescence intermittency in single cadmium selenide nanocrystals. Nature. 383, 802-4 (1996).

133. Norris DJ, Bawendi MG. Measurement and assignment of the size-dependent optical spectrum in CdSe quantum dots. Physics Review B. 53, 16338-46 (1996).

134. Nose K, Fujita H, Omata T, Otsuka-Yao-Matsuo S, Nakamura H, Maeda H. Chemical role of amines in the colloidal synthesis of CdSe quantum dots and their luminescence properties. Journal of Luminescence. 126, 21-6 (2007).

135. Owen JS, Chan EM, Liu H, Alivisatos AP. Precursor Conversion Kinetics and the Nucleation of Cadmium Selenide Nanocrystals. Journal of the American Chemical Society. 132, 18206-13 (2010).

136. Pellegrino T, Manna L, Kudera S, Liedl T, Koktysh D, Rogach AL, Keller S, Radler J, Natile G, Parak WJ. Hydrophobic Nanocrystals Coated with an Amphiphilic Polymer Shell: A general Route to Water Soluble Nanocrystals. Nano Letters. 4, 703-7 (2004).

137. Peng X, Manna L, Yang W, Wickham J, Scher E, Kadavanich A, Alivisatos AP. Shape control of CdSe nanocrystals. Nature. 404, 59-61 (2000).

138. Peng X, Wickham J, Alivisatos AP. Kinetics of II-VI and III-V Colloidal Semiconductor Nanocrystal Growth: Focusing of Size Distributions. Journal of the American Chemical Society. 120, 5343-4 (1998).

139. Peng ZA, Peng X. Formation of High-Quality CdTe, CdSe, and CdS Nanocrystals Using CdO as Precursor. Journal of American Chemical Society. 123, 183-4 (2001).

140. Peng ZA, Peng X. Nearly Monodisperse and Shape-Controlled CdSe Nanocrystals via Alternative Routes: Nucleation and Growth. Journal of the American Chemical Society. 124, 3343-53 (2002).

141. Penicaud V, Massiot D, Gelbard G, Odobel F, Bujoli B. Preparation of structural analogues of divalent metal monophosphonates, using bis(phosphonic) acids: a new strategy to reduce overcrowding of organic groups in the interlayer space. Journal of Molecular Structure. 470, 31-8 (1998).

142. Perov EI, Moshchenskaya NV. Solubility and State of Elemental Selenium in Hydrocarbons. Russian Journal of Applied Chemistry. 74, 1641-4 (2001).

143. Pietryga JM, Schaller RD, Werder D, Stewart MH, Klimov VI, Hollingsworth JA. Pushing the Band Gap Envelope: Mid-Infrared Emitting Colloidal PbSe Quantum Dots. Journal of the American Chemical Society. 126, 11752-3 (2004).

144. Pons T, Lequeux N, Mahler B, Sasnouski S, Fragola A, Dubertret B. Synthesis of Near-Infrared-Emitting, Water-Soluble CdTeSe/CdZnS Core/Shell Quantum Dots. Chemistry of Materials. 21, 1418-24 (2009).

145. Pons T, Uyeda HT, Medintz IL, Mattoussi H. Hydrodynamic Dimensions, Electrophoretic Mobility, and Stability of Hydrophilic Quantum Dots. The Journal of Physical Chemistry B. 110, 20308-16 (2006).

146. Poon HC, Feng ZC, Feng YP, Li MF. Relativistic band structure of ternary II-VI semiconductor alloys containing Cd, Zn, Se and Te. Journal of Physics: Condensed Matter. 7, 2783-99 (1995).

147. Popović Z, Liu W, Chauhan VP, Lee J, Wong C, Greytak AB, Insin N, Nocera DG, Fukumura D, Jain RK, Bawendi MG. A Nanoparticle Size Series for In Vivo Fluorescence Imaging. Angewandte Chemie International Edition. 49, 8649-52 (2010).

148. Prahl S. Optical Absorption of Water Compendium. 2010 [updated 2010; cited 2011 June 24th]; Available from: http://omlc.ogi.edu/spectra/water/abs/index.html.

149. Prahl S. Optical Absorption of Hemoglobin. 2010 [updated 2010; cited]; Available from: http://omlc.ogi.edu/spectra/hemoglobin/index.html.

150. Pries A, Kuebler W. Normal Endothelium. In: Moncada S, Higgs A, editors. The Vascular Endothelium I: Springer Berlin Heidelberg; 2006. p. 1-40.

151. Puzder A, Williamson AJ, Gygi F, Galli G. Self-Healing of CdSe Nanocrystals: First-Principles Calculations. Physical Review Letters. 92, 217401 (2004).

152. Qian X, Brennan MP, Dione DP, Dobrucki WL, Jackowski MP, Breuer CK, Sinusas AJ, Papademetris X. A non-parametric vessel detection method for complex vascular structures. Medical Image Analysis. 13, 49-61 (2009).

153. Qu L, Peng ZA, Peng X. Alternative Routes toward High Quality CdSe Nanocrystals. Nano Letters. 1, 333-7 (2001).

154. Quin LD. A Guide to Organophosphorus Chemistry. New York, New York: John Wiley & Sons; 2000.

155. Reiss H. The Growth of Uniform Colloidal Dispersions. Journal of Chemical Physics. 19, 482-7 (1951).

156. Rempel JY, Trout BL, Bawendi MG, Jensen KF. Properties of the CdSe(0001), (0001), and (1120) Single Crystal Surfaces: Relaxation, Reconstruction, and Adatom and Admolecule Adsorption. The Journal of Physical Chemistry B. 109, 19320-8 (2005).

157. Rempel JY, Trout BL, Bawendi MG, Jensen KF. Density Functional Theory Study of Ligand Binding on CdSe (0001), (0001), and (1120) Single Crystal Relaxed and Reconstructed Surfaces: Implications for Nanocrystalline Growth. The Journal of Physical Chemistry B. 110, 18007-16 (2006).

158. Resch-Genger U, Grabolle M, Cavaliere-Jaricot S, Nitschke R, Nann T. Quantum dots versus organic dyes as fluorescent labels. Nat Meth. 5, 763-75 (2008).

159. Richards-Kortum R, Sevick-Muraca E. QUANTITATIVE OPTICAL SPECTROSCOPY FOR TISSUE DIAGNOSIS. Annual Review of Physical Chemistry. 47, 555-606 (1996).

160. Riviere JE. Pharmacokinetics of nanomaterials: an overview of carbon nanotubes, fullerenes and quantum dots. Wiley Interdisciplinary Reviews: Nanomedicine and Nanobiotechnology. 1, 26-34 (2009).

161. Rogach AL, Eychmüller A, Hickey SG, Kershaw SV. Infrared-Emitting Colloidal Nanocrystals: Synthesis, Assembly, Spectroscopy, and Applications. Small. 3, 536-57 (2007).

162. Roggan A, Friebel M, Dorschel K, Hahn A, Muller G. Optical Properties of Circulating Human Blood in the Wavelength Range 400--2500 nm. Journal of Biomedical Optics. 4, 36-46 (1999).

163. Roodman GD. Mechanisms of Bone Metastasis. New England Journal of Medicine. 350, 1655-64 (2004).

164. Runnels JM, Carlson AL, Pitsillides C, Thompson B, Wu J, Spencer JA, Kohler JMJ, Azab A, Moreau A-S, Rodig SJ, Kung AL, Anderson KC, Ghobrial IM, Lin CP. Optical techniques for tracking multiple myeloma engraftment, growth, and response to therapy. Journal of Biomedical Optics. 16, 011006-13 (2011).

165. Sadekov ID, Maksimenko AA, Nivorozhkin VL. Organic derivatives of monocoordinated tellurium. Russian Chemical Reviews. 67, 193 (1998).

166. Scadden DT. The stem-cell niche as an entity of action. Nature. 441, 1075-9 (2006).

167. Schirmer RE. Modern Methods of Pharmaceutical Analysis: Volume 2. Boca Raton, Florida: CRC Press; 1991.

168. Schmitt JM, Kumar G. Optical Scattering Properties of Soft Tissue: A Discrete Particle Model. Appl Opt. 37, 2788-97 (1998).

169. Schofield R. The relationship between the spleen colony-forming cell and the haemopoietic stem cell. Blood Cells. 4, 7-25 (1978).

170. Shoffner JP, inventor Separation of Dissimilar Amines patent 4174351. 1979.

171. Sipkins DA, Wei X, Wu JW, Runnels JM, Cote D, Means TK, Luster AD, Scadden DT, Lin CP. In vivo imaging of specialized bone marrow endothelial microdomains for tumour engraftment. Nature. 435, 969-73 (2005).

172. Smith AM, Mancini MC, Nie S. Bioimaging: Second window for in vivo imaging. Nat Nano. 4, 710-1 (2009).

173. Smith AM, Mohs AM, Nie S. Tuning the optical and electronic properties of colloidal nanocrystals by lattice strain. Nat Nano. 4, 56-63 (2009).

174. Smith JD, Fisher GW, Waggoner AS, Campbell PG. The use of quantum dots for analysis of chick CAM vasculature. Microvascular Research. 73, 75-83 (2007).

175. Snyder LR. Classification of the solvent properties of common liquids. Journal of Chromatography A. 92, 223-30 (1974).

176. So PTC, Dong CY, Masters BR, Berland KM. TWO-PHOTON EXCITATION FLUORESCENCE MICROSCOPY. Annual Review of Biomedical Engineering. 2, 399-429 (2000).

177. Sperling RA, Liedl T, Duhr S, Kudera S, Zanella M, Lin CAJ, Chang WH, Braun D, Parak WJ. Size Determination of (Bio)conjugated Water-Soluble Colloidal Nanoparticles: A Comparison of Different Techniques. The Journal of Physical Chemistry C. 111, 11552-9 (2007).

178. Spiess E, Bestvater F, Heckel-Pompey A, Toth K, Hacker M, Stobrawa G, Feurer T, Wotzlaw C, Berchner-Pfannschmidt U, Porwol T, Acker H. Two-photon excitation and emission spectra of the green fluorescent protein variants ECFP, EGFP and EYFP. Journal of Microscopy. 217, 200-4 (2005).

179. Steckel JS, Yen BKH, Oertel DC, Bawendi MG. On the Mechanism of Lead Chalcogenide Nanocrystal Formation. Journal of the American Chemical Society. 128, 13032-3 (2006).

180. Sun X, Cheng G, Hao M, Zheng J, Zhou X, Zhang J, Taichman R, Pienta K, Wang J. CXCL12 / CXCR4 / CXCR7 chemokine axis and cancer progression. Cancer and Metastasis Reviews. 29, 709-22 (2010).

181. Teicher BA, Fricker SP. CXCL12 (SDF-1)/CXCR4 Pathway in Cancer. Clinical Cancer Research. 16, 2927-31 (2010).

182. Tsai CL, Chen JC, Wang WJ. Near-infrared Absorption Property of Biological Soft Tissue Constituents. Journal of Medical and Biological Engineering. 21, 7-14 (2001).

183. Urzua MD, Mendiz·bal FJ, Cabrera WJ, RÌos HnE. Interfacial properties of poly(maleic acid-alt-1-alkene) disodium salts at water/hydrocarbon interfaces. Journal of Colloid and Interface Science. 281, 93-100 (2005).

184. van Embden J, Jasieniak J, Gomez DE, Mulvaney P, Giersig M. Review of the Synthetic Chemistry Involved in the Production of Core/Shell Semiconductor Nanocrystals. ChemInform. 38, no-no (2007).

185. van Veen R, Sterenborg H, Pifferi A, Torricelli A, Cubeddu R, editors. Determination of VIS- NIR absorption coefficients of mammalian fat, with time- and spatially resolved diffuse reflectance and transmission spectroscopy. OSA Annual BIOMED Topical Meeting; 2004.

186. Vincent B, Edwards J, Emmett S, Jones A. Depletion flocculation in dispersions of sterically-stabilised particles ("soft spheres"). Colloids and Surfaces. 18, 261-81 (1986).

187. Vioux A, Le Bideau J, Mutin PH, Leclercq D. Hybrid Organic-Inorganic Materials Based on Organophosphorus Derivatives. In: Majoral J-P, editor. New Aspects in Phosphorus Chemistry IV: Springer Berlin / Heidelberg; 2004. p. 145-74.

188. Wang BG, KÖNig K, Halbhuber KJ. Two-photon microscopy of deep intravital tissues and its merits in clinical research. Journal of Microscopy. 238, 1-20 (2010).

189. Wang F, Tang R, Buhro WE. The Trouble with TOPO; Identification of Adventitious Impurities Beneficial to the Growth of Cadmium Selenide Quantum Dots, Rods, and Wires. Nano Letters. 8, 3521-4 (2008).

190. Wang F, Tang R, Kao JLF, Dingman SD, Buhro WE. Spectroscopic Identification of Tri-n-octylphosphine Oxide (TOPO) Impurities and Elucidation of Their Roles in Cadmium Selenide Quantum-Wire Growth. Journal of the American Chemical Society. 131, 4983-94 (2009).

191. Wang R, Calvignanello O, Ratcliffe CI, Wu X, Leek DM, Zaman MB, Kingston D, Ripmeester JA, Yu K. Homogeneously-Alloyed CdTeSe Single-Sized Nanocrystals with Bandgap Photoluminescence. The Journal of Physical Chemistry C. 113, 3402-8 (2009).

192. Wolcott A, Fitzmorris RC, Muzaffery O, Zhang JZ. CdSe Quantum Rod Formation Aided By In Situ TOPO Oxidation. Chemistry of Materials. 22, 2814-21 (2010).

193. Xu H, Rice BW. In-vivo fluorescence imaging with a multivariate curve resolution spectral unmixing technique. Journal of Biomedical Optics. 14, 064011-9 (2009).

194. Yordanov G, Yoshimura H, Dushkin C. Phosphine-free synthesis of metal chalcogenide quantum dots by means of in situ-generated hydrogen chalcogenides. Colloid & Polymer Science. 286, 813-7 (2008).

195. Yu WW, Qu L, Guo W, Peng X. Experimental Determination of the Extinction Coefficient of CdTe, CdSe, and CdS Nanocrystals. Chemistry of Materials. 15, 2854-60 (2003).

196. Zanella M, Abbasi AZ, Schaper AK, Parak WJ. Discontinuous Growth of II-VI Semiconductor Nanocrystals from Different Materials. The Journal of Physical Chemistry C. 114, 6205-15 (2010).

197. Zhang W, Chen G, Wang J, Ye B-C, Zhong X. Design and Synthesis of Highly Luminescent Near-Infrared-Emitting Water-Soluble CdTe/CdSe/ZnS Core/Shell/Shell Quantum Dots. Inorganic Chemistry. 48, 9723-31 (2009).

198. Zhang Y, Li Y, Yan X-P. Aqueous Layer-by-Layer Epitaxy of Type-II CdTe/CdSe Quantum Dots with Near-Infrared Fluorescence for Bioimaging Applications. Small. 5, 185-9 (2009).

199. Zhong H, Nagy M, Jones M, Scholes GD. Electronic States and Exciton Fine Structure in Colloidal CdTe Nanocrystals. The Journal of Physical Chemistry C. 113, 10465-70 (2009).

200. Zhu YF, Lang XY, Jiang Q. The Effect of Alloying on the Bandgap Energy of Nanoscaled Semiconductor Alloys. Advanced Functional Materials. 18, 1422-9 (2008).

201. Zimmer JP, Kim S-W, Ohnishi S, Tanaka E, Frangioni JV, Bawendi MG. Size Series of Small Indium Arsenide-Zinc Selenide Core-Shell Nanocrystals and Their Application to In Vivo Imaging. Journal of American Chemical Society. 128, 2526-7 (2006).

202. Zipfel W, Williams R, Webb W. Nonlinear magic: multiphoton microscopy in the biosciences. Nature Biotechnology. 21, 1369 - 77 (2003).

203. Ascenzi A, Fabry C. Technique for Dissection and Measurement of Refractive Index of Osteones. Journal of Biophysical & Biochemical Cytology. 6, 139-42 (1959).

204. Drobizhev M, Tillo S, Makarov NS, Hughes TE, Rebane A. Absolute Two-Photon Absorption Spectra and Two-Photon Brightness of Orange and Red Fluorescent Proteins. The Journal of Physical Chemistry B. 113, 855-9 (2009).

205. Dunn A, Richards-Kortum R. Three-dimensional computation of light scattering from cells. Selected Topics in Quantum Electronics, IEEE Journal of. 2, 898-905 (1996).

206. Eldred GE, Miller GV, Stark WS, Feeney-Burns L. Lipofuscin: Resolution of Discrepant Fluorescence Data. Science. 216, 757-9 (1982).

207. Finsy R. On the Critical Radius in Ostwald Ripening. Langmuir. 20, 2975-6 (2004).

208. Stark WS, Miller GV, Itoku KA. [42] Calibration of microspectrophotometers as it applies to the detection of lipofuscin and the blue- and yellow-emitting fluorophores in situ. In: Lester P, editor. Methods in Enzymology: Academic Press; 1984. p. 341-7.

209. Troy T, Jekic-McMullen D, Sambucetti L, Rice B. Quantitative Comparison of the Sensitivity of Detection of Fluorescent and Bioluminescent Reporters in Animal Models. Molecular Imaging. 3, 9-23 (2004).

210. Wu X, Liu H, Liu J, Haley KN, Treadway JA, Larson JP, Ge N, Peale F, Bruchez M. Immunofluorescent Labeling of Cancer Marker Her2 and other Cellular Targets with Semiconductor Quantum Dots. Nature Biotechnology. 21, 41-6 (2003).

211. Tolbert SH, Alivisatos AP. Size Dependence of a First Order Solid-Solid Phase Transition: The Wurtzite to Rock Salt Transformation in CdSe Nanocrystals. Science. 265, 373-6 (1994).

212. Pogue BW, Jiang S, Dehghani H, Kogel C, Soho S, Srinivasan S, Song X, Tosteson TD, Poplack SP, Paulsen KD. Characterization of hemoglobin, water, and NIR scattering in breast tissue: analysis of intersubject variability and menstrual cycle changes: SPIE; 2004.

213. Turzhitsky V, Radosevich AJ, Rogers JD, Mutyal NN, Backman V. Measurement of optical scattering properties with low-coherence enhanced backscattering spectroscopy: SPIE; 2011.

214. Gekle M. Renal albumin handling: A look at the dark side of the filter. Kidney Int. 71, 479-81 (0000).